Interference and interaction of charge carriers in graphene

Submitted by Aleksey Kozikov to the University of Exeter

as a thesis for the degree of

Doctor of Philosophy in Physics

in April, 2011

This thesis is available for Library use on the understanding that it is copyright material and that no quotation from the thesis may be published without proper acknowledgement.

I certify that all material in this thesis which is not my own work has been identified and that no material has previously been submitted and approved for the award of a degree by this or any other University.

Abstract

Electron transport at low temperatures in two-dimensional electron systems is governed by two quantum corrections to the conductivity: weak localisation and electron-electron interaction in the presence of disorder. We present the first experimental observation of these quantum corrections in graphene, a single layer of carbon atoms, over a temperature range 0.02 - 200 K. Due to the peculiar properties of graphene, weak localisation is sensitive not only to inelastic, phase-breaking scattering events, but also to elastic scattering mechanisms. The latter includes scattering within and between the two valleys (intra- and inter-valley scattering, respectively). These specifics make it possible, for example, to observe a transition from weak localisation to antilocalisation. Our work reveals a number of surprising features. First of all the transition occurs not only as the carrier density is varied, but also as the temperature is tuned. The latter has never been observed in any other system studied before. Second, due to weak electron-phonon interaction in graphene, quantum interference of electrons survives at very high temperatures, up to 200 K. For comparison, in other two-dimensional (2D) systems the weak localisation effect is only seen below 50 K.

The electron-electron interaction correction is also affected by elastic scattering. In a two-valley system, there are two temperature regimes of the interaction correction that depend on the strength of inter-valley scattering. In both regimes the correction has its own expression. We show that because of the intra-valley scattering, a third regime is possible in graphene, where the expression for the correction takes a new form. The study of weak localisation demonstrates that the third regime is realised in our experiments. We use the new expression to determine the Fermi-liquid parameter, which turns out to be smaller than in other 2D systems due to the chirality of charge carriers.

At very low temperatures (below 100 mK) we observe a saturation of the electron dephasing length. We study different mechanisms that could be responsible for the saturation and discuss in detail two of them – spin-orbit interaction and electron scattering off vacancies. We determine the spin coherence length from studies of weak localisation and the temperature dependence of the conductivity and found good agreement between the two types of experiments. We also show the way to

tune the spin coherence length by an order of magnitude by controlling the level of disorder. However, experiment shows contradictions with theory both in values of the spin coherence length and the type of spin relaxation. We speculate about another spin-related mechanism, spin flip by vacancies.

We also present electron transport in graphene irradiated by gallium ions. Depending on the dosage of irradiation the behavior of electrons changes. Namely, electron localisation can be tuned from weak to strong. At low dosages we observe the weak localisation regime, where the mentioned quantum corrections to the conductivity dominate at low temperatures. We found the electron scattering between the valleys to be enhanced, attributing it to atomically sharp defects (kicked out carbon atoms) produced by ion irradiation. We also speculate that gallium ions can be embedded in the substrate or trapped between silica and graphene. We draw this conclusion after investigation of the spin-orbit interaction in irradiated samples. At high dosages electrons become strongly localised and their transport occurs via variable-range hopping.

Acknowledgements

I would like to thank Professor Alex Savchenko who had been my supervisor during the first two years of my PhD. He made it possible for me to study experimental physics in England, which gave me a lot of opportunities in the world of science, such as to do the cutting-edge research and discuss it with world-leading physicists. These opportunities had shown me what it was like to do science and what research I really liked.

Dr David Horsell had become my supervisor at the end of my second year, and whom I have worked with up to the end of my PhD. I am very grateful to him for taking me on and for making sure that the last year of the PhD went smoothly. By the latter I mean very quick response to all my questions and requests regarding experimental research, preparation for conferences, help with visas.

I am very thankful to the students and postdocs who I have worked with and who have taught me how to measure, fabricate and characterise graphene samples. These people are Fedor Tikhonenko, Roman Gorbachev, Adam Price, David Horsell, Alexey Kaverzin, Sam Hornett, Fred Withers and Peter Hale.

I would also like to thank Dr Massimo Ghidini who was a visitor scientist during my first year at Exeter and who, together with David Horsell, taught me the operation of an atomic force microscope.

In the middle of my PhD Dr Andrei Shytov, Dr Saverio Russo and Dr Jens Martin joined our group and I am thankful to them for sharing their knowledge and experience with me. They are very interesting people and it was a pleasure to meet and work with them.

Of course, many thanks to David Manning and Adam Woodgate who have been continuosly supplying us with liquid helium, without which none of my experiments would have been possible.

Our technician, Paul Wilkins, who is always there when we need technical help, deserves a special gratitude. Together with Paul we were making dipping probes and accessories for measurements. He helps us solve problems when equipment breaks. Apart from being extremely skillful, he also knows many interesting things, so I always enjoyed talking to him. It was a great pleasure working with him.

I would especially like to thank Dr Eros Mariani. He is not only a very bright

physicist, but also a wonderful person. His endless support and help during my PhD as well as his patience with me have made me feel comfortable and confident about what I do. His way of understanding, explaining and seeing things is very rare in my view. I am very lucky to know him and learn from him.

Contents

Abstract 2

Acknowledgements 4

Contents 6

List of Figures 9

List of Tables 17

Introduction 18

1 Basic concepts 21

1.1 Crystal structure of monolayer graphene 21

1.2 Energy dispersion relation 22

1.3 Properties of electrons in graphene 28

1.3.1 Density of States 28

1.3.2 Chirality of charge carriers 29

1.3.3 Berry phase 31

2 Theoretical background 32

2.1 Classical and quantum Hall effect 32

2.2 Shubnikov-de Haas effect 38

2.3 Weak localisation of charge carriers 39

2.4 Electron-electron interaction in the presence of disorder 46

2.5 Methods of separation of the quantum corrections 50

2.6 Electron-phonon interaction 52

2.7 Spin-orbit interaction 54

2.8 Variable-range hopping 56
2.9 Atomic force microscopy 57
2.10 Raman spectroscopy 58

3 Fabrication, sample characterisation and instrumentation 61
3.1 Fabrication of graphene transistors 61
3.2 Determining the number of layers 64
3.2.1 Raman spectrum 64
3.2.2 Quantum Hall effect 65
3.2.3 AFM topography 66
3.3 Determining the carrier density in graphene from SdH oscillations . . 67
3.4 Instrumentation and measurements 68
3.4.1 Helium-3 cryostat 68
3.4.2 Dilution refrigerator 70

4 Quantum corrections to the conductivity at high temperatures 73
4.1 Field effect in graphene 73
4.2 Weak localisation 75
4.2.1 Transition from weak localisation to antilocalisation 77
4.2.2 Temperature dependence of the dephasing rate 80
4.3 Electron-electron interaction 83
4.3.1 Effect of electron-phonon interaction 86
4.3.2 Separation of the quantum corrections 87

5 Quantum corrections to the conductivity at low temperatures 93
5.1 Weak localisation 93
5.1.1 Temperature dependence of the dephasing length 96
5.1.2 Mechanisms of the saturation of the dephasing length 97
5.2 Temperature dependence of the conductivity 99
5.2.1 Electron-electron interaction correction 101
5.3 A comparison of L_{s} determined from MC and $\sigma(T)$ 103
5.3.1 Spin-related phenomena in previous papers on weak localisation 105
5.3.2 Comparison of L_s determined by different experimental groups 105
5.3.3 Speculations about the short spin coherence length 106

6 Electron transport in ion irradiated graphene **109**

6.1 Light irradiation. Weak localisation regime 109

6.1.1 Weak localisation and electron-electron interaction corrections 110

6.1.2 Inter-valley scattering length 112

6.2 Heavy irradiation. Strong localisation regime. Variable-range hopping 113

7 Conclusions **117**

Bibliography **119**

List of Figures

1.1 (a) Graphene crystal lattice consists of two sublattices A (red triangle) and B (blue triangle). The unit cell (dashed diamond) has two atoms. Vectors $\vec{a}_1$ and $\vec{a}_2$ are the lattice unit vectors, $\vec{b}_1$, $\vec{b}_2$ and $\vec{b}_3$ are the nearest-neighbor vectors. (b) The corresponding Brillouin zone. K and K$'$ are the Dirac points. 22

1.2 Energy spectrum of graphene. 25

1.3 (a) K valley and the linear dispersion relation. (b) and (c) The DOS in graphene and 2D-systems with a parabolic dispersion relation, respectively. 29

1.4 The two valleys K and K$'$ in graphene. The valence ($E < 0$) and conduction bands ($E > 0$) cross each other at the so called Dirac point. Arrows indicate the direction of the pseudospin. The projection of the pseudospin on the direction of the wave vector (chirality) is positive, $\xi = +1$, for electrons in the K valley and negative, $\xi = -1$, for electrons in the K$'$ valley. 30

2.1 The circuit for the Hall effect measurements. The current $\vec{j}$ flows from source to drain and four voltage contacts (shaded areas) allow the measurements of the voltage along, V_{xx}, and across the sample, V_{xy}. Electrons (circles with a minus sign) move with velocity $\vec{\nu}$ in the direction opposite to the current. In the presence of the perpendicular magnetic field electron trajectories bend (shown in the figure) and accumulation of the negative charge occurs on one edge of the sample and the positive charge on the other one. Accumulation stops when the Lorentz force equates the electric force. In this equilibrium state the transverse or Hall voltage, V_{xy}, can be measured. 33

2.2 (a) The density of states in a conventional (with a parabolic dispersion relation) two-dimensional system at zero magnetic field. (b) For a non-zero magnetic field the DOS in an ideal 2D system is a series of δ - functions separated by $\hbar\omega/2$. (c) Same as in (b) but in the presence of disorder that broadens the peaks in the DOS. The hatched area corresponds to the localised states and the gray area to the extended states. The solid vertical line is a position of the Fermi level ε_F. 36

2.3 Various paths, (a) and (b), for an electron (blue circle) to go from point A to point B. Probability amplitudes along each path are A_1 and A_2. Black circles correspond to scattering centres. 39

2.4 Limiting cases to observe WL or WAL in graphene. The upper curve corresponds to WL and the situation when $\tau_*^{-1} \gg \tau_\varphi^{-1} \sim \tau_i^{-1}$. The bottom curve is the case of a clean sample (no intra- or inter-valley scattering), $\tau_\varphi^{-1} \gg \tau_i^{-1}, \tau_*^{-1}$. Under certain conditions no weak localisation can be observed (middle curve): $\tau_*^{-1} \gg \tau_\varphi^{-1} \gg \tau_i^{-1}$. 43

2.5 Conditions to observe WL and WAL in graphene. Orange curve corresponds to $\Delta\sigma(B) = 0$ in equation (2.28). The ratios of τ_φ/τ_* and τ_φ/τ_i, for which $\Delta\sigma(B) > 0$ (area above the curve), indicate WL. In the opposite case (area below the curve) they indicate WAL. 44

2.6 Nature of the electron-electron interaction correction. Electron waves following paths A and B scatter off an impurity (black ball) and the Friedel oscillations (semicircles) and interfere constructively. 47

2.7 (a) Elliot-Yafet mechanism of spin dephasing: the direction of spin (red arrow) changes every time an electron (blue circle) scatters off impurities (black circles) or phonons. (b) Dyakonov-Perel mechanism: the SOI induces a magnetic field that changes its direction randomly during electron scattering 55

2.8 Scattering processes that take place in the Raman effect giving rise to (a) intra-valley one-phonon G peak, (b) defect-assisted intra-valley D′ peak (c) intra-valley two-phonon 2D′ peak, (d) defect-assisted inter-valley D peak, (e) inter-valley two-phonon 2D peak. 59

3.1 An optical image of monolayer graphene (encircled area) on top of Si/SiO_2. 62

3.2 Schematic of the transistor. The carrier density is tuned by applying a voltage, V_g, between the n-doped silicon and graphene. The current is driven between contacts 1 and 2, the longitudinal resistivity ρ is measured between 3 and 4 (or 5 and 6), and the transverse resistivity between 3 and 5 (or 4 and 6). 63

3.3 The Raman spectrum of graphene. The symmetric 2D peak, G peak and the defect-assisted D peak are shown. The inset shows a fit of the 2D peak with the Lorentzian function. The fit gives the width of the peak at half maximum of ~ 30 cm^{-1}, which indicates that the studied sample is monolayer graphene. 65

3.4 Quantum Hall effect measured at 4.2 K and 14 T. Plateaus at half-integer filling factors prove that the studied samples are monolayers. . . 66

3.5 (a) Atomic force microscopy image of graphene and (b) a profile taken along a blue line in (a). The profile shows a clear step in height of < 1 nm, which indicates that the sample is single layer graphene. . . 66

3.6 (a) Shubnikov-de Haas oscillations at four different carrier densities, which are denoted as regions I, II, III and IV. These regions correspond to 0.2, 1.15, 2.6 and $3.5 \cdot 10^{12}$ cm^{-2}, respectively. The measurements are performed at 4.2 K. (b) SdH oscillations shown for region II as a function of $1/B$. Red crosses correspond to the positions of the peaks in the resistance. 67

3.7 The dependence of the coefficient γ as a function of magnetic field for regions II and III in Fig. 3.6(a). The averaged value of γ is $7.7 \cdot 10^{10}$. 68

3.8 Principle of operation of the ^{3}He system. Picture of the left: the sorb at 30 K releases ^{3}He gas, which condenses passing through the 1 K Pot at 1.2 K. Liquid ^{3}He at 1.2 K is collected in the sample space. Picture on the right: When all ^{3}He has been condensed, the sorb temperature should be reduced to 2 K for it to start pumping the vapour above liquid ^{3}He. The pumping decreases the temperature of ^{3}He down to 0.25 K. 70

3.9 Schematic diagram of the dilution refrigerator. 71

4.1 The resistance of the sample as a function of the carrier density or the gate voltage. The point where the resistance is maximum is the electro-neutrality point (NP). Regions I, II and III correspond to the carrier densities 0.2, 1.15 and 2.6·10^{12} cm^{-2}, respectively, where weak localisation is studied. 75

4.2 (a) The resistance of the sample as a function of the gate voltage measured at 5 K in a narrow window of V_g (shown for region II as an example). For simplicity only four curves, which correspond to different magnetic fields, are shown. (b) The result of averaging of the curves in (a). 76

4.3 Evolution of the magnetoconductivity as a function of the carrier density shown at three different temperatures. The solid curves are fits to equation (2.27). 77

4.4 Evolution of the magnetoconductivity as a function of the temperature. The bottom panel is a zoomed-in view for high temperatures. The solid curves are fits to equation (2.27). 78

4.5 Conditions to observe WL and WAL in graphene. Orange curve corresponds to $\Delta\sigma(B) = 0$ in equation (2.28). The ratios of τ_φ/τ_* and τ_φ/τ_i, for which $\Delta\sigma(B) > 0$ (area above the curve), indicate WL. In the opposite case (area below the curve) they indicate WAL. Point are experimental values found from the analysis of the magnetoconductivity. 79

4.6 Temperature dependence of the dephasing rate. Solid lines are expectations from electron-electron interaction found as a sum of equations (4.1) and (4.3): (a) $\alpha = 1.5, \beta = 0$; (b) $\alpha = 1.5, \beta = 2.5$; (c) $\alpha = 0, \beta = 2.5$. Dotted lines are dephasing rates calculated using equation (4.2). 80

4.7 The gate voltage dependence of the resistivity measured at 5.4 K for three studied samples S1, S2 and S3. The EEI correction to the conductivity is studied in regions I, II and III. 83

4.8 (a) The gate voltage dependence of the resistivity of sample S1 in region II at different temperatures. (b)-(d) The resistivity as a function of temperature for sample S1 for the three studied regions. The solid line in (d) is a fit to equation (2.51). The fit gives $D_a = 18$ eV. 85

4.9 (a) Determination of the position, V_{NP}, of the neutrality point and its resistivity, ρ_{NP}. The upper half of the $\rho(V_g)$ curve is fitted with a Gaussian function. This function is then used to determine V_{NP} and ρ_{NP}. (b) Fluctuations of the NP at different temperatures: $V_{NP} = 3 - 3.3$ V. 86

4.10 (a) Resistivity as a function of temperature for sample S1 in the three studied regions (see Fig. 4.8). The dashed line indicates the contribution from electron-acoustic phonon interaction calculated using equation (2.48) (shifted for convenience) with $D_a = 18$ eV. (b) The conductivity after the phonon contribution has been subtracted. The solid lines show the WL correction to the conductivity. 88

4.11 (a) Resistivity as a function of temperature for sample S2, shown for three regions. The dashed lines indicate the magnitude of the acoustic phonon contribution calculated using equation (2.48) (shifted for convenience) with $D_a = 18$ eV. (b) The conductivity $\Delta\sigma(T) = \sigma(T) - \sigma(T_0)$ at different magnetic fields (the contribution of acoustic phonons with $D_a = 18$ eV has been subtracted). 89

4.12 The electron-electron interaction correction to the conductivity. (a) The results for sample S1 (circles) are obtained by determining the WL correction using equation (2.27) (in region I the results for sample S3 are also displayed by triangles). (b) For sample S2 the WL contribution is suppressed by magnetic field. Solid lines are fits to equation (2.31). Black and blue colors correspond to the subtraction of equation (2.48) with $D_a = 18$ and 21 eV, respectively. 90

5.1 The resistance measured in sample SS1 as a function of magnetic field shown for region I at 30 mK. Three curves correspond to three close values of the gate voltage. 94

5.2 (a) The resistivity dependence on the gate voltage, RV_g, measured at 30 mK in sample SS1. Red circles represent regions where magnetoconductivity is measured. The temperature dependence of the conductivity is measured in regions I, II and III. The left inset shows the gate voltage dependence of the conductivity for the same sample at 30 mK. The right inset shows the valence and conduction bands filled with electrons up to the Fermi energy, ε_F, which is much larger than k_BT in all studied regions. (b) The RV_g curves measured in a temperature range 20 mK - 4.2 K. The left inset shows a zoomed-in region near the neutrality point. The right inset shows the resistivity in a narrow range of the gate voltages in region I. 95

5.3 Magnetoconductivity measured in regions I, II, III and IV at different temperatures. 96

5.4 The temperature dependence of the dephasing length in sample SS1 extracted from MC in regions I, II and III. Different symbols represent different experimental runs. The dotted line shows the saturated value of $L_{\varphi s}$. Solid curve is the expected behavior of the dephasing length due to electron-electron interaction. Error bars at each temperature indicate values of $L_{\varphi s}$, which can be used to fit the MC curves. 97

5.5 The resistance dependences on the gate voltage measured at 30 mK in sample SS2 for different source–drain currents show the absence of electron overheating for 1 and 0.1 nA (this is true also for sample SS1). The inset is a zoomed-in region shown in the main graph by a rectangle. 98

5.6 The temperature dependences of the conductivity, $\Delta\sigma(T) = \sigma(T) - \sigma(T_0)$, where T_0 is the lowest studied temperature. The dependences in the main graphs are shown for sample SS1 for (a) region I, (b) region II and (c) region III. Insets show $\Delta\sigma(T)$ in sample SS2. The solid curves are fits to equation (5.3). The values of the spin coherence lengths in each region are shown for sample SS1. Different symbols in the insets correspond to different experimental runs. 100

5.7 The EEI correction to the conductivity isolated by applying a perpendicular magnetic field of 1 T. The left- and right-hand side graphs correspond to regions III and IV. 101

5.8 (a) The longitudinal magnetoresistivity measured in region I at different temperatures. Fitting solid curves are used to determine the resistivity at the crossing point. The inset shows the same curves after the EEI correction has been subtracted. (b) The transverse magnetoresistivity at different temperatures. The group of lines in the main graph corresponds to raw data and that in the inset shows ρ_{xy} without the EEI correction. (c-d) The temperature dependences of the Hall coefficient shown for regions I and III. The solid lines are linear fits. Different points at each temperature correspond to different magnetic fields. 102

5.9 The EEI correction to the conductivity determined from the temperature dependence of the Hall coefficient for regions I-IV. 103

5.10 The spin coherence length as a function of the mean free path determined from the MC analysis (circles, squares and hexagons) and the temperature dependence of the conductivity, equation (5.3) (diamonds and triangles). Circles and diamonds correspond to sample SS1, squares and triangles - to sample SS2, hexagons - to sample SS3. The solid line is a linear fit to experimental data shown by red circles. Error bars show possible values of L_s that can be used to fit the experimental dependences. 104

5.11 The dependence of the spin coherence length on the mean free path determined by different experimental groups [112–114]. 105

5.12 The dependence of the ratio L_s/l_p on the carrier density for the three studied samples. 106

5.13 The dependence of the ratio L_s/l_p on the inter-valley scattering length for the three studied samples. 107

6.1 The gate voltage dependence of the resistivity measured at different temperatures in sample SS3 after irradiation. The two insets are zoomed-in regions shown in the main graph by rectangles. 110

6.2 (a) The $R(V_g)$ curve at 4 K. Arrows indicate the studied regions of the gate voltage (carrier density). (b) The temperature dependence of the resistivity shown for region II. The solid line is the electron–acoustic phonon contribution to ρ with the deformation potential of 30 eV. (c - i) The temperature dependence of the conductivity in seven regions of the gate voltage plotted in the semilogarithmic scale. Regions I, II and III correspond to 3, 16 and 36 V with respect to the neutrality point, respectively, and regions IV, V and VI to -3, -16 and -36 V with respect to the NP. The measurements are shown for two experimental runs. Solid lines in the $\Delta\sigma(T)$ dependences are linear fits. 111

6.3 (a, b) Magnetoconductivity measured in regions I and II at different temperatures. (c, d) The temperature dependence of the conductivity in the same regions. The coefficient A from equation (2.31) is shown. Different symbols correspond to different experimental runs. 112

6.4 The resistivity as a function of the gate voltage measured after ion bombardment at different temperatures. The curves are shifted to zero gate voltage. 113

6.5 The temperature dependence of the resistivity before (left column) and after (right column) ion irradiation measured at the neutrality point (NP) and in regions I, II and III. These regions are the same as in all previous experiments. Before ion bombardment the resistivity was measured first at increasing temperatures (triangles), then at decreasing temperatures (squares), and after bombardment only at decreasing T. 115

6.6 The resistivity as a function of temperature for a heavily irradiated sample. Experimental points follow the $\exp(T^{-1/3})$ dependence, which indicates that electron transport occurs via variable-range hopping. 116

List of Tables

4.1 The inter- and intra-valley scattering times (in ps) extracted from the analysis of the MC. Errors come from the fitting procedure. 78

4.2 Electron mobility μ (in $cm^2V^{-1}s^{-1}$) at 5 K for three regions of the carrier density in samples S1, S2 and S3. Characteristic scattering times τ_i and τ_* (in ps) are also shown for sample S1. 84

5.1 Sample parameters: dimensions (in μm) of the samples and mobilities μ (in $cm^2V^{-1}s^{-1}$) in regions I, II and III. 95

5.2 Approximate dependence on electronic density n of the ratio of the spin coherence length to the mean free path L_s/l_p using estimates from recent literature [120–124]. 106

6.1 Sample parameters before and after ion bombardment. The resistivity is given at the neutrality point at different temperatures and the mobility (in $cm^2V^{-1}s^{-1}$) at 20 V with respect to the NP. The exposure time for irradiation is also shown. 116

Introduction

The year 2004 was marked by the "discovery" of a fascinating material – graphene. It is a sheet of carbon only one atom thick. Since then it has triggered a huge number of research activities aimed at uncovering what this material is capable of. Finally, in 2010 its discoverers were awarded the Nobel Prize for Physics. Six years after its discovery, graphene has already shown itself to be the strongest material in nature, the best ever conductor of heat and an excellent conductor of electricity. These properties are already leading to graphene becoming part of our everyday lives in the near future. For example, it is an excellent candidate for touch screens and thin and flexible monitors. Apart from practical applications, graphene has become a test bed to study fundamental physical phenomena. Many interesting properties of graphene have already been shown, but many still remain to be revealed. Our research is aimed at uncovering and understanding new physics in the conduction of electrons in graphene. The project is about how electrons move and interact with their surroundings.

In our every day lives we deal with objects that can be touched and seen with the naked eye. Such objects obey classical laws of physics. But as we shrink the size of a system, the properties of materials deviate from those observed in 'classical' objects, and quantum physics comes into play. For example, in the presence of imperfections of the crystal structure electron waves scatter off the potential created by the imperfections and interfere with each other. This gives rise to many interesting phenomena, such as quantum corrections to the conductivity: weak localisation and antilocalisation of charge carriers and electron-electron interaction in the presence of disorder. Investigation of the quantum correction in graphene under different experimental conditions is this main focus of the thesis.

The structure of the thesis is the following.

In Chapter 1 we start with basic concepts and describe interesting properties of graphene, which we use throughout the thesis.

In Chapter 2 we discuss different quantum phenomena and highlight remarkable differences between graphene and other two-dimensional systems. In this chapter we explain the origins of these phenomena and provide the theoretical background needed to understand the physics in graphene.

In Chapter 3 fabrication techniques and equipment for measurements are presented. Here we show how graphene can be produced by mechanical exfoliation of graphite using adhesive tape. Graphite can be imagined as a stack of graphene layers being held together by weak Van der Waals forces. The exfoliation technique involves peeling off the layers and depositing them on top of a substrate. However, their number in a sample can not be controlled. We discuss the ways of identifying flakes of a certain thickness and show different methods of determining the number of layers. Field-effect transistors are produced from the flakes and loaded in low-temperature cryostats for measurements. We discuss principles of operation of different cryostats and show specifics of each of them.

In Chapter 4 we discuss our measurements of the quantum corrections to the conductivity: weak localisation and electron-electron interaction in the presence of disorder. We start with low temperatures, 5 K, and show a transition from weak localisation to antilocalisation as a function of the carrier density and temperature. We raise the temperature to 200 K and surprisingly still observe quantum interference. We discuss the reasons behind this by studying the dephasing time. This is the time during which an electron loses information about its phase. It plays a very important role in the interference of electron waves. The quantum corrections depend similarly on temperature. Therefore, in order to study them, they have to be separated. We present different methods of separating the two corrections and compare them with each other. The electron-electron interaction correction is then studied in different samples at temperatures between 0.25 and 40 K. We show a new form of the expression for the interaction correction compared to other two-dimensional systems and determine the Fermi-liquid parameter.

In Chapter 5 we study the quantum corrections at temperatures between 20 mK and 4 K. In addition to the methods of their separation described in the previous chapter, we demonstrate one more method. In the studies of weak localisation at

temperatures below 0.1 K we observe a saturation of the dephasing length. We consider possible origins of this saturation and discuss in detail two of them: spin-orbit interaction and electron scattering off vacancies. Here we also determine the spin coherence length in graphene, which despite many theories turns out to be very short. We try to explain why this is so and show how it can be overcome. We also demonstrate how to tune the spin coherence length by controlling the level of disorder. The spin coherence length is also determined from the temperature dependence of the conductivity. Its values are found to be in good agreement with those extracted from the weak localisation studies.

In Chapter 6 we intentionally irradiate graphene samples with gallium ions and study electron transport through such devices. The results are compared with those obtained before ion bombardment. We show that as we increase the dosage of irradiation, we move from weak to strong localisation regime. In the former case electron transport at low temperatures is governed by the quantum corrections, and in the latter case by variable range hopping. We also investigate how elastic scattering is affected by irradiation.

In the last chapter we summarise all our findings.

Chapter 1

Basic concepts

In this chapter we discuss basic concepts, which are necessary since they will be used throughout the thesis. We start with the crystal structure of monolayer graphene and use the tight-binding approximation to derive the linear dispersion relation – one of the unusual properties of this material. Other properties of electrons in graphene include chirality of charge carriers and the Berry phase. Each of these will be discussed in detail.

1.1 Crystal structure of monolayer graphene

Graphene is a monolayer of carbon atoms arranged in a honeycomb structure [1], Fig. 1.1(a). Its crystal lattice consists of two interpenetrating triangular sublattices, the atoms of which are denoted by A and B in the figure. The lattice vectors, which are the vectors between neighboring carbon atoms in a given sublattice, are $\vec{a}_1 = (0;\ a)$ and $\vec{a}_2 = (a\sqrt{3}/2;\ a/2)$, where $a = 1.42 \times \sqrt{3} = 2.46$ Å and the carbon-carbon distance is 1.42 Å. The vectors between any two atoms (irrespective of sublattice) are the nearest-neighbor vectors: $\vec{b}_1 = (-a/2\sqrt{3};\ a/2)$, $\vec{b}_2 = (a/\sqrt{3};\ 0)$ and $\vec{b}_3 = (-a/2\sqrt{3};\ -a/2)$. Atoms A and B form a unit cell, a minimal number of atoms whose repetition in space produces a crystal lattice, shown by the dashed diamond in the figure. In reciprocal space, this leads to two inequivalent points K and K′ in the Brillouin zone, Fig. 1.1(b), which are called Dirac points. The reciprocal lattice vectors are $\vec{\delta}_1 = (1/a\sqrt{3};\ -1/a)$ and $\vec{\delta}_2 = (-2/a\sqrt{3};\ 0)$.

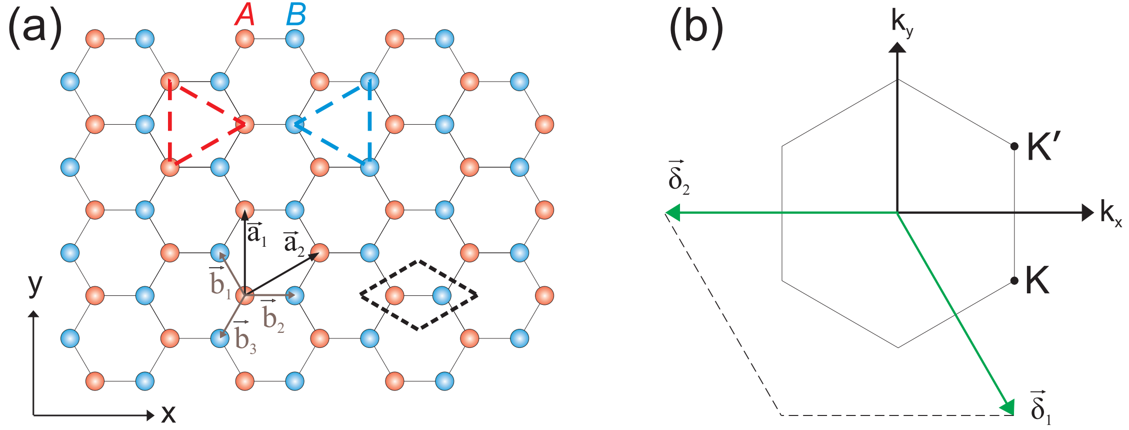

Figure 1.1: (a) Graphene crystal lattice consists of two sublattices A (red triangle) and B (blue triangle). The unit cell (dashed diamond) has two atoms. Vectors $\vec{a}_1$ and $\vec{a}_2$ are the lattice unit vectors, $\vec{b}_1$, $\vec{b}_2$ and $\vec{b}_3$ are the nearest-neighbor vectors. (b) The corresponding Brillouin zone. K and K′ are the Dirac points.

1.2 Energy dispersion relation

The band structure of graphene is calculated [2] using the tight binding approximation. Graphene's honeycomb crystal lattice is not a Bravais lattice, but the two triangular sublattices, which it consists of, are. As there are two atoms in the unit cell, A and B, electron wave functions that correspond to A and B are

$$\begin{cases} \varphi_A = \frac{1}{\sqrt{N}} \sum\limits_A e^{2\pi i \vec{k}\vec{r}_A} \chi(\vec{r} - \vec{r}_A) \\ \varphi_B = \frac{1}{\sqrt{N}} \sum\limits_B e^{2\pi i \vec{k}\vec{r}_B} \chi(\vec{r} - \vec{r}_B) \end{cases} , \tag{1.1}$$

where $\vec{r}_A$ and $\vec{r}_B$ are the positions of atoms A and B, respectively, N is the number of the unit cells in the crystal, and $\chi(\vec{r})$ is the wave function of electrons on isolated carbon atoms. To form φ_A and φ_B we take χ in N unit cells, which differ by a phase factor $e^{2\pi i \vec{k}\vec{r}_{A/B}}$, and then sum over the lattice vectors $\vec{r}_A$ and $\vec{r}_B$ of the whole crystal.

The wave function of electrons in the solid is expressed by a linear combination of functions φ_A and φ_B:

$$\Psi = \varphi_A + \lambda \varphi_B , \tag{1.2}$$

where λ is a coefficient to be optimised to minimize the energy E. The eigenvalues

E of the function Ψ are calculated from the Schrödinger equation: $H\Psi = E\Psi$. We multiply this equation by Ψ^* from both sides and integrate:

$$E = \frac{\langle\Psi|H|\Psi\rangle}{\langle\Psi|\Psi\rangle} = \frac{\int \Psi^* H \Psi d\vec{r}}{\int \Psi^* \Psi d\vec{r}} \ . \tag{1.3}$$

In this equation H represents the kinetic energy of an electron: $H = p^2/m$. Substitution of Ψ from equation (1.2) into (1.3) gives

$$E = \frac{\int(\varphi_A^* + \lambda\varphi_B^*)H(\varphi_A + \lambda\varphi_B)d\vec{r}}{\int(\varphi_A^* + \lambda\varphi_B^*)(\varphi_A + \lambda\varphi_B)d\vec{r}} \ . \tag{1.4}$$

We neglect the overlap between electrons on different atoms: $\int \varphi_A\varphi_B = 0$. Then

$$E = \frac{\int(\varphi_A^* H\varphi_A + \lambda^2\varphi_B^* H\varphi_B + \lambda\varphi_B^* H\varphi_A + \lambda\varphi_A^* H\varphi_B)d\vec{r}}{\int(\varphi_A^*\varphi_A + \lambda^2\varphi_B^*\varphi_B)d\vec{r}} \ . \tag{1.5}$$

Introducing the so called transfer integrals $H_{AA} = \int \varphi_A^* H\varphi_A d\vec{r}$, $H_{BB} = \int \varphi_B^* H\varphi_B d\vec{r}$, $H_{AB} = \int \varphi_A^* H\varphi_B d\vec{r}$, $H_{BA} = \int \varphi_B^* H\varphi_A d\vec{r}$ and overlap integrals $S_1 = \int \varphi_A^*\varphi_A d\vec{r}$, $S_2 = \int \varphi_B^*\varphi_B d\vec{r}$ and taking into account that $S_1 = S_2 = S$, $H_{AA} = H_{BB}$ and $H_{AB} = H_{BA}^*$ we get:

$$E = \frac{H_{AA} + \lambda^2 H_{BB} + \lambda(H_{AB} + H_{BA})}{S(1+\lambda^2)} = \frac{1}{S}\left[H_{AA} + \frac{2\lambda}{1+\lambda^2}H_{AB}\right] \ . \tag{1.6}$$

To find the values of λ that give the minimum of E, we take the derivative of E with respect to λ and equate it to zero, $E'_\lambda = 0$:

$$E'_\lambda = \frac{2(1+\lambda^2) - 2\lambda\cdot\lambda}{(1+\lambda^2)^2} = 0 \ .$$

From this equation we find $\lambda = \pm 1$ and the minimised value of E is therefore:

$$E = \frac{1}{S}(H_{AA} \pm H_{AB}) \ . \tag{1.7}$$

We assume that the atomic wave function is normalised [3], such that $S = 1$. To calculate H_{AA} and H_{AB} we substitute the wave functions of electrons from different

sublattices, equations (1.1), to $H_{AA} = \int \varphi_A^* H \varphi_A d\vec{r}$ and $H_{AB} = \int \varphi_A^* H \varphi_B d\vec{r}$:

$$H_{AA} = \frac{1}{N} \sum_{A,\ A'} e^{-2\pi i \vec{k}(\vec{r}_A - \vec{r}_{A'})} \int \chi^*(\vec{r} - \vec{r}_A) H \chi(\vec{r} - \vec{r}_{A'}) d\vec{r} \ , \tag{1.8}$$

$$H_{AB} = \frac{1}{N} \sum_{A,\ B} e^{-2\pi i \vec{k}(\vec{r}_A - \vec{r}_B)} \int \chi^*(\vec{r} - \vec{r}_A) H \chi(\vec{r} - \vec{r}_B) d\vec{r} \ , \tag{1.9}$$

where $\vec{r}_A - \vec{r}_B = \vec{a}/\sqrt{3}$ is the distance between two neighboring carbon atoms, A and A' are two carbon atoms in sublattice A.

The maximum contribution to H_{AA} in equation (1.8) comes from $\vec{r}_A = \vec{r}_{A'}$. This gives the energy of the isolated atom $E_0 = \int \chi^*(\vec{r}) H \chi(\vec{r}) d\vec{r}$. The next order contribution comes from $\vec{r}_A = \vec{r}_{A'} - \vec{a}_1$, where $\vec{a}_1$ is a vector between two neighbors in sublattice A (it can also be $\vec{a}_2$), and gives $\gamma_0' = -\int \chi^*(\vec{r} - \vec{a}_1) H \chi(\vec{r}) d\vec{r}$.

Similarly, in equation (1.9) the maximum contribution arises when A and B are nearest neighbors. Then $\gamma_0 = -\int \chi^*(\vec{r} - \vec{b}_1) H \chi(\vec{r}) d\vec{r}$, where $\vec{b}_1$ is a vector between atoms A and B (in can also be $\vec{b}_2$).

Now we can rewrite equations (1.8) and (1.9):

$$H_{AA} = E_0 - 2\gamma_0'(\cos 2\pi k_y a + 2 \cos \pi k_x a\sqrt{3} \cos \pi k_y a) \ .$$

Similarly,

$$H_{AB} = -\gamma_0(e^{-2\pi i k_x (a/\sqrt{3})} + 2 \cos \pi k_y a \cdot e^{2\pi i k_x (a/2\sqrt{3})}) \ .$$

Then

$$H_{AB} = \gamma_0 \sqrt{1 + 4 \cos^2 \pi k_y a + 4 \cos \pi k_y a \cos \pi k_x \sqrt{3} a} \ .$$

Thus, the energy is (see equation (1.7))

$$\begin{aligned} E = E_0 - 2\gamma_0'(\cos 2\pi k_y a + 2 \cos \pi k_x a\sqrt{3} \cos \pi k_y a) \pm \\ \pm\gamma_0 \sqrt{1 + 4 \cos^2 \pi k_y a + 4 \cos \pi k_y a \cos \pi k_x \sqrt{3} a} \ . \end{aligned} \tag{1.10}$$

Near the K and

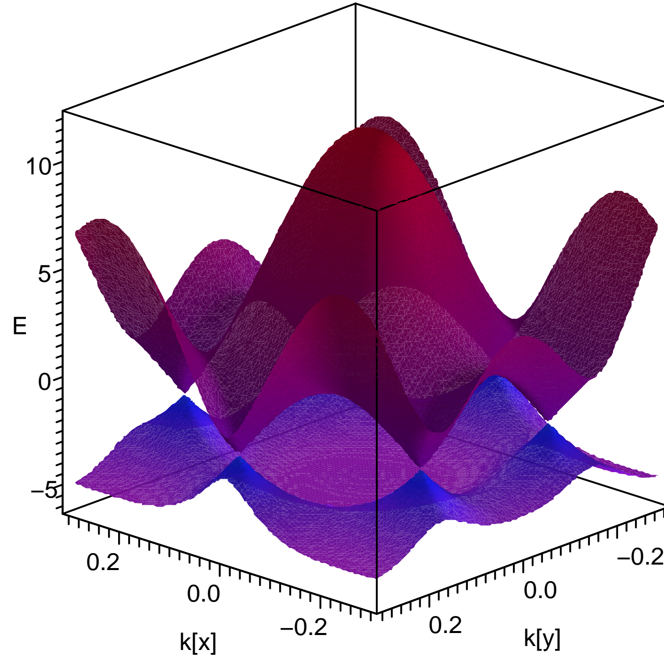

Figure 1.2: Energy spectrum of graphene.

$$E = E_0 + 3\gamma_0^{'} \pm \sqrt{3}\pi\gamma_0|\vec{k} - \vec{K}|a - 3\pi^2\gamma_0^{'}|\vec{k} - \vec{K}|^2 a^2 \ , \tag{1.11}$$

where $|\vec{k} - \vec{K}|$ means that we deal with wave vectors with respect to the K point.

Taking into account only nearest carbon neighbors ($\gamma_0^{'} = 0$) we get the energy dispersion relation in graphene:

$$|E - E_0| = \pm\sqrt{3}\pi\gamma_0 a|\vec{k} - \vec{K}| \ , \tag{1.12}$$

where '+' corresponds to electrons and '-' corresponds to holes. The energy dispersion law with $\gamma_0, \gamma_0^{'} \neq 0$ is shown in Fig. 1.2.

From equations (1.10) and (1.12) one can see that if only nearest neighbors are taken into account, then the energy dependence on the wave vector is symmetric and linear in the vicinity of the K and K′ points. However, if $\gamma_0^{'} \neq 0$, then the energy dispersion relation becomes assymetric and non-linear.

In order to find the form of the Hamiltonian for electrons in graphene, we write it using creation and annihilation field operators a^+ and a, respectively, for sublattice A. Similarly one can define creation and annihilation operators, b^+ and b, for

sublattice B. Then the Hamiltonian takes the form [4–6]:

$$H = -\gamma_0 \sum_{\vec{r}} \sum_{j=1}^{3} a^+(\vec{r}) b(\vec{r} + \vec{b}_j) + b^+(\vec{r}) a(\vec{r} + \vec{a}_j) \ . \tag{1.13}$$

Here we neglected the contribution from the next-nearest neighbors, i.e. $\gamma_0' = 0$. The Fourier transforms of the creation and annihilation operators are

$$\begin{aligned} a^+(\vec{r}) = \int \frac{d^2\vec{k}}{(2\pi)^2} e^{-i\vec{k}\vec{r}} a^+(\vec{k}) \ , \quad b^+(\vec{r}) = \int \frac{d^2\vec{k}'}{(2\pi)^2} e^{-i\vec{k}'\vec{r}} b^+(\vec{k}') \ , \\ a(\vec{r}) = \int \frac{d^2\vec{k}}{(2\pi)^2} e^{i\vec{k}\vec{r}} a(\vec{k}) \ , \quad b(\vec{r}) = \int \frac{d^2\vec{k}'}{(2\pi)^2} e^{i\vec{k}'\vec{r}} b(\vec{k}') \ . \end{aligned} \tag{1.14}$$

Combining equations (1.13) and (1.14) we get:

$$\begin{aligned} H = -\gamma_0 \sum \sum \int \frac{d^2\vec{k}}{(2\pi)^2} e^{-i\vec{k}\vec{r}} a^+(\vec{k}) \int \frac{d^2 k'}{(2\pi)^2} e^{i\vec{k}'(\vec{r}+\vec{b}_j)} b(\vec{k}') - \\ -\gamma_0 \sum \sum \int \frac{d^2\vec{k}'}{(2\pi)^2} e^{-i\vec{k}'\vec{r}} b^+(\vec{k}') \int \frac{d^2\vec{k}}{(2\pi)^2} e^{i\vec{k}(\vec{r}+\vec{a}_j)} a(\vec{k}) = \\ = -\gamma_0 \int \frac{d^2\vec{k}}{(2\pi)^2} a^+(\vec{k}) \int \frac{d^2\vec{k}'}{(2\pi)^2} \sum e^{i(\vec{k}'-\vec{k})\vec{r}} \sum_{j=1}^{3} e^{i\vec{k}'\vec{b}_j} b(\vec{k}') + c.\ c. \ , \end{aligned} \tag{1.15}$$

where $c.\ c.$ stands for complex conjugate. Taking into account that $\sum_{\vec{r}} e^{i(\vec{k}'-\vec{k})\vec{r}} = 2\pi^2 \delta(\vec{k}' - \vec{k})$, integration over $\vec{k}'$ gives:

$$H = -\gamma_0 \int \frac{d^2\vec{k}}{(2\pi)^2} \left[a^+(\vec{k}) \sum_{j=1}^{3} e^{i\vec{k}\vec{b}_j} b(\vec{k}) + b^+(\vec{k}) \sum_{j=1}^{3} e^{-i\vec{k}\vec{a}_j} a(\vec{k}) \right] \ . \tag{1.16}$$

Now we can write our Hamiltonian in the form [4–6]

$$H = \int \frac{d^2\vec{k}}{(2\pi)^2} \psi^+(\vec{k}) \tilde{H} \psi(\vec{k}) \ , \tag{1.17}$$

where $\psi^+(\vec{k}) = \left(a^+(\vec{k}),\ b^+(\vec{k})\right)$, $\psi(\vec{k}) = \left(a(\vec{k}),\ b(\vec{k})\right)^T$ and

$$\tilde{H} = \begin{pmatrix} 0 & -\gamma \sum_{j=1}^{3} e^{i\vec{k}\vec{b}_j} \\ -\gamma \sum_{j=1}^{3} e^{i\vec{k}\vec{a}_j} & 0 \end{pmatrix} \ . \tag{1.18}$$

The Hamiltonian can be simplified near the K and K′ points. In this case it takes the following form:

$$H = \hbar\nu_F(\alpha_1 k_x + \alpha_2 k_y)\ , \tag{1.19}$$

where the Fermi velocity $\nu_F = \sqrt{3}a\gamma_0/2\hbar$ and

$$\alpha_1 = \begin{pmatrix} \sigma_i & 0 \\ 0 & -\sigma_i \end{pmatrix}\ , \tag{1.20}$$

$$\sigma_1 = \begin{pmatrix} 0 & 1 \\ 1 & 0 \end{pmatrix} \qquad \sigma_2 = \begin{pmatrix} 0 & -i \\ i & 0 \end{pmatrix} \tag{1.21}$$

are the Pauli matrices.

Thus, for electrons in the K valley the Hamiltonian is

$$H = \hbar\nu_F \begin{pmatrix} 0 & k_x - ik_y \\ k_x + ik_y & 0 \end{pmatrix}\ . \tag{1.22}$$

Since $k_x = -i\frac{\partial}{\partial x}$ and $k_y = -i\frac{\partial}{\partial y}$, then

$$H = -i\hbar\nu_F \begin{pmatrix} 0 & i\frac{\partial}{\partial x} + \frac{\partial}{\partial y} \\ -i\frac{\partial}{\partial x} + \frac{\partial}{\partial y} & 0 \end{pmatrix}\ . \tag{1.23}$$

Representing the wave function as a two component column

$$\Psi = \begin{pmatrix} \phi \\ \chi \end{pmatrix} \tag{1.24}$$

we arrive at the system of equations that comes from the Schrödinger equation:

$$\begin{cases} -i\hbar\nu_F\left(\frac{\partial\chi}{\partial x} - i\frac{\partial\chi}{\partial y}\right) = E\phi \\ -i\hbar\nu_F\left(\frac{\partial\phi}{\partial x} + i\frac{\partial\phi}{\partial y}\right) = E\chi \end{cases}\ . \tag{1.25}$$

We substitute χ from the second equation into the first one and get:

$$\frac{\partial^2 \phi}{\partial x^2} + \frac{\partial^2 \phi}{\partial y^2} = -\frac{E^2}{\hbar^2 \nu_F^2} \phi \ . \tag{1.26}$$

The solution of this wave equation is $\phi = (1/\sqrt{2})\ e^{ik_x x + ik_y y}$. We substitute this solution in the second equation in (1.25):

$$\chi = \frac{\hbar \nu_F (k_x + ik_y)}{E} \frac{1}{\sqrt{2}} e^{ik_x x + ik_y y} = \pm \frac{(k_x + ik_y)}{\sqrt{k_x^2 + k_y^2}} \frac{1}{\sqrt{2}} e^{ik_x x + ik_y y} = = \pm e^{i\theta}\ \frac{1}{\sqrt{2}} e^{ik_x x + ik_y y}, \tag{1.27}$$

where $\theta = \arctan(k_y/k_x)$ and $+/-$ corresponds to electrons/holes.

Thus, the two component electron wave function takes the form:

$$\Psi = \frac{1}{\sqrt{2}} \begin{pmatrix} 1 \\ \pm e^{i\theta} \end{pmatrix} e^{ik_x x + ik_y y} \ . \tag{1.28}$$

1.3 Properties of electrons in graphene

1.3.1 Density of States

Due to the linear dispersion relation, equation (1.12) and Fig. 1.3(a), the density of states (DOS – the number of states per unit volume and per unit energy) in graphene is different compared to that in conventional two-dimensional systems, which have a parabolic dispersion relation. Indeed, the total number of states is $N_s = gVV_\phi/V_1$, where g is the spin and valley degeneracy, V_ϕ is the phase volume, V_1 is the phase volume per one state and V is the volume in the coordinate space. Substituting $V_\phi = \pi p^2 = \pi(\hbar k)^2$ and $V_1 = (2\pi\hbar)^2$ we get $N_s = gVk^2/4\pi$. Since $E = \hbar k \nu_F$, the DOS is

$$\nu(E) = \frac{1}{V}\frac{dN_s}{dE} = \frac{1}{V}\frac{dN_s}{dk}\frac{dk}{dE} = \frac{g}{4\pi}\frac{2k}{\hbar\nu_F} = \frac{gE}{2\pi(\hbar\nu_F)^2} = \frac{2\varepsilon_F}{\pi(\hbar\nu_F)^2} \ , \tag{1.29}$$

where ε_F is the Fermi energy. Thus, the DOS in graphene depends linearly on energy (Fig. 1.3(b)). For comparison, the DOS in 2D-systems with a parabolic dispersion relation is $\nu(E) = gm/\pi\hbar^2$ (it is calculated similarly with the only difference being

$E = \hbar^2 k^2/(2m)$, where m is the electron mass), i.e. it is constant, Fig. 1.3(c).

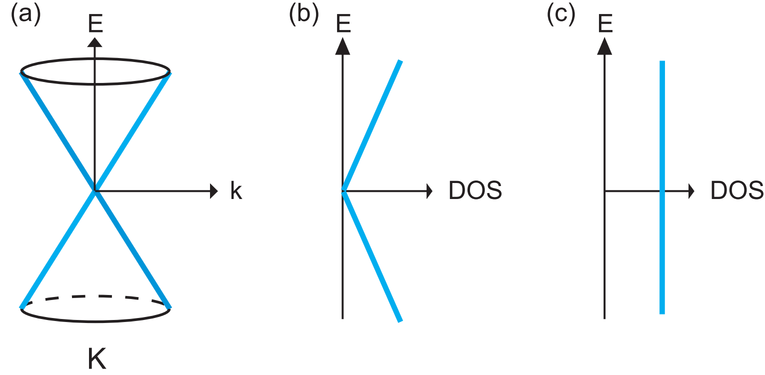

Figure 1.3: (a) K valley and the linear dispersion relation. (b) and (c) The DOS in graphene and 2D-systems with a parabolic dispersion relation, respectively.

Using the expession for the DOS we can calculate the carrier density in graphene:

$$n = \int_0^{\varepsilon_F} \nu(E) f(E)\,\mathrm{d}E = \int_0^{\varepsilon_F} \frac{2E}{\pi(\hbar\nu_F)^2}\mathrm{d}E = \frac{\varepsilon_F^2}{\pi(\hbar\nu_F)^2} = \frac{k_F^2}{\pi}\,, \tag{1.30}$$

where $f(E)$ is the Fermi-Dirac distribution. The carrier density is calculated at zero temperature, for which $f(E) = 1$ and the limits of integration are 0 and ε_F.

1.3.2 Chirality of charge carriers

Due to the crystal structure of graphene, electrons in this material have a number of unique properties, which results in a number of interesting quantum phenomena. In order to reflect the fact that there are two sublattices in graphene, a new quantum number was introduced - pseudospin [7]. It has an 'up' state for one sublattice and 'down' state for the other one. The existence of the sublattices, Fig. 1.1(a), leads to the Dirac-like Hamiltonian of electrons, equation (1.22):

$$H = \begin{pmatrix} 0 & \nu_F(p_x - ip_y) \\ \nu_F(p_x + ip_y) & 0 \end{pmatrix} = \nu_F \vec{\sigma}\cdot\vec{p}\,, \tag{1.31}$$

where $\vec{p}$ is momentum.

As it was shown in the previous section, electrons in graphene have a linear

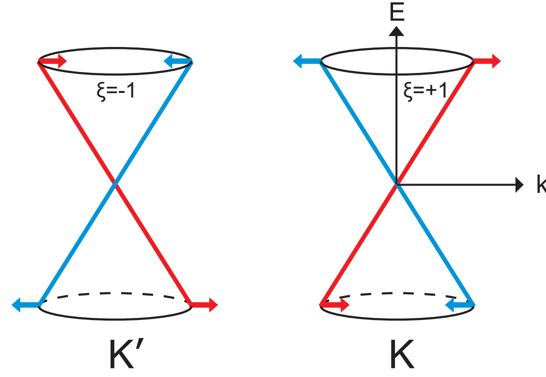

Figure 1.4: The two valleys K and K′ in graphene. The valence ($E < 0$) and conduction bands ($E > 0$) cross each other at the so called Dirac point. Arrows indicate the direction of the pseudospin. The projection of the pseudospin on the direction of the wave vector (chirality) is positive, $\xi = +1$, for electrons in the K valley and negative, $\xi = -1$, for electrons in the K′ valley.

dispersion relation:

$$E = \pm \nu_F |\vec{p}| \ , \tag{1.32}$$

where the $+$ sign correspond to electrons and the $-$ sign to holes. Taking into account the Schrödinger equation $H\Psi = E\Psi$ and combining Eq. (1.31) and (1.32) we arrive at the following relation:

$$\vec{\sigma} \cdot \vec{p} = \pm |\vec{p}| \ . \tag{1.33}$$

Now we can introduce the so called chirality:

$$\xi = \vec{\sigma} \frac{\vec{p}}{|\vec{p}|} = \pm 1 \ . \tag{1.34}$$

Mathematically, chirality is a projection of the pseudospin on the direction of motion. In Fig. 1.4 arrows show the direction of the pseudospin in each valley. One can see that for electrons (at $E > 0$) in the K valley the chirality is $+1$, because the pseudospin is parallel to the momentum. Electrons in the K′ valley have the opposite chirality of -1. Therefore, the chirality is conserved for electrons that are elastically scattered within one valley. Certain kinds of scattering centres can transfer electrons between the valleys, breaking the chirality.

We meet the concept of chirality every day. The most prominent example is our hands. An object is called chiral if it can not be superimposed with its mirror image. For example, our right hand is a mirror image of the left hand, and they can not be superimposed. In graphene the situation is similar. In Fig. 1.1(a) one can see that one sublattice is a mirror image of the other one (red and blue triangles): the two sublattices are not superimposable. The chirality has a profound effect on quantum phenomena in graphene, which will be discussed in Chapter 2.

1.3.3 Berry phase

Another interesting property of electrons in graphene, which is important for understanding the quantum phenomena, also comes from the presence of the two sublattices. It is called the Berry phase. By a gauge tranformation [6] the wave function (equation (1.28)) around the K point can be rewritten as:

$$\Psi \propto \begin{pmatrix} e^{-i\theta/2} \\ e^{i\theta/2} \end{pmatrix} e^{i\vec{p}\cdot\vec{r}} \,. \tag{1.35}$$

The Berry phase is the phase that the electron wave function acquires when the electron completes a full circle. When this happens, the momentum vector of the electron rotates by $\varphi = 2\pi$. Substituting this relation into the electron wave function, equation (1.35), we have

$$\Psi \to \Psi \begin{pmatrix} e^{-i\pi} \\ e^{i\pi} \end{pmatrix} \,. \tag{1.36}$$

As one can see the phase of the wave function changes by π. This is the Berry phase. In Chapter 2 a consequence of the Berry phase π will be discussed in detail.

Chapter 2

Theoretical background

In this Chapter we consider different quantum phenomena, such as the weak localisation and electron-electron interaction corrections to the conductivity, spin-orbit interaction, quantum Hall effect, Shubnikov-de Haas effect, etc. More specifically, we give theoretical explanation of the origin of these phenomena in two-dimensional systems with parabolic dispersion relation and emphasise the differences of their manifestation in graphene. We also discuss different methods of sample characterisation, e.g. atomic force microscopy and Raman spectroscopy.

2.1 Classical and quantum Hall effect

Consider a sample with an electron gas confined in two dimensions. Suppose a magnetic field B is applied perpendicular to the 2D plane. The trajectories of the electrons are bent by a Lorentz force: $\vec{F_L} = -e[\vec{\nu} \times \vec{B}]$, where $\vec{\nu}$ is the velocity and e is the absolute value of the electron charge. This force makes electrons move along cyclotron orbits with radius $R = m\nu/(eB)$, where m is the electron mass, and the Larmor frequency

$$\omega_c = \frac{eB}{m} \ . \tag{2.1}$$

In the presence of an external electric field an electron will experience an electric force $\vec{F_e} = -e\vec{E}$, which induces a net drift velocity of the electron gas perpendicular to $\vec{E}$ and $\vec{B}$. In Fig. 2.1 an electric field has been applied between source and drain, inducing a drift velocity in the X-direction. At the same time the Lorentz force $\vec{F_L}$

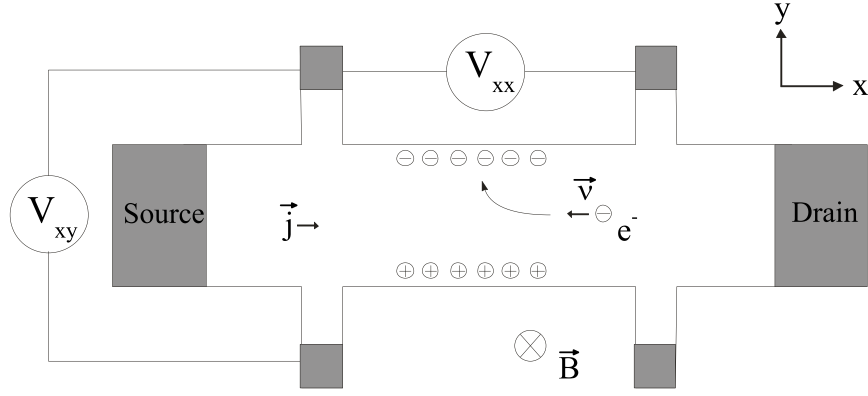

Figure 2.1: The circuit for the Hall effect measurements. The current $\vec{j}$ flows from source to drain and four voltage contacts (shaded areas) allow the measurements of the voltage along, V_{xx}, and across the sample, V_{xy}. Electrons (circles with a minus sign) move with velocity $\vec{\nu}$ in the direction opposite to the current. In the presence of the perpendicular magnetic field electron trajectories bend (shown in the figure) and accumulation of the negative charge occurs on one edge of the sample and the positive charge on the other one. Accumulation stops when the Lorentz force equates the electric force. In this equilibrium state the transverse or Hall voltage, V_{xy}, can be measured.

pushes it along the Y-axis. The total force exerted on the electron is $\vec{F} = \vec{F_L} + \vec{F_e}$ The equation of motion in this case takes the form:

$$\frac{d\vec{p}}{dt} = -e\left(\vec{E} + [\vec{\nu} \times \vec{B}]\right) - \frac{\vec{p}}{\tau} \ , \tag{2.2}$$

where τ is the relaxation time and $\vec{p}/\tau$ is the friction force that comes from electron scattering off impurities. In equilibrium the current flowing along the sample is constant, which means $d\vec{p}/dt = 0$. Then

$$-e\left(\vec{E} + [\vec{\nu} \times \vec{B}]\right) = \frac{\vec{p}}{\tau} \ . \tag{2.3}$$

Since the current density $\vec{j} = -en\vec{\nu}$, then $\vec{\nu} = -\vec{j}/(en)$ and $\vec{p} = -m\vec{j}/(en)$. Substituting the last two relations into equation (2.3) we get:

$$e\left(\vec{E} + \left[-\frac{\vec{j}}{en} \times \vec{B}\right]\right) = \frac{m\vec{j}}{en\tau} \ . \tag{2.4}$$

From this equation we get an expression for the electric field:

$$\vec{E} = \frac{m}{e^2 n\tau}\vec{j} + \frac{1}{en}\left[\vec{B} \times \vec{j}\right] \quad . \tag{2.5}$$

Its projections on X and Y axes are:

$$\begin{cases} E_x = \frac{m}{e^2 n\tau} j_x + \frac{B}{en} j_y = \frac{m}{e^2 n\tau} j_x \\ E_y = \frac{m}{e^2 n\tau} j_y - \frac{B}{en} j_x = -\frac{B}{en} j_x \end{cases} \quad . \tag{2.6}$$

In equilibrium the Lorentz force balances the electric force and the net current perpendicular to the sample edge is zero, $j_y = 0$.

Since $E_\alpha = \rho_{\alpha\beta} j_\beta$, then

$$\begin{cases} \rho_{xx} = \frac{m}{e^2 n\tau} \\ \rho_{yx} = -\frac{B}{en} \end{cases} \quad . \tag{2.7}$$

Negative and positive charge in our system accumulate on the sample edges and a voltage drop $V_{xy} = \frac{B}{en} I_x = R_H I_x$ builds up. Here R_H is the Hall coefficient and I_x is the current passing along the sample. The voltage drop V_{xy} is also called the Hall voltage. This is the nature of the classical Hall effect - accumulation of the positive and negative charges on the sample edges in the presence of the perpendicular magnetic field. Thus, in the classical description the Hall voltage is linearly proportional to the applied magnetic field, and the longitudinal magnetoresistivity ρ_{xx} is independent of the magnetic field.

In 1980 Klaus von Klitzing carried out an experiment on the Hall effect [8] and found deviations from the classical expectations. First of all, there are plateaus in the Hall voltage, which correspond to quantised values of $\rho_{xy} = h/\nu e^2$, where $\nu = 1, 2, 3, ...$ Second, when ρ_{xy} shows a plateau, ρ_{xx} goes to zero, whereas according to the classical picture ρ_{xx} is finite and constant, equation (2.7).

Consider a 2D gas of N_e non-interacting electrons at zero magnetic field. The Hamiltonian of such a system is

$$H = \sum_{i=1}^{N_e} \frac{\vec{p_i}^{\,2}}{2m} \quad . \tag{2.8}$$

The density of states (DOS) is $m/\pi\hbar^2$ (per spin/valley, see Chapter 1) and does not depend on energy.

In the presence of the magnetic field

$$H = \sum_{i=1}^{N_e} \frac{\left(\vec{p_i} + e\vec{A}(\vec{r_i})\right)^2}{2m} \ , \tag{2.9}$$

where $\vec{A}(\vec{r_i})$ is the magnetic vector potential, $\vec{B} = \nabla \times \vec{A}$. In order to solve the Schrödinger equation we take the Landau gauge $\vec{A} = (0, Bx, 0)$ and the single particle Hamiltonian takes the form:

$$H = \frac{p_x^2 + p_y^2 + 2p_y eBx + e^2B^2x^2}{2m} = \frac{p_x^2 + (p_y + eBx)^2}{2m} \ . \tag{2.10}$$

Then the Schrödinger equation is

$$\left[\frac{p_x^2}{2m} + \frac{1}{2m}\left(\hbar k + eBx\right)^2\right]\Psi(x) = E\Psi(x) \ . \tag{2.11}$$

Introducing the magnetic length $l_B = \sqrt{\frac{\hbar}{eB}}$ and using the expression for the Larmor frequency (equation (2.1)), we can rewrite the previous equation in the following form:

$$\left[\frac{p_x^2}{2m} + \frac{m\omega_c^2}{2}\left(kl_B^2 + x\right)^2\right]\Psi(x) = E\Psi(x) \ . \tag{2.12}$$

The magnetic length l_B has a physical meaning of an area πl_B^2 that is threaded by half of the magnetic flux quantum: $2\pi l_B^2 B = \Phi_0 = \frac{h}{e}$.

From equation (2.12) we get the energy spectrum of electrons in the magnetic field:

$$E_N = \hbar\omega_c(N + \frac{1}{2}) \ , \tag{2.13}$$

where $N = 0, 1, 2, ...$ This is the case for a two-dimensional electron gas with a parabolic dispersion relation. We will see that the spectrum for graphene is quite different.

The energy levels (equation (2.13)) are called Landau levels (LLs), which are

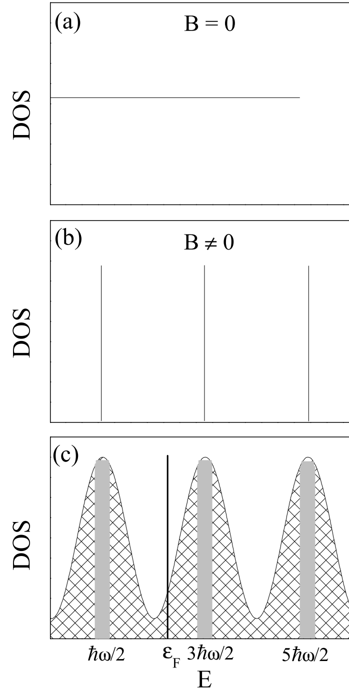

Figure 2.2: (a) The density of states in a conventional (with a parabolic dispersion relation) two-dimensional system at zero magnetic field. (b) For a non-zero magnetic field the DOS in an ideal 2D system is a series of δ - functions separated by $\hbar\omega/2$. (c) Same as in (b) but in the presence of disorder that broadens the peaks in the DOS. The hatched area corresponds to the localised states and the gray area to the extended states. The solid vertical line is a position of the Fermi level ε_F.

$\vec{k}$-independent. The magnetic field transforms the constant density of states of a 2D electron gas into a series of δ - functions separated by $\hbar\omega_c$ (see equation (2.13) and Fig. 2.2(a,b)).

For a sample of area S the number of states in each LL is

$$N_\Phi = \frac{S}{2\pi l_B^2} = \frac{eBS}{2\pi\hbar} \ . \tag{2.14}$$

The factor '2' in equation (2.14) takes into account the fact that at high magnetic fields each LL is split into two. Each of the two LLs has half the number of electrons than without splitting. The filling factor ν – the number of filled LLs – is equal to the total number of electrons, N_e, divided by the number of states in one LL, N_Φ:

$$\nu = \frac{N_e}{N_\Phi} = \frac{2N_e\pi\hbar}{eBS} = \frac{\Phi_0}{B}\frac{N_e}{S} = \frac{n\Phi_0}{B} \ . \tag{2.15}$$

For the integer quantum Hall effect (QHE) the filling factor is an integer.

In a perfect system at high magnetic fields, the density of states is a series of δ - functions located at energies $E_n = \hbar\omega_c(N + \frac{1}{2})$, which have the N_Φ - fold degeneracy. However, real samples have imperfections in their crystal lattice or impurities. This disorder lifts the degeneracy of the LLs and broadens them transforming them into bands with a width inversely proportional to the mean scattering time, Fig. 2.2(c). Two types of states appear: localised and extended. There is no current through the localised states. Suppose the magnetic field is fixed and the Fermi level is tuned. If the Fermi level lies in the area of localised states, then only the states below the Fermi level contribute to the resistivity. In other words ν filled Landau levels give rise to $\rho_{xy} = h/\nu e^2$ and plateaus appear in the transverse (Hall) resistivity. At the same time $\rho_{xx} = 0$. If the Fermi level lies within the band of the extended states, the carrier density in these states changes from 0 to N_Φ when ε_F passes through the extended states. This situation corresponds to a transition region between the plateaus in ρ_{xy}. The longitudinal resistivity is finite in this case.

Similarly to the resistivity tensor $\hat{\rho}$ (equations (2.7)) one can define the conductivity tensor $j_\alpha = \sigma_{\alpha\beta}E_\beta$. Using equations (2.6) we get:

$$\hat{\sigma} = \hat{\rho}^{-1} = \frac{1}{\rho_{xx}^2 + \rho_{xy}^2} \begin{pmatrix} \rho_{xx} & \rho_{xy} \\ -\rho_{xy} & \rho_{xx} \end{pmatrix} \tag{2.16}$$

In the quantum Hall effect regime when $\rho_{xy} = h/\nu e^2$ and $\rho_{xx} = 0$, the transverse conductivity equals $\sigma_{xy} = 1/\rho_{xy} = e^2\nu/h$, which follows from equation (2.16).

The QHE in graphene is quite different due to its unique electronic properties. The quantised energy levels at non-zero magnetic field are no longer determined by equation (2.13), but are given by [9,10]

$$E_N = \pm\nu_F\sqrt{2e\hbar BN}\ , \tag{2.17}$$

where $+/-$ refers to electrons/holes.

The quantised Hall conductivity in conventional 2D systems (with parabolic dispersion relation) is $\sigma_{xy} = 4e^2/h\ \nu$, where the factor 4 comes from the double valley and double spin degeneracy, whereas in graphene $\sigma_{xy} = 4e^2/h\ (\nu+1/2)$ [9,10].

Equation (2.17) shows that in graphene there is a level at zero energy, whereas in 2D systems with parabolic dispersion relation this level is absent.

2.2 Shubnikov-de Haas effect

When the magnetic field is not large enough ($\omega_c\tau < 1$) for the Hall plateaus to develop, the longitudinal resistivity experiences oscillations as a function of the magnetic field or the Fermi energy. These oscillations are called Shubnikov-de Haas oscillations (SdH). In the presence of a magnetic field the density of states is a series of localised and extended states, Fig. 2.2(c). Since the field is not very high, the energy levels are close to each other and overlap, equation (2.13). If B is fixed and the Fermi energy is tuned, then as ε_F passes through the peaks in the DOS, the resistivity is maximal. When ε_F passes through the dips in the DOS, the resistivity is minimal. The situation is similar when the Fermi energy is fixed and B is tuned. In this case the distance between two adjacent LLs, $\Delta E_N = E_{N+1} - E_N = \hbar\omega_c = \hbar eB/m$ (see equation (2.13)), increases when the magnetic field increases.

The SdH effect is a good tool to determine the carrier density in a system. In the case of graphene, suppose a magnetic field B_1 is applied and the Nth LL coincides with the Fermi energy: $E_N = \nu_F\sqrt{2e\hbar B_1 N} = \varepsilon_F$. Keeping the Fermi level fixed let us decrease the magnetic field to B_2, so that the (N+1)$^{\text{th}}$ LL coincides with ε_F. We get the system of equations:

$$\begin{cases} \nu_F\sqrt{2e\hbar B_1 N} = \hbar k_F \nu_F \\ \nu_F\sqrt{2e\hbar B_2 (N+1)} = \hbar k_F \nu_F \end{cases} . \tag{2.18}$$

We extract N from the first equation and $(N+1)$ from the second one:

$$\begin{cases} N = \frac{\hbar k_F^2}{2eB_1} \\ N+1 = \frac{\hbar k_F^2}{2eB_2} \end{cases} . \tag{2.19}$$

Subtracting the first equation from the second one we get:

$$1 = \frac{\hbar\pi n}{2e}\left(\frac{1}{B_2} - \frac{1}{B_1}\right) . \tag{2.20}$$

The carrier density is

$$n = \frac{4e}{h}\frac{1}{\left(\frac{1}{B_2} - \frac{1}{B_1}\right)} . \tag{2.21}$$

Thus, in order to determine the carrier density in graphene, one has to measure the longitudinal magnetoresistivity, determine the magnetic fields that correspond to any two adjacent LL's and use equation (2.21) to calculate the carrier density.

2.3 Weak localisation of charge carriers

Consider a classical electron (a particle) that travels from point A to point B and scatters off different scattering centres, Fig. 2.3(a). There are many paths along which the electron can travel, and we consider two of them for simplicity. The probability, P, for the electron to get to point B will be the sum of the squared probability amplitudes along each path: $P = |A_1|^2 + |A_2|^2$.

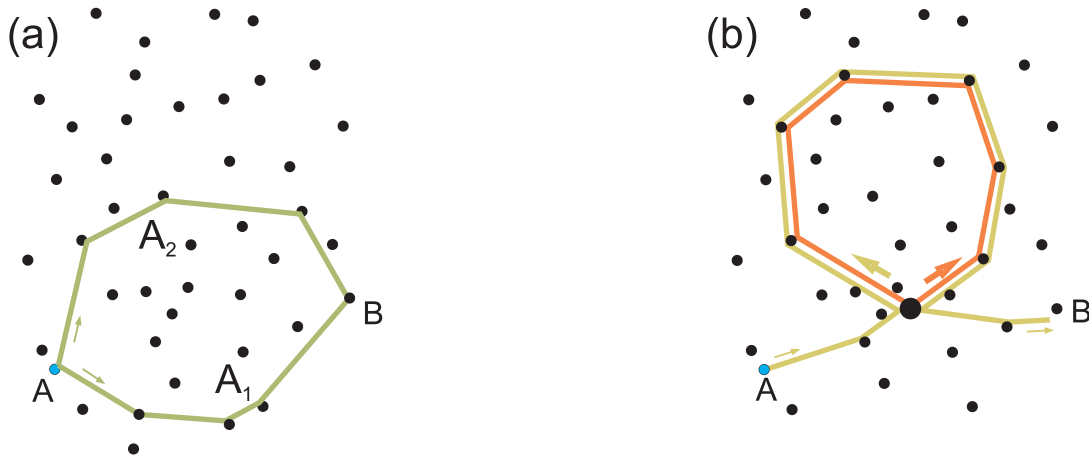

Figure 2.3: Various paths, (a) and (b), for an electron (blue circle) to go from point A to point B. Probability amplitudes along each path are A_1 and A_2. Black circles correspond to scattering centres.

In quantum mechanics electrons are treated as waves. In this case the two waves of the electron can travel in opposite directions along a closed loop and interfere at the point of intercept. Depending on the phase difference of the two waves the interference can be either constructive or destructive. If they meet in phase, then constructive interference takes place, increasing the probability to find the electron at the point of intercept: $P = |A_1|^2 + |A_2|^2 + 2|A_1||A_2|$. The total conductivity decreases and the electron becomes *weakly localised* [11, 12].

If the two waves meet in anti-phase, they interfere destructively. The probability for the electron to appear at the point of intercept decreases: $P = |A_1|^2 + |A_2|^2 -$

$2|A_1||A_2|$, and the total conductivity increases. This phenomenon is called *weak antilocalisation*.

In conventional two-dimensional systems (with parabolic dispersion relation) the two paths are identical, and the two waves meet in phase. Therefore, weak localisation (WL) of electrons is expected. In graphene due to the Berry phase of π the two waves meet in anti-phase and weak antilocalisation (WAL) is expected [13]. This is unusual, because in conventional 2D-systems WAL is possible only in the presence of strong spin-orbit interaction [11, 14–17], and in graphene WAL takes place even without it.

When we talk about WL, electron backscattering is important, i.e. when the momentum of an electron rotates by π after it has traveled along a closed loop. In this case the phase of one electron wave changes by $\pi/2$ (it changes by π when the electron momentum rotates by 2π - Berry phase, see equation (1.36)). The phase of the other wave changes by $-\pi/2$. They meet with a phase difference of $\pi/2 - (-\pi/2) = \pi$ and interfere destructively. Thus, weak antilocalisation takes place.

Another way to understand why quantum interference of electrons waves leads to antilocalisation is to calculate the probability of backscattering. The initial (immediately before entering the closed loop) and the final (after backscattering) states of the electron are

$$|i\rangle \propto \begin{pmatrix} e^{-i\varphi/2} \\ e^{i\varphi/2} \end{pmatrix} \qquad |f\rangle \propto \begin{pmatrix} -e^{-i\varphi/2} \\ e^{i\varphi/2} \end{pmatrix} . \tag{2.22}$$

The initial state, $|i\rangle$, is the electron wave function, equation (1.35). The final state, $|f\rangle$, is its wave function after $\varphi \rightarrow \varphi + \pi$. The probability of backscattering is therefore

$$\langle i|f\rangle = \begin{pmatrix} e^{i\varphi/2} & e^{-i\varphi/2} \end{pmatrix} \begin{pmatrix} -e^{-i\varphi/2} \\ e^{i\varphi/2} \end{pmatrix} = -1 + 1 = 0 . \tag{2.23}$$

As we discussed before, destructive interference decreases the probability to find the electron at the point of intercept. Thus, the calculated zero probability means

weak antilocalisation.

In experiment, weak localisation can be detected by applying a low magnetic field perpendicular to the current. In this case the amplitudes of the probability to pass the closed loop clockwise and counterclockwise acquire an additional phase factor:

$$A_1 \to A_1 \exp\left(i\frac{e}{\hbar}\oint \vec{A}d\vec{l}\right) = A_1 \exp\left(\frac{ieBS}{\hbar}\right) = A_1 \exp\left(\frac{i\pi BS}{\Phi_0}\right) , \qquad (2.24)$$

$$A_2 \to A_2 \exp\left(-\frac{i\pi BS}{\Phi_0}\right) , \qquad (2.25)$$

where $\vec{A}$ is the magnetic vector potential, $d\vec{l}$ is an infinitesimal vector element of the closed loop, $\Phi = \oint \vec{A}d\vec{l} = BS$ is the magnetic flux, S is the area of the closed loop and $\Phi_0 = h/2e$ is the quantum of magnetic flux. Thus, a magnetic flux threading the closed trajectories adds a phase difference to the two electron waves

$$\Delta\varphi = 2\pi\frac{\Phi}{\Phi_0} \qquad (2.26)$$

and destroys the interference.

When the two electron waves meet in phase, they interfere constructively, and the total conductivity decreases (WL). The magnetic field decreases the probability for the electron to stay at the point of intercept, and increases the total conductivity leading to positive magnetoconductivity (MC): $\Delta\sigma(B) = \sigma(B) - \sigma(B = 0) > 0$. When the two electron waves meet in anti-phase, they interfere destructively, and the total conductivity increases due to WAL. The magnetic field decreases the conductivity and leads to negative MC, $\Delta\sigma(B) < 0$.

Thus, in experiment the conductivity is measured as a function of low magnetic field. The sign of the MC allows one to determine the behavior of an electron system: WL or WAL.

The situations described above take place in 'clean' samples. However, in real ones there are different kinds of imperfections, which affect quantum interference of electron waves. Unlike conventional 2D systems, WL in graphene is sensitive not only to inelastic scattering, but also to elastic scattering mechanisms [13, 18].

Electrons lose their energy during inelastic collisions, which also break their phase coherence. Such processes are characterised by the dephasing time τ_φ. Elastic (energy conserving) scattering can be of two types due to the presence of the two valleys. Processes that scatter electrons within one valley require a smooth scattering potential, which can be produced by, for example, ripples or dislocations [13, 19, 20]. Such processes are characterised by the scattering time τ_s. Since the chirality suppresses backscattering within one valley (see e.g. equation (2.23)), such scattering suppresses WL. Weak localisation can also be destroyed by so called trigonal 'warping', characterised by the time τ_w. Trigonal warping appears when next-nearest-neighbor carbon atoms are taken into account ($\gamma_0' \neq 0$) to calculate the energy spectrum of electrons in graphene. In this case the Fermi surface is no longer circular, but triangular in shape. Therefore, when an electron is backscattered within one valley, then $\vec{k} \to -\vec{k}$, but there is no such k-state due to the distortion of the Fermi surface. This leads to the loss of coherence and destruction of interference. The combined effect of the described processes is characterised by the intra-valley scattering time τ_*: $\tau_*^{-1} = \tau_s^{-1} + \tau_w^{-1}$.

Atomically sharp defects, such as edges of samples or missing carbon atoms, can scatter electrons between the valleys. Such scattering processes are characterised by the inter-valley scattering time τ_i. They break the chirality and allow the interference of electron waves. Thus, inter-valley scattering restores WL.

Electron waves traveling along a closed loop scatter (elastically or inelastically) off impurities. These impurities can break the phase of the waves. Therefore, the size of the closed loop can not exceed a certain length in order for the waves to stay coherent and interfere. This length is called the electron dephasing length, $L_\varphi = \sqrt{D\tau_\varphi}$, where D is the diffusion coefficient, and is a very important quantity in the WL effect. The dephasing length limits the size of the closed trajectories. This characteristic length decreases if the temperature increases [21, 22]. When the closed loops become smaller the strength of WL is reduced. Therefore, quantum interference is usually observed at low temperatures (less than ~ 50 K) [23–33].

The theory [13] predicts the following MC in graphene:

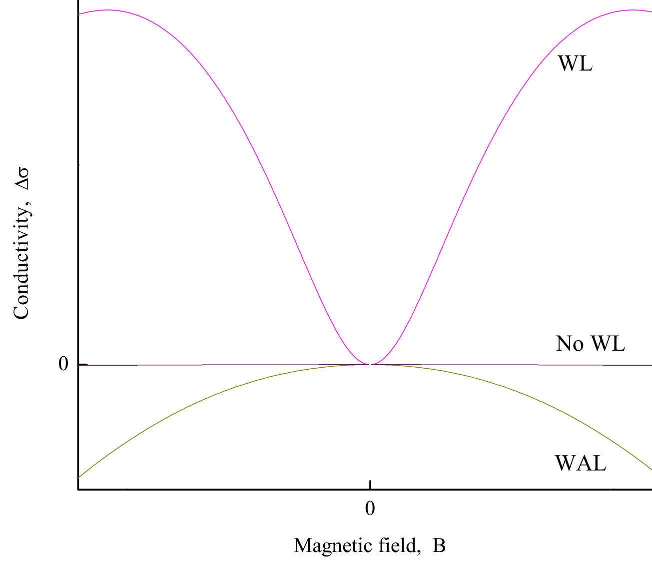

Figure 2.4: Limiting cases to observe WL or WAL in graphene. The upper curve corresponds to WL and the situation when $\tau_*^{-1} \gg \tau_\varphi^{-1} \sim \tau_i^{-1}$. The bottom curve is the case of a clean sample (no intra- or inter-valley scattering), $\tau_\varphi^{-1} \gg \tau_i^{-1}, \tau_*^{-1}$. Under certain conditions no weak localisation can be observed (middle curve): $\tau_*^{-1} \gg \tau_\varphi^{-1} \gg \tau_i^{-1}$.

.

$$\Delta\sigma(B) = \frac{e^2}{\pi h} \cdot \left(F\left(\frac{\tau_B^{-1}}{\tau_\varphi^{-1}}\right) - F\left(\frac{\tau_B^{-1}}{\tau_\varphi^{-1} + 2\tau_i^{-1}}\right) - 2F\left(\frac{\tau_B^{-1}}{\tau_\varphi^{-1} + \tau_i^{-1} + \tau_*^{-1}}\right)\right) . \quad (2.27)$$

Here $F(z) = \ln z + \psi(0.5 + z^{-1})$ is a monotonically increasing function, $\psi(x)$ is the digamma function, $\tau_B^{-1} = 4eDB/\hbar$ and $D = \nu_F l_p/2$, l_p is the mean free path. (The theory assumes that the momentum relaxation rate τ_p^{-1} is the highest in the system and comes from charged impurities, and does not affect the electron interference.) Negative MC corresponding to antilocalisation is described by the second and third (negative) terms. In the absence of intra- and inter-valley scattering, $\tau_{i,*} \to \infty$, $\Delta\sigma(B)$ is totally determined by the third term – this situation would correspond to defect-free graphene samples (clean samples), Fig. 2.4. In the opposite case of strong intra- and inter-valley scattering (small τ_* and τ_i), the negative terms are suppressed and the first (positive) term dominates, which corresponds to electron localisation. It is this situation that was realised in recent experiments [34, 35] on

mechanically exfoliated graphene where the negative terms, originating from the chirality of electrons, were not large enough to change the sign of the low-field MC.

Analysis of equation (2.27) shows that in order to observe WAL, it is not necessarily to have a clean sample. Indeed, using the fact that the function $F(z)$ is quadratic at small $z \ll 1$, $F(z) = z^2/24$, we can simplify equation (2.27):

$$\Delta\sigma(B) = \frac{e^2}{24\pi h} \cdot \left(\frac{4eDB\tau_\phi}{\hbar}\right)^2 \left(1 - \frac{1}{(1+2\tau_\phi/\tau_i)^2} - \frac{2}{(1+\tau_\phi/\tau_i+\tau_\phi/\tau_*)^2}\right) . \quad (2.28)$$

The expression in brackets determines the sign of the MC. Figure 2.5 shows the diagram, in which a curve $\Delta\sigma(B) = 0$ separates regimes of positive MC (above the curve) and negative MC (below the curve). The points on the curve correspond to the absence of the quantum correction. Along the X- and Y-axis the ratios τ_φ/τ_i and τ_φ/τ_*, respectively, are plotted. A condition τ_φ/τ_*, $\tau_\varphi/\tau_i \ll 1$ corresponds to the case of a clean system (no inter- and intra-valley scattering). As we already discussed, WAL is expected (see the origin of Fig. 2.5). In the opposite case, τ_φ/τ_*, $\tau_\varphi/\tau_i \gg 1$, electrons are elastically scattered within a valley and between the valleys many times before they loose their phase coherence (strong inter- and intra-valley scattering).

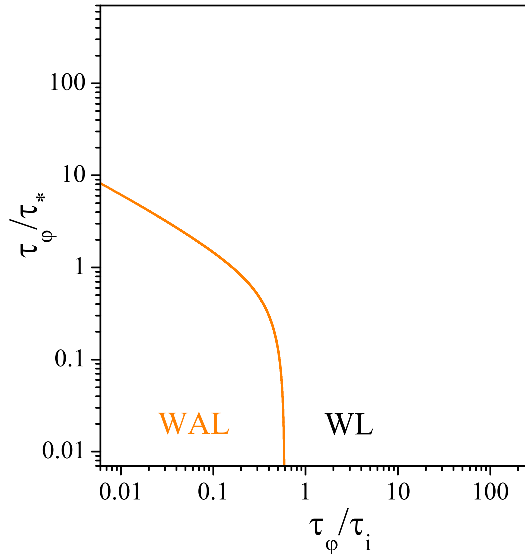

Figure 2.5: Conditions to observe WL and WAL in graphene. Orange curve corresponds to $\Delta\sigma(B) = 0$ in equation (2.28). The ratios of τ_φ/τ_* and τ_φ/τ_i, for which $\Delta\sigma(B) > 0$ (area above the curve), indicate WL. In the opposite case (area below the curve) they indicate WAL.

.

As one can see from the diagram, WAL can be observed when intra- and inter-valley scattering are present in the system. The numbers of the ratios when WAL is expected in real samples say that elastic scattering can be stronger or at least comparable to inelastic scattering. The ratios can be tuned by varying the temperature and carrier density. In Chapters 4 and 5 we discuss the consequences of such tuning.

Interference of electron waves leads to another quantum phenomenon, universal conductance fluctuations (UCF) [36–39], which will also be present in the experiments described in this work. Electrons moving along many different trajectories in a sample will experience interference. The probability of an electron to traverse the sample within a certain time will therefore contain an interference term, which depends on the phase difference of the electron waves (as was discussed earlier). If this term fluctuates under changing surrounding conditions, then the probability, and therefore the conductance, will also fluctuate. One such 'condition' is a change of the impurity configuration. For example, let us consider many macroscopically identical samples, which differ only in their arrangement of impurities. The conductance averaged over these samples is $\langle G \rangle = G_0$. But due to different configuration of impurities, the conductance $G = G_0 + \delta G$ in each of the samples will be slightly different (will fluctuate from sample to sample). The amplitude of the conductance fluctuations is universal and of the order of $\delta G = e^2/h$. It has been shown [36, 37] that instead of taking many samples, one can take a single sample and measure the conductance as a function of magnetic field or the Fermi energy, which will be equivalent to changing the impurity configuration. The fluctuations are reproducible and aperiodic and seen in small samples, whose length is comparable to the dephasing length, and at low temperatures.

Since in this work we study magnetoconductivity and the dependence of the conductivity on the Fermi energy, the UCF should be suppressed by averaging the conductance values over the magnetic field or the Fermi energy for other quantum effects to be investigated.

2.4 Electron-electron interaction in the presence of disorder

In the previous section we considered a single-particle effect: an electron interferes with itself and becomes weakly localised. Interference is also possible when many electrons interact in the presence of disorder. The interaction occurs via the Coulomb potential and gives rise to another quantum effect - electron-electron interaction correction (EEI) to the conductivity [40].

Consider a gas of non-interacting electrons with a single charged impurity. Interaction of the electrons with the impurity leads to oscillations of the charge density around it, which are called the Friedel oscillations [41]:

$$\delta n(\vec{r}) \propto \frac{\sin(2\vec{k}_F\vec{r})}{r^2} , \tag{2.29}$$

where $\vec{r}$ is the distance from the impurity, and $\vec{k}_F$ is the Fermi wave vector,

If we turn on the interaction between the electrons, this will create the oscillating scattering potential, which can be represented as a Hartree term [42, 43]:

$$V_H(\vec{r}) = \int d\vec{r'} V(\vec{r} - \vec{r'})\delta n(\vec{r'}) , \tag{2.30}$$

where $V(\vec{r} - \vec{r'}) = e^2/|\vec{r} - \vec{r'}|$ is the Coulomb potential, and $n(\vec{r'})$ is the electron density. Electron waves scattering off the impurity itself and the oscillating potential (Friedel oscillations) interfere with each other. The interference is most important when the electron waves are backscattered. Suppose one electron wave follows path A, the other one follows path B (Fig. 2.6). On B the wave acquires an additional phase due to the difference in distances of A and B. The wave vector changes by $2\vec{k_F}$ (due to electron backscattering), and an additional distance is $\vec{R}$ - the radiusf of the Friedel oscillation. Therefore, the phase difference is $2\vec{k_F}\vec{R}$. This phase is canceled by the phase of the Friedel oscillation $-2\vec{k_F}\vec{R}$ (equation (2.29)) leading to the constructive interference and a decrease of the conductivity.

This picture of the EEI correction is valid in the ballistic regime, i.e. when $k_BT\tau_p/\hbar > 1$, which means the time of electron interaction $\hbar/k_BT$ is smaller than

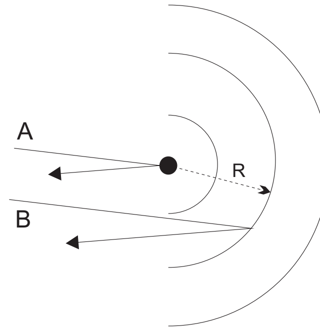

Figure 2.6: Nature of the electron-electron interaction correction. Electron waves following paths A and B scatter off an impurity (black ball) and the Friedel oscillations (semicircles) and interfere constructively.

.

the momentum relaxation time τ_p. In the diffusive regime, $k_B T \tau_p/\hbar < 1$, when two interacting electrons experience many collisions with impurities during the time of their interaction, the picture is slightly different. In this case there are many impurities and interference takes place not only when electron waves are backscattered, but also when they are scattered by any angle [43]. The origin of the EEI correction is the same as in the ballistic regime: electron waves are scattered off impurities and Friedel oscillations and interfere with each other.

Note that for the EEI correction to exist, two conditions must be fulfilled: the presence of at least one impurity to create the Friedel oscillations, and Coulomb interaction to transform the oscillations of charge density into oscillations of the scattering potential. The Friedel oscillations can be created by non-interacting electrons, but it is the Coulomb interaction that creates the oscillations of the scattering potential. This potential is then scattered off by electrons waves.

The theory [40] predicts the following expression for the EEI correction in the diffusive regime:

$$\delta\sigma^{\mathrm{EEI}}(T) = -A(F_0^\sigma)\frac{e^2}{2\pi^2\hbar}\ln\frac{\hbar}{k_B T \tau_p} \ , \tag{2.31}$$

where $A(F_0^\sigma)$ is the coefficient that depends on the Fermi-liquid constant F_0^σ. The Fermi-liquid constant is a function of the so-called r_s parameter, which shows the

strength of EEI:

$$r_s = \frac{U_C}{E_F} \ , \tag{2.32}$$

where U_C and E_F are the Coulomb and Fermi energies, respectively.

Investigation of the EEI correction to the conductivity can give information about the Fermi-liquid constant F_0^σ. In non-chiral systems, F_0^σ is given by the interaction potential averaged over all possible scattered momenta [40, 43]:

$$F_{norm} = -\nu \langle U(|\vec{p} - \vec{p'}|) \rangle = -\nu \int \frac{d\theta}{\pi} U \left(2k_F \sin\frac{\theta}{2} \right) \ , \tag{2.33}$$

where ν is density of states per spin/valley component, $U(q)$ is the Fourier component of the interaction, θ is the scattering angle, and k_F is the Fermi wave vector. In chiral systems (e.g. graphene) chirality conservation suppresses the scattering amplitude [44] by the factor $\cos(\theta/2)$, and therefore one has to use a slightly different expression:

$$F_{chiral} = -\nu \int \frac{d\theta}{\pi} U \left(2k_F \sin\frac{\theta}{2} \right) \cos^2\frac{\theta}{2} \ . \tag{2.34}$$

For a simple estimate of the Fermi-liquid constant, we use [45] the Thomas-Fermi approximation writing the Fourier image of the screened 2D Coulomb potential in the form

$$U(q) = \frac{2\pi e_*^2}{q + \kappa} \ , \tag{2.35}$$

where e_* is the effective charge, $e_*^2 = 2e^2/(\epsilon + 1)$, that includes the suppression of the Coulomb potential by the SiO_2 substrate, $\epsilon = 3.9$, $\kappa = N \cdot 2\pi\nu e_*^2$ is the screening parameter, N is the total number of spin/valley channels per electron (this factor is due to the Thomas-Fermi screening which is provided by all possible channels). Therefore,

$$U(q) = \frac{2\pi e_*^2}{q + 2\pi e_*^2 N\nu} \ , \tag{2.36}$$

Then, the Fermi-liquid constant can be expressed in terms of r_s, which for graphene is equal to $r_s = U_C/E_F = e_*^2/(r\hbar\nu_F k_F) = e_*^2/(\hbar\nu_F)$ with $r = 1/\sqrt{\pi n}$ being the distance between two interacting electrons, and N. Thus, we find [45] for a non-chiral 2D electron gas (2DEG)

$$F_{norm} = -\frac{r_s}{2}\Phi\left(\frac{Nr_s}{2}\right) \ , \tag{2.37}$$

where the function $\Phi(a)$ is

$$\Phi(a) = \int_0^\pi \frac{d\theta}{\pi}\frac{1}{\sin\frac{\theta}{2}+a} = \begin{cases} \frac{1}{\pi\sqrt{1-a^2}}\ln\frac{1+\sqrt{1-a^2}}{1-\sqrt{1-a^2}} & a<1 \\ \frac{2}{\pi\sqrt{1-a^2}}\arctan\sqrt{a^2-1} & a>1 \end{cases} \ . \tag{2.38}$$

For $r_s = 0.88$ and $N = 2$ (as in GaAs), this gives $F_0^\sigma = -0.18$.

For a chiral 2DEG, one can relate the integral to the same function Φ, thus finding

$$F_{chiral} = -\frac{r_s}{2}\Phi_c\left(\frac{Nr_s}{2}\right) \ , \tag{2.39}$$

with

$$\Phi_c(a) = (1-a^2)\Phi(a) + a - \frac{2}{\pi} \ . \tag{2.40}$$

For $r_s = 0.88$ and $N = 4$ (graphene), this gives $F_0^\sigma = -0.10$.

Thus, the theory predicts F_0^σ to be the smallest in graphene among all other systems due to the chirality of charge carriers. The approximation (2.40) which neglects effects of strong interaction, such as the Fermi velocity and Z-factor renormalisations [46], is expected to be valid for $r_s \leq 1$, which is the case for graphene.

Note that due to the linear dispersion relation, $E_F = \hbar k_F \nu_F$, in graphene, r_s does not depend on the carrier density. For comparison, in conventional 2D systems it does depend on the carrier density as $1/\sqrt{n}$ (see e.g. [47]). Therefore, in graphene the EEI correction in the diffusive regime is independent of the carrier density.

In Chapters 4 and 5 we compare this theory with experiment.

2.5 Methods of separation of the quantum corrections

Both WL and EEI corrections to the conductivity depend logarithmically on temperature [11,40]. Therefore, in order to study them, it is necessary to separate their contributions. In this section we discuss in detail the methods for separating the two quantum corrections.

From the previous section we know that the EEI correction depends logarithmically on temperature, equation (2.31). To find the temperature dependence of the WL correction at zero magnetic field, we use the definition of WL: a 2D system is in the weak localisation regime if at infinitely large magnetic field $B \to \infty$, MC is positive $\Delta\sigma(B) > 0$. This means that $\Delta\sigma(B) = \delta\sigma(B \to \infty) - \delta\sigma(B = 0) = -\delta\sigma(B = 0) \equiv -\delta\sigma^{WL}(T)$. The WL correction $\delta\sigma(B \to \infty) = 0$, because at large magnetic field electron interference is suppressed, equation (2.26). Using equation (2.27) and the fact that $F(z) = \ln z$ at large $z \gg 1$, we arrive at the WL correction to the conductivity at zero magnetic field [13]:

$$\delta\sigma^{\mathrm{WL}}(T) = -\frac{e^2}{2\pi^2\hbar}\left[\ln\left(1 + 2\tau_\varphi(T)/\tau_i\right) - 2\ln\left(\frac{\tau_\varphi(T)/\tau_p}{1 + \tau_\varphi(T)/\tau_i + \tau_\varphi(T)/\tau_*}\right)\right] \quad (2.41)$$

As clearly seen from equations (2.41) and (2.31) both corrections are logarithmically dependent on temperature. Therefore, in experiment it is difficult to distinguish between the two. There are several methods of separation of the WL and EEI corrections.

1) Using the standard theoretical model, equation (2.27) and [13], the three characteristic times are determined from the low-field MC studies: the dephasing time τ_φ, the elastic times of inter-valley scattering τ_i and intra-valley scattering τ_*. These times are used to determine the WL correction at zero magnetic field, equation (2.41), which is then subtracted from the experimental temperature dependence of the conductivity.

2) The EEI correction can be isolated by applying a perpendicular magnetic field: a magnetic flux adds a phase difference to the two electron waves and destroys interference (equation (2.26)). The suppression of WL is expected at magnetic fields,

which are much larger than the so-called 'transport' field [48–50], $B_{tr} = \hbar/2el_p^2$, where l_p is the mean free path. At the same time these magnetic fields should be small in order not to affect the EEI correction due to the Zeeman effect [11]. The effect is expected at higher fields that satisfy the following condition: $g^*\mu_B B > k_B T$, where $g*$ is the Landé g-factor, which in graphene is 2 (see e.g. [51]), and μ_B is the Bohr magneton.

3) The correction due to electron-electron interaction can be determined directly from the Hall coefficient studies [40]. In this case the transverse magnetoresistivity $\rho_{xy}(B)$ is measured in the Hall regime to determine the Hall coefficient R_H:

$$R_H = \frac{\rho_{xy}}{B} \ . \tag{2.42}$$

The advantage of this method is that WL does not contribute to the transverse resistivity, i.e. $\delta\rho_{xy}^{WL} = 0$. But it does to the longitudinal, σ_{xx}, and transverse, σ_{xy}, conductivities. The EEI correction enters only σ_{xx}:

$$\begin{cases} \sigma_{xx} = \sigma_0 + \delta\sigma^{WL} + \delta\sigma^{EEI} \\ \sigma_{xy} = \sigma_0 \mu B + \delta\sigma^{WL} \end{cases} \tag{2.43}$$

where

$$\sigma_0 = \frac{en\mu}{1 + (\mu B)^2} \tag{2.44}$$

is the Drude conductivity, μ is the mobility of electrons, n is the electron density, e is the absolute value of the electron charge.

Converting the conductivities, equations (2.43), into the resistivities using the following relations:

$$\rho_{xx} = \frac{\sigma_{xx}}{\sigma_{xx}^2 + \sigma_{xy}^2} \qquad \rho_{xy} = \frac{\sigma_{xy}}{\sigma_{xx}^2 + \sigma_{xy}^2} \tag{2.45}$$

and expressing the Hall coefficient as $R_H = R_H^0 + \delta R_H$, where R_H^0 is the classical Hall coefficient and δR_H is the correction to R_H^0, we arrive at the following expression

for δR_H:

$$\frac{\delta R_H(T)}{R_H^0} = -\frac{2\delta\sigma^{EEI}(T)}{\sigma_0} \tag{2.46}$$

and

$$\rho_{xx} = \frac{1}{\sigma_0} - \frac{\delta\sigma^{EEI}}{\sigma_0^2}\left(1 - (\mu B)^2\right) \ . \tag{2.47}$$

Equation (2.46) shows that the study of the Hall coefficient gives the magnitude of the EEI correction directly. There is no need to consider the WL correction in this method. Equation (2.47) gives the values of the Drude conductivity, σ_0, at $B = 1/\mu$. The classical Hall coefficient is $R_H^0 = 1/ne$. The carrier density n can be determined from the Shubnikov-de Haas oscillations (as was discussed in Chapter 1).

Realisation of methods 1 and 2 is given in Chapter 4 and realisation of method 3 in Chapter 5.

2.6 Electron-phonon interaction

There are several contributions to the temperature dependence of the conductivity. Depending on a studied temperature range some of the contributions can be neglected. At low temperatures the quantum corrections to the Drude conductivity dominate, and at high temperatures electron-phonon interaction is the main contribution to σ_0. At intermediate temperatures both the quantum corrections and electron-phonon interaction are important. At these temperatures in order to study the corrections, the phonon contribution has to be subtracted. In the following chapters we discuss each of these temperature ranges. For example, we determine the EEI correction at both low- and intermediate T and compare the results.

There are different types of phonons that can contribute to the resistivity of graphene on the SiO_2 substrate [52–56]: phonons coming from the substrate and those in a graphene sheet. The latter includes acoustic and optical phonons as well as flexural phonons. At temperatures below 100 K only acoustic phonons contribute to the resistivity [52, 53, 57], because optical phonons are difficult to excite at these

temperatures and the effect of flexural phonons is suppressed due to the presence of the substrate [55, 56]. The Boltzmann transport theory gives [45, 52, 53] the following expression for the electron-acoustic phonon contribution to the resistivity in graphene:

$$\rho_A(T) = \frac{1}{\pi}\frac{D_a^2 E_F^2}{\rho_s \upsilon_{ph} \hbar^3 \upsilon_F^3} \int_0^{\pi} \frac{T_{\rm BG}}{T} \cos^2\frac{\theta}{2} \sin^4\frac{\theta}{2} \times \sinh^{-2}\left(\frac{T_{\rm BG}}{T}\sin\frac{\theta}{2}\right) d\theta, \qquad (2.48)$$

where D_a is the deformation potential, $T_{\rm BG} = 2\upsilon_{ph}E_F/(\hbar k_B \upsilon_F)$ is the Bloch-Grüneisen temperature, θ is the scattering angle, $\rho_s = 7.6 \times 10^{-7}$ kg m^{-2} is the density of graphene, $\upsilon_{ph} = 2 \times 10^4$ m s^{-1} is the speed of sound, $\upsilon_F = 10^6$ m s^{-1} is the Fermi velocity of carriers and E_F is the Fermi energy. In the high-temperature limit, $T \gg T_{\rm BG}$, the phonon contribution to the resistivity is

$$\rho_A(T) = \left(\frac{h}{e^2}\right) \frac{\pi^2 D_a^2 k_B T}{2h^2 \rho_s \upsilon_{ph}^2 \upsilon_F^2} \ . \qquad (2.49)$$

At temperatures below the Bloch-Grüneisen temperature $\rho_A(T) \propto T^4$

For graphene it was found that $D_a = 18 \pm 1$ eV [57], 18 and 21 eV [58] for electron and holes, respectively, and 25 ± 5 eV [59].

At temperatures above 100 K optical phonons coming from the Si/SiO$_2$ substrate become important [54, 57], which give the following contribution to the resistivity:

$$\rho_{Op}(V_g, T) = 0.607\frac{h}{e^2} V_g^{-1.04} \left(\frac{1}{e^{(59meV)/k_B T} - 1} + \frac{6.5}{e^{(155meV)/k_B T} - 1}\right) \ . \qquad (2.50)$$

In order to analyse the experimental temperature dependence of the resistivity at high T, the phonon contribution is represented as a sum of two terms:

$$\rho_{e-ph} = \rho_A + \rho_{Op} \ , \qquad (2.51)$$

where the deformation potential D_a is the only fitting parameter.

2.7 Spin-orbit interaction

When an electron moves with relativistic velocity in an electric field, in the rest frame of the electron the electric field transforms into the magnetic field (Lorentz transformation):

$$\vec{B} = -\frac{[\vec{\nu} \times \vec{E}]}{c^2} \ , \tag{2.52}$$

where $\vec{\nu}$ is the velocity, $\vec{E}$ is the electric field the electrons travel through, c is the speed of light. Coupling of the electron motion to this field gives rise to spin-orbit interaction (SOI). The origin of the electric field can be different: the electric field from the atomic nuclei or that coming from the crystal or band structure of the solid. The electron spin can only interact with the magnetic field, which can be created by the spin-orbit interaction or by an external source.

Since our interest is quantum interference, it is important to understand the mechanisms of electron dephasing (for a review see [60]). These mechanisms will be discussed in details in Chapters 4 and 5. One of them can be the SOI. So far we have not considered the electron spin when we talked about interference of the two electron waves traveling along a closed loop. In fact, the phase difference of the waves depends on the spin. In case of strong SOI the spin of the electron that propagates along a closed trajectory rotates with respect to its original orientation. This will lead to the destructive interference of the two waves and weak antilocalisation of charge carriers [11, 14–17]. If the SOI is not that strong, it can only lead to the suppression of weak localisation.

In 2DEGs moving electrons interact with their surroundings, such as impurities, phonons, internal and external electric and magnetic fields. All of this can flip the electron spin and therefore lead to the dephasing of electron waves. Thus, electron spin and dephasing are linked. We will focus our investigation of SOI on the possible mechanisms of spin dephasing. In graphene two types of spin dephasing are relevant: Elliot-Yafet [61,62] (EY) and Dyakonov-Perel [63,64] (DP). In the EY mechanism the direction of the electron spin changes during scattering events that cause momentum relaxation, like electron scattering off impurities or phonons, Fig.

2.7(a). The Hamiltonian for electrons in this case is

$$H_{SO} = \frac{\hbar}{4m_0^2c^2}\vec{p}\cdot(\vec{\sigma}\times\vec{\nabla}V) \ , \tag{2.53}$$

where m_0 is the free electron mass, $\vec{p}$ is the momentum, V is the scalar electric potential and $\vec{\sigma} = (\sigma_x, \sigma_y, \sigma_z)$ is a vector, whose components are the Pauli matrices:

$$\sigma_x = \begin{pmatrix} 0 & 1 \\ 1 & 0 \end{pmatrix} \qquad \sigma_y = \begin{pmatrix} 0 & -i \\ i & 0 \end{pmatrix} \qquad \sigma_z = \begin{pmatrix} 1 & 0 \\ 0 & -1 \end{pmatrix} \ . \tag{2.54}$$

In the presence of the magnetic field, $\vec{B} = [\vec{\nabla}\times\vec{A}]$, the momentum $\vec{p}$ is replaced by $\vec{P} = \vec{p} + e\vec{A}$.

For the EY mechanism the time during which the electron keeps memory about the spin original orientation, spin coherence time, $\tau_{\rm SO}$, depends linearly on the mean free path, l_p. The characteristic spin coherence length $L_{\rm SO} = \sqrt{D\tau_{\rm SO}} \propto \sqrt{l_p l_p} \propto l_p$.

In the DP mechanism of spin dephasing the effective magnetic field produced by the SOI causes the spin to precess, Fig. 2.7(b). The magnetic field changes its direction during the electron scattering. For this mechanism the spin coherence time is inversely proportional to the mean free path $\tau_{\rm SO} \propto l_p^{-1}$. Therefore, $L_{\rm SO}$ is independent of l_p.

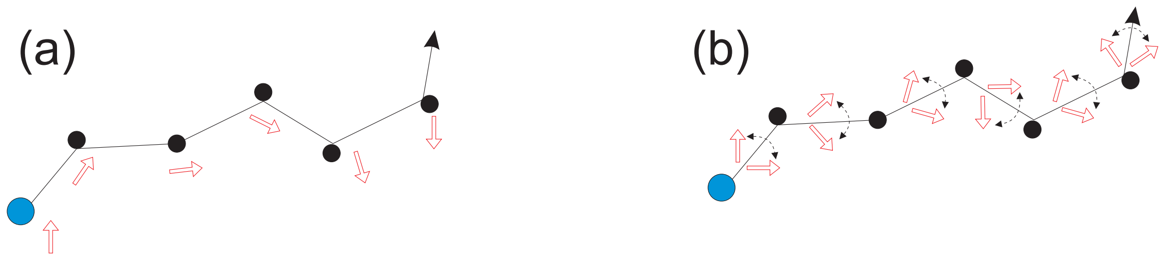

Figure 2.7: (a) Elliot-Yafet mechanism of spin dephasing: the direction of spin (red arrow) changes every time an electron (blue circle) scatters off impurities (black circles) or phonons. (b) Dyakonov-Perel mechanism: the SOI induces a magnetic field that changes its direction randomly during electron scattering

Different dependences of the spin coherence length on the mean free path for the two mechanisms allow one to distinguish between the EY or DP types of spin dephasing in the experiment.

2.8 Variable-range hopping

In very disordered systems electron states are localised [65]. This means that electrons wave functions are localised in a limited area and decay exponentially:

$$\Psi = f(r)e^{-r/\xi} \ , \tag{2.55}$$

where ξ is the localisation radius or localisation length. The limited area is roughly equal to the localisation radius.

Due to the presence of the exponential factor in equation (2.55) electron wave functions overlap, therefore there is a finite probability $1/\tau_{ij}$ for electrons to tunnel (hop) from one site to another [66]. The tunneling is possible by means of phonons:

$$\frac{1}{\tau_{ij}} \propto f(E_i)(1 - f(E_j))[1 + n(E_{ij})] \int |M(q)|^2 \delta(\hbar qs - E_{ij}) d^3q \ . \tag{2.56}$$

This equation means that an electron in the initial state i with the Fermi distribution

$$f(E_i) = \frac{1}{e^{\frac{E_i - \mu}{T}} + 1} \ ,$$

where μ is the chemical potential, tunnels to the final state j with the Fermi distribution $f(E_j)$. For the tunneling to take place the final state has to be empty. This fact is described by a factor $(1 - f(E_j))$. Hopping of electrons from one state i to the other j occurs via phonon assisted tunneling. This means that electrons emit or absorb phonons during hopping. The phonon distribution function is the Bose function

$$n(E_{ij}) = \frac{1}{e^{\frac{E_{ij}}{T}} - 1} \ ,$$

where E_{ij} is the difference in energies of the initial and final states $E_{ij} = E_i - E_j$. The δ - function is necessary to fulfil the energy conservation law: phonons are emitted or absorbed in order to compensate the energy difference E_{ij}. $M(q)$ and s are the electron-phonon coupling constant and the speed of sound, respectively.

In 2D systems the hopping length is $R_0 = (a/3)\,(T_0/T)^{1/3}$ and it increases with decreasing temperature [67]. Here $T_0 = \beta(\nu(\varepsilon_F)\xi^2)^{-1}$, $\nu(\varepsilon_F)$ is the density of states

at the Fermi level, β is a numerical factor. The conductivity obeys Mott's law

$$\sigma(T) = \sigma_0(T) e^{-\left(\frac{T_0}{T}\right)^{1/3}} , \tag{2.57}$$

where $\sigma_0(T)$ is a prefactor that depends on the electron-phonon coupling. At $T \ll T_0$ the exponent in equation (2.57) dominates. This is the variable-range hopping regime. In the opposite case, $T \gg T_0$, $\sigma_0(T)$ dominates, which gives a power law dependence.

In Chapter 6 we describe a way to produce strong disorder in graphene that will lead to the variable-range hopping conductivity.

2.9 Atomic force microscopy

Scanning probe microscopy (SPM) is a powerful method to study morphology and local properties of solids with high spatial resolution [68]. Investigation of the surfaces is carried out with the help of a probe with a tip at the end of the probe. The tips have a radius that varies from one atom to tens of nanometers. The probe is moving along the surface at a typical distance of 0.1 - 10 nm from the surface.

The principle of operation of scanning probe microscopes is based on different types of interaction between the tip and the surface. Therefore, there are different kinds of the microscopes, such as scanning tunneling (STM) or atomic force (AFM) microscopes. The operation of the STM [69] is based on the tunneling current between the tip and a conducting surface. The AFM operation [70] is based on the force interaction between the tip and a surface. In both types of SPM there is a parameter that characterises the interaction between the tip and the surface. It can be current (STM) or force (AFM). This parameter depends on the tip-surface distance and can be used to make a feedback system (FB). An operator sets the original value of the parameter, and the FB system keeps it fixed. If during scanning the tip-surface distance changes, then the parameter also changes. The FB system approaches or withdraws the tip from the surface until the value of the parameter becomes equal to its original value. The computer records the changes of the tip-sample distance as a function of the tip position and reconstructs a profile of the surface.

In this work a room temperature AFM was used to characterise graphene samples. The fabrication process of graphene (see the next chapter) does not allow to control the thickness of the samples. Therefore, once the sample is found, it is necessary to verify the number of layers. This can be done by scanning the surface of graphene and the underlying substrate by the AFM tip. As a result the height of the samples with respect to the substrate will be determined. The thickness of a single layer graphene is known to be 0.34 nm [2]. Thus, one can easily determine the number of layers [71].

2.10 Raman spectroscopy

When atoms and molecules are illuminated with light, photons are elastically scattered off them. This process is called Rayleigh scattering. Electrons absorb photons and get excited to a higher energy level. After relaxation the electrons return to their original state emitting photons.

However, photons can also scatter inelastically. In this case the energy of scattered photons is different compared to that of incident photons or in other words the frequency of light is shifted after scattering. This process is called Raman scattering [72]. There are two types of Raman scattering: Stokes and anti-Stokes. If the energy of emitted photons is smaller, than that of absorbed photons, then this corresponds to Stokes scattering. In the opposite case, when emitted photons are more energetic, then anti-Stokes scattering takes place.

Raman spectroscopy is a fast and non-destructive technique that uses the Raman scattering effect to study doping, defects, strain, edges, etc [73–80] A sample is illuminated with a laser beam. The reflected light consists of both elastic and inelastic components. The elastically scattered light is filtered out and the rest is collected by a detector. The analysis of the light intensity as a function of frequency can give information about the imperfections in the solid.

Raman spectroscopy is widely used to determine the number of layers of graphene and characterise the defects in it [74–78, 81, 82]. The Raman spectrum of graphene consists of several peaks in reflected intensity at certain frequencies [83]. Each of them can give information on different features in the samples. First we consider electron scattering off photons within one valley. Electron can absorb a photon and

get excited from the valence into the conduction band leaving a hole behind (Fig. 2.8(a)). There it first relaxes to a virtual level and then recombines with a hole producing a photon with smaller energy. This process gives rise to peak G. The electron can relax via phonon scattering to a real level in the conduction band after excitation (Fig. 2.8(b)). Then it recombines with the hole via defect scattering. This gives rise to the D′ peak. And finally the electron can relax to a real level in the conduction band, then to a real level in the valence band, and eventually it recombines with the hole (Fig. 2.8(c)). This is a two-phonon process and it gives rise to the 2D′ peak. There are two other peaks, which appear when the electron is scattered between the valleys. The D peak appears similarly as the D′ does with an exception that the electron relaxes to a real level in the other valley and then it recombines with the hole via defect scattering (Fig. 2.8(d)). The 2D peak is an analogue of the 2D′ peak in that the electron is scattered between the valleys (Fig. 2.8(e)).

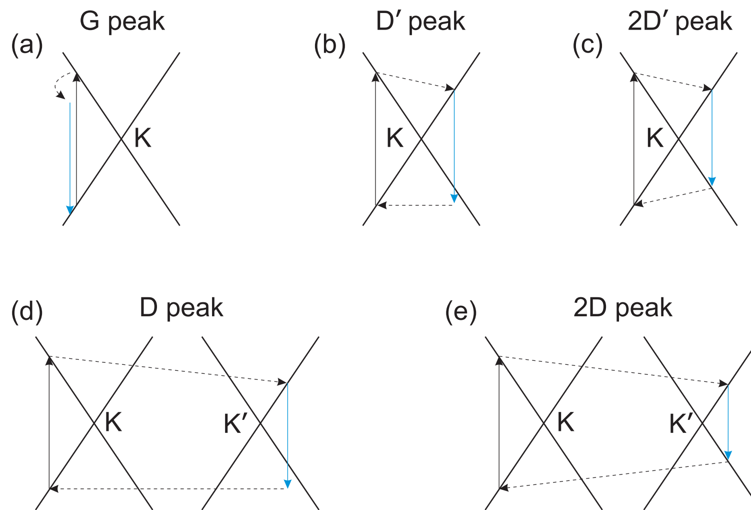

Figure 2.8: Scattering processes that take place in the Raman effect giving rise to (a) intra-valley one-phonon G peak, (b) defect-assisted intra-valley D′ peak (c) intra-valley two-phonon 2D′ peak, (d) defect-assisted inter-valley D peak, (e) inter-valley two-phonon 2D peak.

The D peak appears only if there are defects (e.g. missing atoms) in the system. In a defect-free graphene the D peak is absent. In order to determine the number of layers of graphene, one should study the shape of the 2D peak. For monolayer graphene the width of the 2D peak at half-maximum should be ~ 30 cm^{-1} and the peak itself is symmetric.

If the number of graphene layers is more than 1, then the width of the 2D peak gets broadened and becomes asymmetric [81, 82, 84–87].

Chapter 3

Fabrication, sample characterisation and instrumentation

In this Chapter we go through the fabrication process of graphene devices starting from deposition of graphene on top of a substrate and finishing with loading graphene transistors into low-temperature cryostats. At different stages of this routine we can determine the number of graphene layers in samples we work with. We consider a number of different methods to determine the number of layers. We also discuss the principles of operation of low-temperature cryostats, which are used for electron transport measurements presented in this thesis.

3.1 Fabrication of graphene transistors

Fabrication of graphene devices starts with a few millimeter sized piece of natural graphite. Graphite has a layered structure [88]. The crystal structure of a single layer was discussed in Chapter 1. The separation between graphene planes is 0.34 nm, therefore a few millions of them will make up a millimeter thick graphite crystal.

In order to remove one layer of carbon atoms from graphite, a mechanical exfoliation technique is used [1]. An adhesive tape is used repeatedly to cleave a graphite piece into thinner layers. At the final stage of exfoliation, the tape with graphite flakes on it is placed face down and pushed onto the silicon/silicon dioxide (Si/SiO_2)

Figure 3.1: An optical image of monolayer graphene (encircled area) on top of Si/SiO_2.

substrate. A substrate is necessary, because graphene itself was predicted not to exist in the free state [89–92]. After deposition the substrates with flakes are covered with a layer of resist (polymethylmethacrylate, PMMA). At first, this layer protects graphene from surrounding atmosphere, which lowers the quality of samples by doping, and then it is used to make contacts using electron-beam lithography [93].

The exfoliation technique does not allow control of the number of graphene layers in individual flakes. Flakes deposited on top of Si/SiO_2 consist of different number of layers, and it is therefore necessary to search for a sample with a required thickness. This is done with an optical microscope. Although graphene is one atom thick, it is possible to see it under the microscope (Fig. 3.1) due to contrast of graphene with respect to the underlying substrate [94]. The graphene contrast is due to interference of light waves scattered from graphene itself and the bottom edge of SiO_2. Depending on the thickness of SiO_2, one should use different filters in order to maximise the contrast difference. For example, a green filter makes graphene visible on top of 300 nm SiO_2. Almost all samples that are described in the thesis are deposited on the 300 nm thick silica.

Experiments discussed in the following chapters were performed on monolayer graphene and the green filter was used to find the flakes. At this stage one can verify that the found flakes are single-layers, which can be done by measuring the Raman spectra. After the flakes have been located, electron beam lithography is

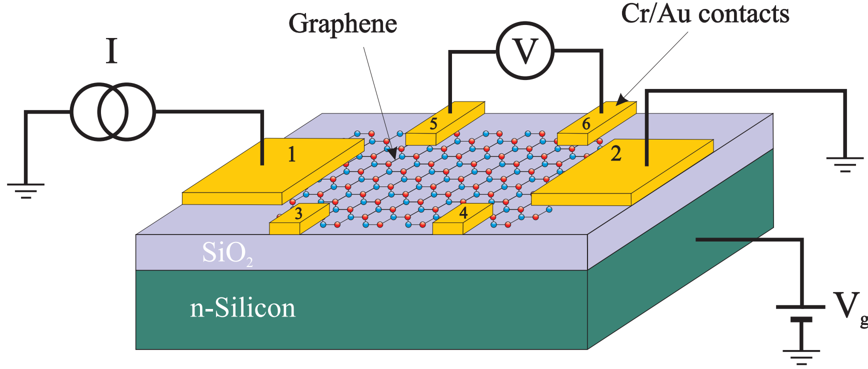

Figure 3.2: Schematic of the transistor. The carrier density is tuned by applying a voltage, V_g, between the n-doped silicon and graphene. The current is driven between contacts 1 and 2, the longitudinal resistivity ρ is measured between 3 and 4 (or 5 and 6), and the transverse resistivity between 3 and 5 (or 4 and 6).

used to pattern contacts on top of them. This procedure finishes with removing the exposed regions of the resist ('developing'). After that 5 nm of chrome (Cr) and 40 nm of gold (Au) are evaporated on top of the substrate covering its entire surface. A subsequent process called 'lift-off' removes the resist from the substrate together with the evaporated metal. Metal only remains in areas exposed to the electron beam. The final step of graphene device fabrication is to connect samples on the substrate to electrical contacts of a chip carrier using an ultrasonic wire bonding technique.

The procedure described creates a graphene transistor (Fig. 3.2), in which a silicon layer, being highly doped, acts as one metal plate (gate) of a plane capacitor and the graphene flake as the other one. Applying a voltage to the gate changes the carrier density in the sample (field effect). Electron-beam lithography is used to make multiterminal devices, which allows measurements of the four-terminal resistance. All measurements are performed in a constant current regime. The current is driven between contacts 1 (source) and 2 (drain). The longitudinal resistance, R_{xx}, is measured between 3 and 4 (or 5 and 6), and the transverse resistance, R_{xy}, between 3 and 5 (or 4 and 6). The conductivities are then calculated: $\sigma_{xx} = 1/\rho_{xx} = (1/R_{xx})(L/W)$, where ρ is the resistivity, L and W are the length and the width of a sample, respectively, and $\sigma_{xy} = 1/R_{xy}$.

The capacitance of a such capacitor is $C = \epsilon_r \epsilon_0 S/d$, where ϵ_0 is the electric constant, ϵ_r is the relative permittivity, S is the area of plates and d is the distance

between the plates (thickness of SiO_2). On the other hand $C = Q/V_g$, where Q is the charge of a plate and V_g is the voltage applied to the plates (gate voltage). From the two equations we get: $\epsilon_r \epsilon_0 S/d = Q/V_g$. The charge Q can be expressed as $Q = eN$, where e is the electron charge and N is the number of electrons in a plate. Thus, applying a voltage to the gate increases the electron density by $n = N/S = (\epsilon_r \epsilon_0 / de) V_g$. For 300 nm thick SiO_2 , $n = 7.2 \cdot 10^{10} V_g$ (cm^{-2} V^{-1}).

After the contacts to graphene have been made, a sample can be loaded into a low-temperature cryostat to perform electron transport measurements. At this stage it is also possible to verify that the sample is monolayer graphene by measuring the quantum Hall effect, QHE (Chapter 2). Apart from measurements of the Raman spectrum and the QHE, the number of layers can be determined using an atomic force microscope. This should be done when graphene is deposited on top of Si/SiO_2 but before it is covered with PMMA, or when a graphene transistor is made.

3.2 Determining the number of layers

We consider three methods to determine the number of graphene layers in a sample. They are based on measurements of the Raman spectrum of graphene, QHE and AFM topography. Examples for each of the methods will be shown.

3.2.1 Raman spectrum

The use of the Raman spectrum to determine the number of layers in a sample is based on analysis of the G and 2D peaks. The Raman data are recorded by using a laser with a wavelength of 532 nm. The power of the excitation laser is restricted to 5 mW in order to avoid sample damage by heating.

Figure 3.3 shows an example of such a spectrum for graphene. As expected (e.g. [83]) the G and 2D peaks appear at 1580 and ∼2700 cm^{-1}, respectively. The 2D peak is symmetric and its width at half maximum can be determined by fitting the peak with a Lorentzian function (see inset in Fig. 3.3). The fit gives 30 cm^{-1}. One can also see that the intensity of the 2D peak is higher than that of the D peak. Thus, the studied samples are monolayers graphene.

Note that the D peak, which is expected at 1350 cm^{-1}, is very small. This

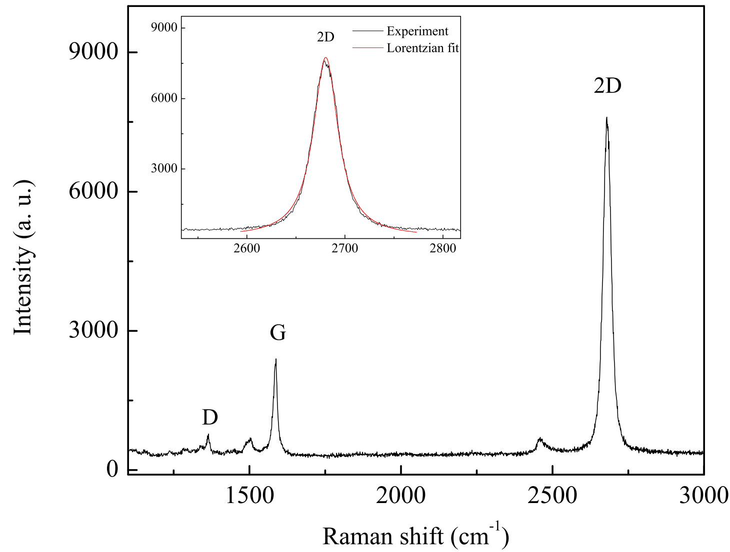

Figure 3.3: The Raman spectrum of graphene. The symmetric 2D peak, G peak and the defect-assisted D peak are shown. The inset shows a fit of the 2D peak with the Lorentzian function. The fit gives the width of the peak at half maximum of ~ 30 cm^{-1}, which indicates that the studied sample is monolayer graphene.

indicates high quality of the graphene sample and absence of sharp defects.

3.2.2 Quantum Hall effect

As we discussed in the previous chapter the QHE in graphene is different compared to that in 2D-systems with parabolic dispersion relation. The quantised values of the conductivity, $\sigma = 4\nu e^2/h$, appear at integer filling factors in conventional systems and at half-integer ν in graphene. Therefore, the QHE measurements can give information about the number of layers in a studied sample. In this work we study the QHE at a temperature of 4.2 K and in a magnetic field of 14 T. The longitudinal and transverse resistivities, ρ_{xx} and ρ_{xy}, are measured as a function of the carrier density. These are then used to calculate the transverse conductivity: $\sigma_{xy} = \rho_{xy}/(\rho_{xx}^2 + \rho_{xy}^2)$. Figure 3.4 shows the results of the QHE measurements. One can see that the plateaus appear at half integer filling factors, which shows that the samples are monolayers [9, 10]. The same result was obtained for all samples described in the thesis.

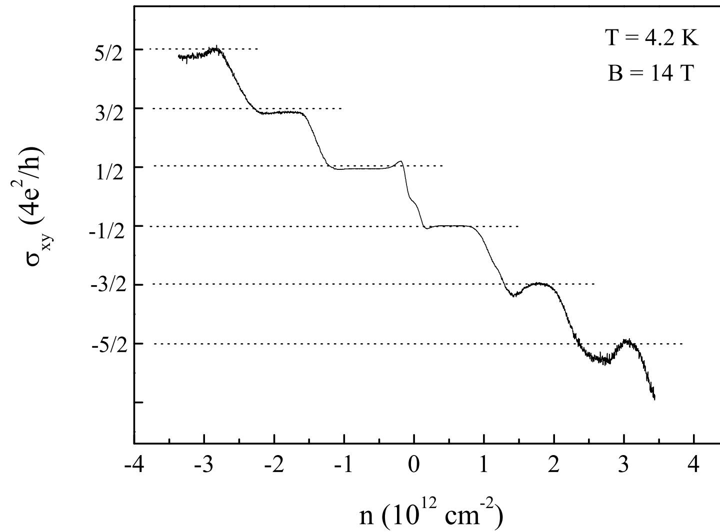

Figure 3.4: Quantum Hall effect measured at 4.2 K and 14 T. Plateaus at half-integer filling factors prove that the studied samples are monolayers.

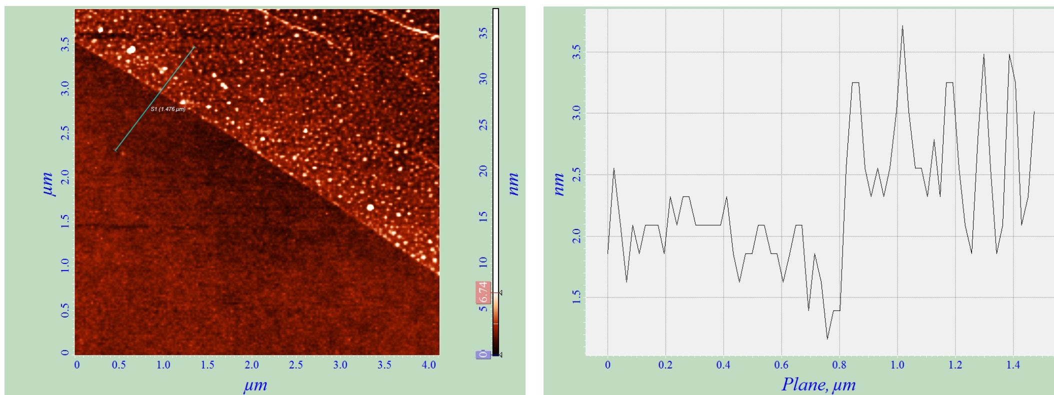

Figure 3.5: (a) Atomic force microscopy image of graphene and (b) a profile taken along a blue line in (a). The profile shows a clear step in height of < 1 nm, which indicates that the sample is single layer graphene.

3.2.3 AFM topography

An atomic force microscope can be used to construct a profile of the surface of the substrate and a sample. This profile in turn can be used to determine the height of the sample with respect to Si/SiO_2. As was mentioned earlier the distance between graphene layers in graphite is 0.34 nm. Therefore, the height of 0.34 nm is expected for monolayer graphene. However, due to the presence of contaminations, e.g. residues of PMMA or dirt from the atmosphere, the actual height, h, can be larger. Experience shows that $h \lesssim 1$ nm is usually observed. Figure 3.5 shows an AFM profile of graphene on Si/SiO_2. The measured height of the sample turns out

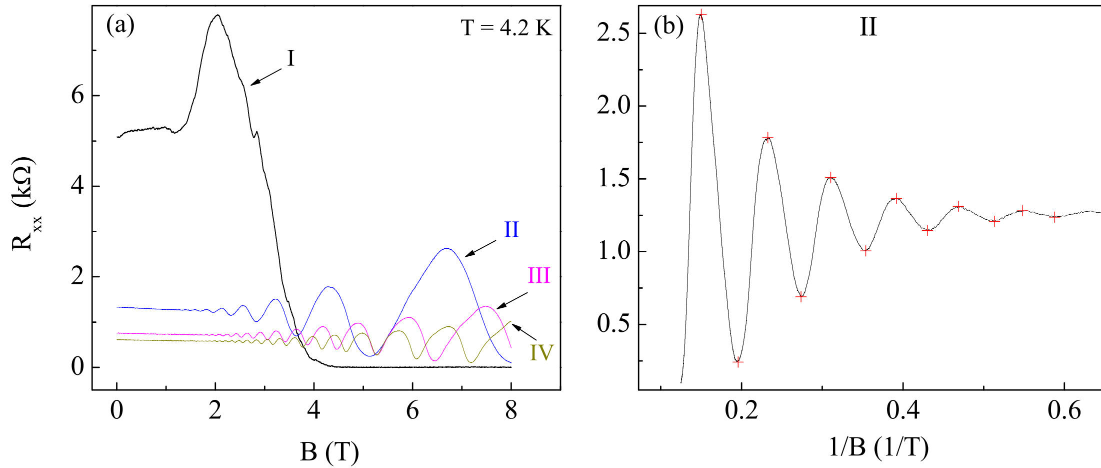

Figure 3.6: (a) Shubnikov-de Haas oscillations at four different carrier densities, which are denoted as regions I, II, III and IV. These regions correspond to 0.2, 1.15, 2.6 and $3.5 \cdot 10^{12}$ cm^{-2}, respectively. The measurements are performed at 4.2 K. (b) SdH oscillations shown for region II as a function of $1/B$. Red crosses correspond to the positions of the peaks in the resistance.

to be < 1 nm, which indicates that it is monolayer graphene.

3.3 Determining the carrier density in graphene from SdH oscillations

Despite the fact that the Si/SiO_2 substrates are grown with a nominal oxide thickness of oxide of 300 nm, there can be variations in the manufacturing process, which vary the thickness and quality of the layer. These contaminations can form a charged layer, which can screen the electric field between silicon and sample when the gate voltage is applied. In both cases the carrier density calculated theoretically ($n = 7.2 \cdot 10^{10} V_g$ cm^{-2}) can be different from the real one. To avoid this the Shubnikov-de Haas oscillations can be used to determine the carrier density at each studied gate voltage using equation (2.21). Below is an example of such measurements that show that the real thickness of the oxide is 280 nm.

The longitudinal resistance is measured at a fixed gate voltage as a function of the magnetic field $R_{xx}(B)$ (Fig. 3.6(a)). Then it is plotted as $R_{xx}(1/B)$, which shows oscillations equidistant from each other (an example for region II is shown in Fig. 3.6(b)). The positions of two closest peaks are determined and equation (2.21) is used to calculate the carrier density. The resultant n is divided by the value of

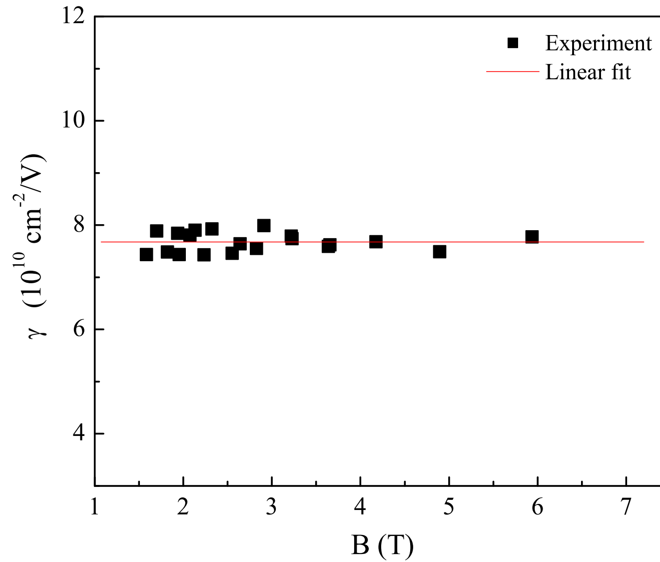

Figure 3.7: The dependence of the coefficient γ as a function of magnetic field for regions II and III in Fig. 3.6(a). The averaged value of γ is $7.7 \cdot 10^{10}$.

the gate voltage to calculate the coefficient γ ($n = \gamma V_g$). When this is done for all peaks in the resistance, the obtained values of γ are averaged. This result is shown in Fig. 3.7.

Analysis of the SdH oscillations has shown that $n = (7.7 \pm 0.2) \cdot 10^{10} V_g$ (cm^{-2}), which corresponds to the thickness of SiO_2 of 280 ± 10 nm.

3.4 Instrumentation and measurements

In order to study quantum phenomena, low temperatures are required. Low temperatures are obtained by pumping on a liquid bath. Depending on the sort of liquid the lowest temperature upon pumping can be different. In this chapter we consider such low-temperature cryostats as the ^{3}He system and the dilution refrigerator.

3.4.1 Helium-3 cryostat

We start with the ^{3}He cryostat. The choice of liquid to be pumped can be different. In case of liquid helium-4 (^{4}He) pumping makes it possible to achieve $\sim$ 1.2 K, whereas the lowest limit for ^{3}He is 0.25 K. The reasons for the difference in the lowest achievable temperatures (base temperatures) for ^{3}He and ^{4}He are the following [95]. The vapour pressure of ^{3}He is always higher than that of ^{4}He, because the zero point

motion is higher for the lighter ^{3}He atom. Also, the ^{3}He superconducting film is absent. Therefore there is no heat link between liquid ^{3}He and parts of the cryostat, which have higher temperatures.

At low temperature when ^{3}He is liquid, there is vapour above it, which can be treated as an ideal gas. In this case one can write the Clausius-Clapeyron equation:

$$\frac{dP}{dT} = \frac{LP}{RT^2} , \tag{3.1}$$

where P is the vapour pressure, L is the latent heat of evaporation, R is the universal gas constant. From this equation one can find the vapour pressure:

$$P \propto e^{-L/RT} . \tag{3.2}$$

Equation (3.2) shows that the vapour pressure of ^{3}He decreases during cooldown. Since the mass flow is proportional to P, the cooling power decreases when ^{3}He temperature goes down. At some point the cooling power equates the external heat link and an equilibrium temperature settles. For the ^{3}He cryostat this temperature is 0.25 K.

In this section we discuss the Oxford Instruments ^{3}He top loading (TL) system, Heliox TL. Top loading means that a probe with a sample is loaded from the top of the cryostat and immersed into the liquid ^{3}He.

There are three working parts in the ^{3}He system that are used to cool the sample down to the base temperature (Fig. 3.8). The first part is the sorption pump (sorb). When it is cold, it acts as a pump and absorbs the He gas. When it is heated, it releases all the gas that has been absorbed. The second part is the 1 K Pot. This is a small vessel located below the sorb, which is filled with liquid ^{4}He via a needle valve. The needle valve connects the 1 K Pot with the main bath, which is filled with liquid ^{4}He. The main bath has to be refilled regularly. The 1 K Pot is connected to a rotary pump, which cools the 1 K Pot down to $\sim$ 1.2 K. And the last part is the sample space, which is located at the bottom of the cryostat. The sample space is a place where the sample is lowered to and liquid ^{3}He is collected. When the sample is inserted into the system, the sorb is heated to 30 K to release the ^{3}He gas. The

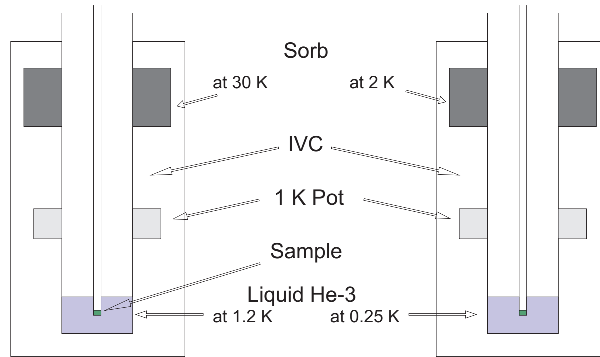

Figure 3.8: Principle of operation of the ^{3}He system. Picture of the left: the sorb at 30 K releases ^{3}He gas, which condenses passing through the 1 K Pot at 1.2 K. Liquid ^{3}He at 1.2 K is collected in the sample space. Picture on the right: When all ^{3}He has been condensed, the sorb temperature should be reduced to 2 K for it to start pumping the vapour above liquid ^{3}He. The pumping decreases the temperature of ^{3}He down to 0.25 K.

gas passing through the 1 K Pot is condensed, collected in the sample space and cools the sample to the temperature of the 1 K Pot, which is $\sim$ 1.2 K. When all gas is condensed in the sample space, the sorb should be cooled down. Then it starts pumping the vapour pressure above liquid ^{3}He, and the sample temperature drops to the base temperature.

The three working parts are located in the inner vacuum chamber (IVC) to provide thermal isolation from the main bath. To prevent quick evaporation of liquid ^{4}He from the main bath it is surrounded by the outer vacuum chamber (OVC).

The Oxford Instruments Heliox TL used in this work allows measurements in a wide range of temperatures (0.25 - 300 K) and high magnetic fields (0 - 15 T).

3.4.2 Dilution refrigerator

The principle of operation of the dilution refrigerator is based on the use of the mixture of ^{3}He and ^{4}He. As it was already mentioned pumping the vapour pressure above liquid ^{4}He reduces the temperature to 1.2 K and above ^{3}He – to 0.25 K. The mixture of the two isotopes of helium makes it possible to achieve much lower temperatures.

When the temperature of the mixture drops down to a certain temperature, it separates into two phases: the concentrated phase rich in ^{3}He and the diluted phase rich in ^{4}He. The diluted phase is heavier than the concentrated one, therefore the ^{3}He

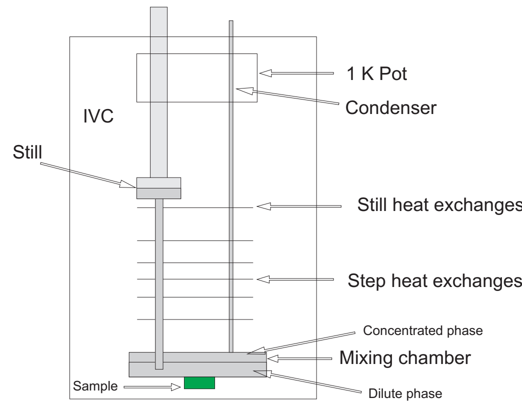

Figure 3.9: Schematic diagram of the dilution refrigerator.

rich phase is above the ^{4}He rich phase. When atoms of ^{3}He from the concentrated phase move across the boundary to the diluted phase, the cooling is produced. In the dilution refrigerator this process is continuous due to the circulation of ^{3}He by pumping.

The work of the dilution refrigerator [95] starts with the mixture coming from the dump to the condenser, where the 1 K Pot at a temperature of 1.2 K condenses the gas (Fig. 3.9). The liquid then enters the mixing chamber (MC). The circulation starts by pumping with a rotary pump. The osmotic vapour pressure gradient drives the liquid to the still, where its temperature decreases further down to ~ 0.8 K. This cooling is possible due to the higher vapour pressure of ^{3}He compared to ^{4}He. Therefore, it is ^{3}He that circulates.

The phase separation occurs at temperature below 0.86 K and is called the tricritical temperature. At this stage the heat is applied to the still to increase the gas circulation rate. Between the mixing chamber and the still there are the still heat exchanger and step heat exchangers. The still heat exchanger allows cooling the mixture to 0.8 K after it has passed the condenser. Therefore, the liquid enters the MC at 0.8 K. When ^{3}He atoms cross the phase boundary, the temperature of the mixture drops below 0.8 K. On its way to the still the step heat exchanger cools the mixture coming from the condenser and the still heat exchanger further down. This procedure is repeated as long as there is gas circulation and cools the mixture in the mixing chamber down to the base temperature.

The sample to be measured is mounted below the MC and a direct thermal link cools the sample to the base temperature.

We use the Oxford Instruments Kelvinox 300 dilution refrigerator. The temperature in this system can be varied between 20 mK and 4 K and an incorporated superconducting magnet can produce magnetic fields of up to 18 T.

Chapter 4

Quantum corrections to the conductivity at high temperatures

In this chapter we discuss the experimental results of the investigation of the weak localisation and electron-electron interaction corrections at temperatures between 5 and 200 K. We begin with measurements and analysis of magnetoconductivity in graphene and determine the characteristic lengths responsible for WL. We show that WL in graphene is very unusual compared to conventional 2D systems. For example, quantum interference in graphene survives at temperatures up to 200 K, whereas in systems with a parabolic dispersion relation WL is usually observed below 50 K. Depending on experimental conditions, temperature and carrier density, we observe a transition from weak localisation to antilocalisation. Before the advent of graphene, such a transition was only observed as a function of the gate voltage.

The transition can be observed in both MC and the temperature dependence of the conductivity. In the latter there is also the EEI correction, which we study separately and determine the value of the Fermi-liquid constant.

We also show for both quantum corrections the importance of the elastic scattering.

4.1 Field effect in graphene

The studied graphene sample S1, being 22.5 μm long and 2 μm wide, was produced by mechanical exfoliation of graphite as described previously. Electron-beam lithography was used to make a six-terminal device. This allowed measurements

of the longitudinal and transverse resistance using the 4-terminal van der Pauw method [96] without taking into account the resistance of the contacts. The device was then loaded into the low-temperature cryostat. Before cooling down, the sample was annealed in vacuum ($\sim 10^{-6}$ mbar) at 140°C for two hours to remove contaminations, e.g. water, from the surface of the sample.

In this experiment [97] we measure magnetoconductivity at different temperatures and carrier densities. The latter can be changed by applying a voltage to the gate. The measurements are performed in a constant current regime ($I = 10$, 50 or 100 nA depending on the carrier density and temperature). The typical dependence of the resistance on the gate voltage, $R(V_g)$, or the carrier density is shown in Fig. 4.1. At a certain gate voltage the resistance has the largest value (the peak in the dependence). This point is called the electro-neutrality (NP) or the Dirac point and corresponds to the point where the conduction and valence bands cross each other (Fig. 1.3(a)). In pristine graphene (with no contaminations) the NP is at zero gate voltage [9, 98]. Here the resistivity is expected to be very large, because the density of states is very small (Fig. 1.3(b)). The behavior of charge carriers at the Dirac point is a delicate issue and it is beyond the scope of this thesis. In real samples the resistivity at this point is finite [7] and the position of the NP is always shifted in the gate voltage due to unintentional doping by e.g. water or chemicals left during fabrication, etc. The annealing procedure removes some part of these contaminants and moves the NP closer to $V_g = 0$.

The NP divides the $R(V_g)$ dependence into two branches (Fig. 4.1). The left (negative carrier density) branch corresponds to adding holes to the system and the right (positive carrier density) to adding electrons. In both cases, as expected, the resistance drops.

The passage of an electrical current through a sample causes Joule heating [99], which is proportional to the current squared and the resistance. This heating can warm the sample and so its effective temperature can differ from what a temperature controller shows. The heating of the sample changes its resistance, which is temperature-dependent [57–59, 100, 101]. To prevent this from happening we measure the gate voltage dependences of the resistance at different source-drain currents. If the electrons are overheated by current, then when it is decreased, one would see that the resistance changes (e.g. increases at low temperatures). At some point

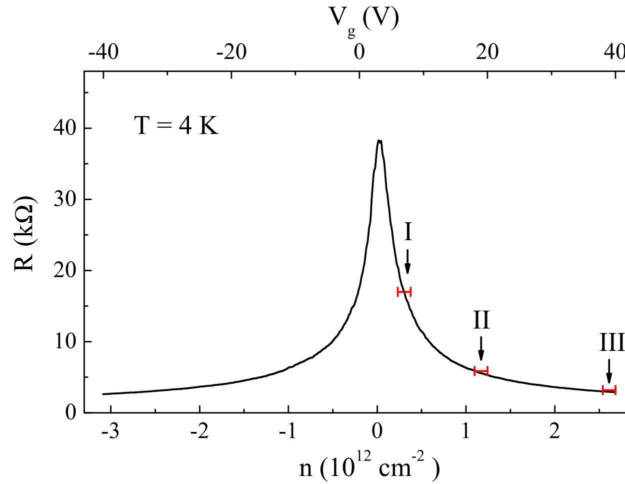

Figure 4.1: The resistance of the sample as a function of the carrier density or the gate voltage. The point where the resistance is maximum is the electro-neutrality point (NP). Regions I, II and III correspond to the carrier densities 0.2, 1.15 and $2.6{\cdot}10^{12}$ cm^{-2}, respectively, where weak localisation is studied.

the resistance stops changing and the current that this resistance corresponds to is suitable for measurements. In this experiment the current was varied between 1 and 100 nA depending on the carrier density and temperature (these two parameters affect the resistance of the sample). For example, at low T and n, small currents are required. At high n or high T the current can be increased. A more detailed analysis (with examples) of electron overheating in experiments will be given in Chapter 5 where the quantum corrections are studied at temperatures down to 20 mK, at which the overheating is more topical.

4.2 Weak localisation

We study WL in three different regions of the carrier density indicated in Fig. 4.1 by red bars. These regions named I, II and III correspond to 3, 16 and 36 V with respect to the NP.

One of the ways to detect weak localisation is to apply a low magnetic field perpendicular to a sample and measure the conductivity (MC) [11]. The magnetic field adds a phase difference to the two electron waves and destroys interference between them (see equation (2.26) and Fig. 2.3).

The studied sample is relatively small, therefore at low temperatures the UCF

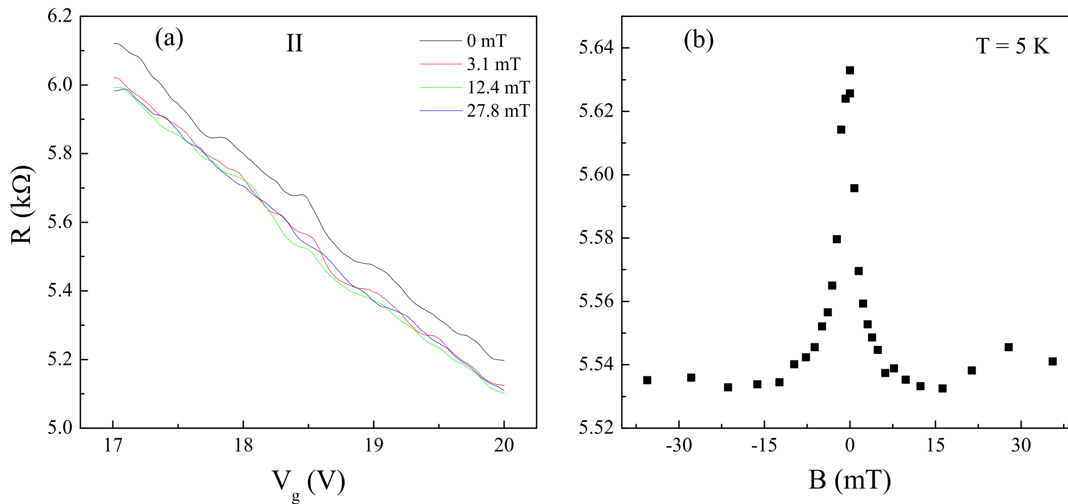

Figure 4.2: (a) The resistance of the sample as a function of the gate voltage measured at 5 K in a narrow window of V_g (shown for region II as an example). For simplicity only four curves, which correspond to different magnetic fields, are shown. (b) The result of averaging of the curves in (a).

can be noticeable and they have to be averaged out in order to study the WL more carefully. Figure 4.2 shows how the averaging is performed. The resistance of the sample in each region is measured as a function of the gate voltage in a narrow window of V_g: for region I the window is $\Delta V_g = 1$ V, for region II $\Delta V_g = 3$ V and for region III $\Delta V_g = 4$ V. The resistance is then averaged over this window. Then the magnetic field B is increased by a few milli Tesla and the resistance is measured in the same range of the gate voltages. The gate voltage window should on one hand be small in order not to change the resistance too much, otherwise the studied system will be different. On the other hand, the range should be large for it to consist of many periods of the UCF. The measurements and averaging are performed for both positive and negative values of the magnetic field between -30 and 30 mT. As a result of averaging, a set of points, which correspond to the resistance at different magnetic fields, will appear (Fig. 4.2(b)). One can see that the dependence in the figure is slightly asymmetric due to the mixture of the longitudinal and transverse resistances [102]. The symmetric part, R_s, of the curve is extracted using a relation $R_s(B) = (R(B)+R(-B))/2$. It is then converted to the magnetoconductivity (MC) $\Delta\sigma(B) = \sigma(B)-\sigma(B=0) = -(L/W)\Delta R_s(B)/[R_s(B)R_s(B=0)]$. When the above is done at a given temperature, it is changed and the measurements and analysis are repeated. The obtained MC curves are then analysed using equation (2.27) and

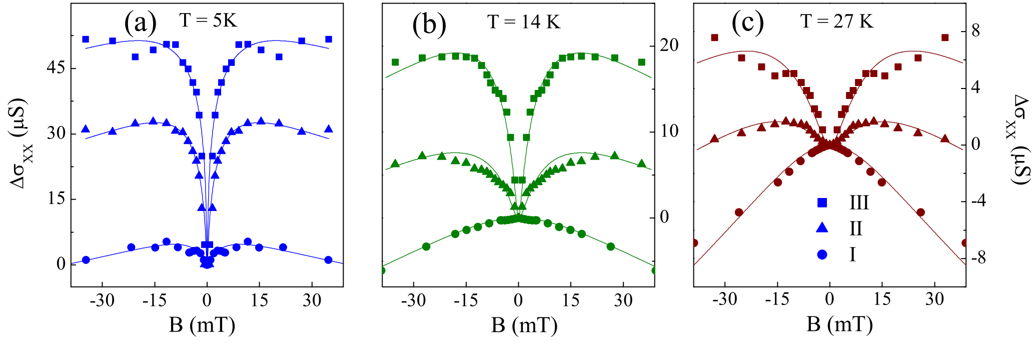

Figure 4.3: Evolution of the magnetoconductivity as a function of the carrier density shown at three different temperatures. The solid curves are fits to equation (2.27).

the three characteristic lengths, L_φ, L_i and L_*, are extracted.

4.2.1 Transition from weak localisation to antilocalisation

In order to study the effect of experimental conditions on WL, we carry out two types of experiment. In the first experiment we fix the temperature and study the MC at different carrier densities. The result of measurements and averaging is shown in Fig. 4.3 for three different temperatures: 5, 14 and 27 K. It is seen that at the lowest temperature the MC is positive at all studied carrier densities n. This is an indication that WL takes place under these experimental conditions. As we increase n, WL becomes stronger (the dip in the MC becomes narrower), because of the increasing dephasing length due to adding more electrons to the system, which screen the impurities (see Chapter 2). At $T = 14$ and 27 K one can see that with decreasing electron density the MC changes its sign from positive (region III) to negative (region I).

The analysis of the MC curves using equation (2.27) shows that the dips in the dependences at small B are mainly controlled by τ_φ, whereas the bendings of the curves are determined by τ_i and τ_*. As in the previous experiments on WL [34] the elastic times τ_i and τ_* are temperature independent and the dephasing time decreases with increasing temperature and decreasing carrier density. A transition from WL to WAL is observed, because the ratio of the characteristic times is seen to enter the region of antilocalisation as shown in Fig. 2.5. At $T = 5$ K the value of τ_φ is larger, therefore one cannot achieve the transition from WL to WAL because of the large values of τ_φ/τ_* and τ_φ/τ_i.

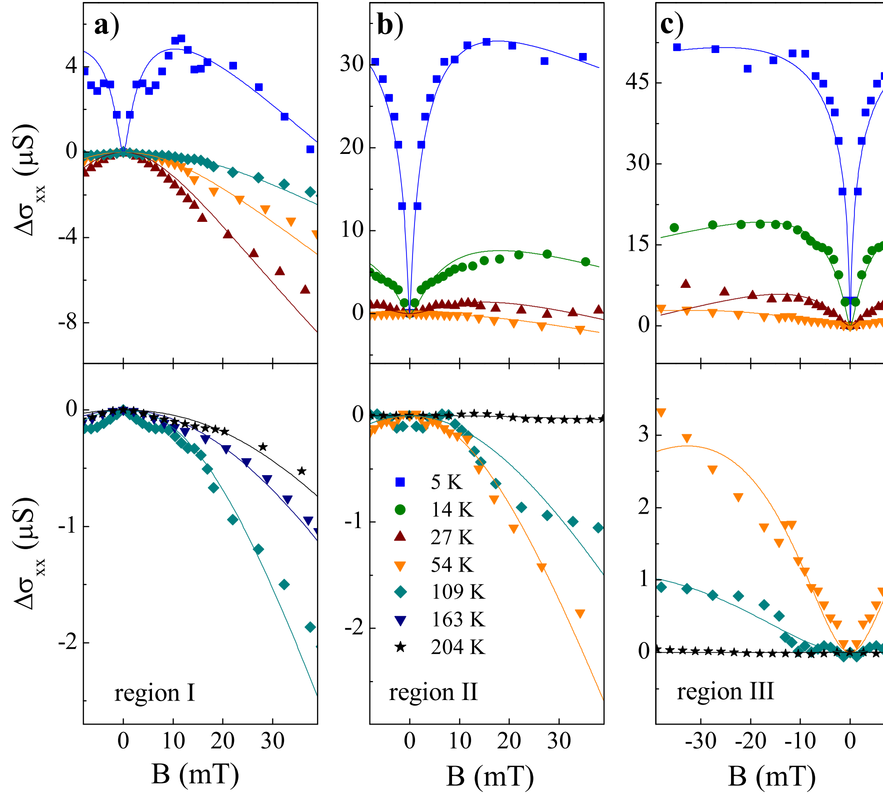

Figure 4.4: Evolution of the magnetoconductivity as a function of the temperature. The bottom panel is a zoomed-in view for high temperatures. The solid curves are fits to equation (2.27).

In the second experiment we fix the carrier density and measure the MC at different temperatures. The measurements and averaging are performed in the same way as for the first experiment. The result is shown in Fig. 4.4 for regions I, II and III. At 5 K we observe a positive MC (WL). As the temperature is increased the dip in the MC becomes wider until the dependence flattens at ~ 10 K in region I (not shown) and at 27 K in region II. At higher temperatures the sign of the MC changes to negative and a peak (instead of a dip) in the dependences is observed,

Table 4.1: The inter- and intra-valley scattering times (in ps) extracted from the analysis of the MC. Errors come from the fitting procedure.

Region	τ_i	τ_*
I	14.0 ± 3.0	0.45 ± 0.05
II	3.0 ± 0.4	0.30 ± 0.02
III	1.0 ± 0.2	0.35 ± 0.02

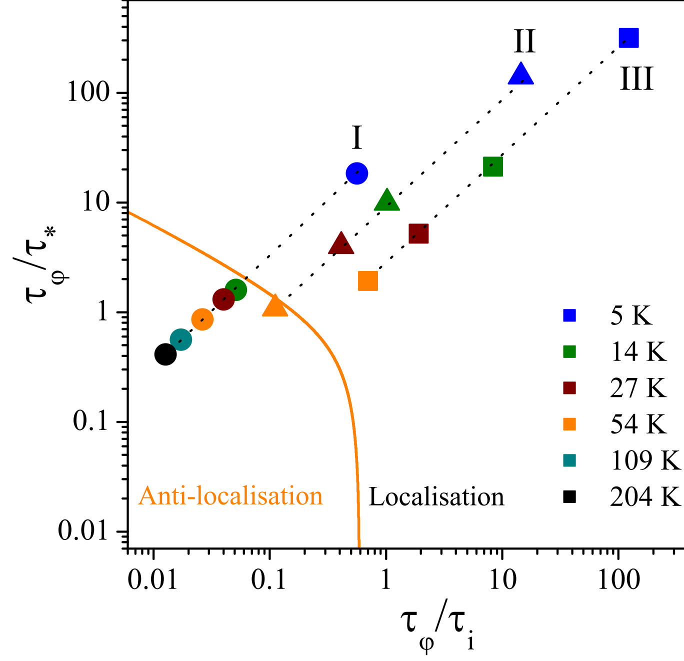

Figure 4.5: Conditions to observe WL and WAL in graphene. Orange curve corresponds to $\Delta\sigma(B) = 0$ in equation (2.28). The ratios of τ_φ/τ_* and τ_φ/τ_i, for which $\Delta\sigma(B) > 0$ (area above the curve), indicate WL. In the opposite case (area below the curve) they indicate WAL. Point are experimental values found from the analysis of the magnetoconductivity.

indicating a transition from WL to WAL. At $T > 100$ K the width of the peak increases (electron interference is being suppressed) due to dephasing of electron waves until the MC curve flattens again at 200 K in region II. In region III there is no transition from WL to WAL. The absence of the transition is again due to the large values of τ_φ/τ_* and τ_φ/τ_i. Since L_φ is larger at lower temperatures the WL correction is the strongest at 5 K for all regions. Similarly to the experiment shown in Fig. 4.3, the observed transition from positive MC to negative MC is explained due to the variations in the ratios τ_φ/τ_i and τ_φ/τ_* (Fig. 4.5). The values of τ_i and τ_* obtained from the MC are given in Table 4.1.

The two described experiments show that in graphene there is a transition from WL to WAL as a function of the carrier density and the temperature. The latter has never been observed in any other systems before. The transition has been observed as a function of the gate voltage [103, 104], where the applied V_g tuned the strength of the spin-orbit interaction.

Unusually, the quantum interference in graphene survives at very high temper-

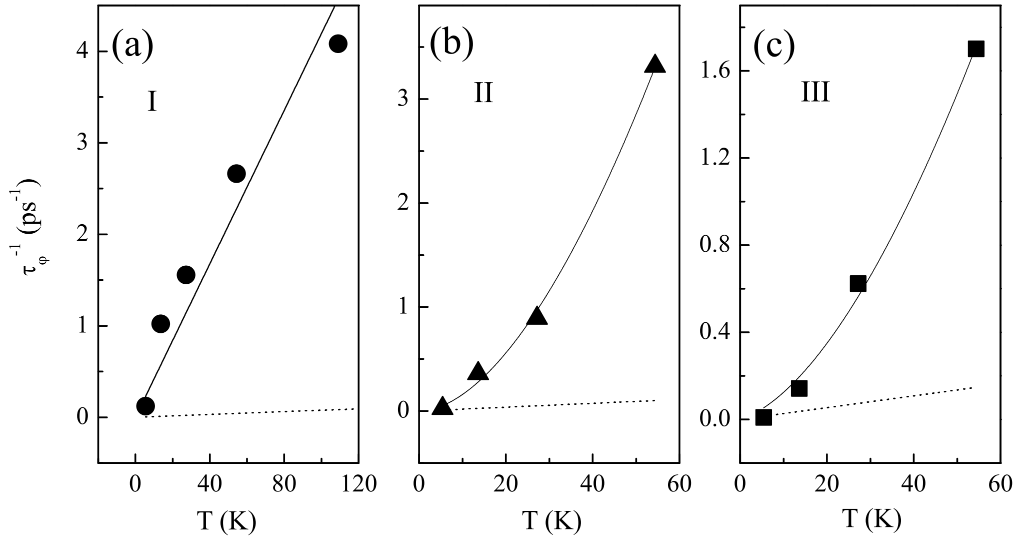

Figure 4.6: Temperature dependence of the dephasing rate. Solid lines are expectations from electron-electron interaction found as a sum of equations (4.1) and (4.3): (a) $\alpha = 1.5, \beta = 0$; (b) $\alpha = 1.5, \beta = 2.5$; (c) $\alpha = 0, \beta = 2.5$. Dotted lines are dephasing rates calculated using equation (4.2).

atures, up to 200 K (Fig. 4.4(a)). In conventional 2D systems WL is usually not observed above ~ 50 K [23–33] because of strong electron-phonon scattering.

4.2.2 Temperature dependence of the dephasing rate

In order to understand why the electron interference in graphene can be seen at such high temperatures, we investigate the temperature dependence of the dephasing rate τ_φ^{-1}.

We consider two mechanisms that can cause electron dephasing [21,22]: electron-electron and electron-phonon interactions. In the previous studies of τ_φ^{-1} the dependence was found to be linear as a function of temperature [34] corresponding to electron-electron scattering in the diffusive regime [21]:

$$\tau_\varphi^{-1} = \alpha \frac{k_B T}{2\varepsilon_F \tau_p} \ln\left(\frac{2\varepsilon_F \tau_p}{\hbar}\right) , \quad (4.1)$$

where ε_F is the Fermi energy, τ_p is the momentum relaxation time and α is a coefficient of the order of unity. This regime corresponds to the condition $k_B T \tau_p / \hbar < 1$, which means that two interacting electrons experience many collisions with impurities during the time of their interaction, $\hbar / k_B T$. Figure 4.6 shows the temperature

dependence of the dephasing rate in regions I, II and III. The values of τ_φ^{-1} were obtained from the analysis of the MC using equation (2.27). At temperatures above 120 K in region I and 60 K in regions II and III the values of τ_φ become smaller than the mean free time. This is not physical, therefore the range of temperatures in Fig. 4.6 is reduced compared to that shown in Fig. 4.4. The expected rates due to electron-electron and electron-phonon scattering are shown by solid and dashed lines, respectively. Phonons give the following contribution to the dephasing rate:

$$\tau_{e-ph}^{-1} = \frac{1}{\hbar^3}\frac{\varepsilon_F}{4\nu_F^2}\frac{D_a^2}{\rho_m s^2}k_B T \ , \tag{4.2}$$

where D_a is the deformation potential constant, ρ_m is the density of graphene, s is the speed of sound, and ν_F is the Fermi velocity. (In plotting the electron-phonon rate we have used the values $\rho_m = 7.6 \times 10^{-7}$ kg m^{-2}, $s = 2 \times 10^4$ m s^{-1}, $\nu_F = 10^6$ m s^{-1} and $D_a \approx 18$ eV which were used in the analysis of the temperature dependence of the classical conductance [57].) One can see that the electron-phonon rate is much smaller than the experimental dephasing rate. Moreover, the experimental dependence is not linear in regions II and III. This excludes not only electron-phonon but also electron-electron scattering in the diffusive regime as the main dephasing mechanisms. The alternative inelastic scattering mechanism is electron-electron scattering in the ballistic regime, which is realised at $k_B T \tau_p/\hbar > 1$, when electrons interact with each other without multiple impurity scattering. This gives a parabolic temperature dependence of the dephasing rate [22]:

$$\tau_\varphi^{-1} = \beta\frac{\pi}{4}\frac{(k_B T)^2}{\hbar\varepsilon_F}\ln\left(\frac{2\varepsilon_F}{k_B T}\right) \ . \tag{4.3}$$

Coefficients α and β in equations (4.1) and (4.3) are fitting parameters and according to the theory they should be of order unity. A transition temperature, T_0, between diffusive and ballistic regimes is determined from the condition $k_B T_0 \tau_p/\hbar \sim 1$: below T_0 the regime is diffusive, above T_0 it is ballistic. In region I the transition temperature is high, $T_0 \sim 80$ K, and the dephasing rate can be explained by the diffusive electron-electron interaction, equation (4.1). In regions II and III with $T_0 \sim$ 60 K and 40 K, respectively, the dephasing rate can be represented as a sum of the two rates, equations (4.1) and (4.3). Therefore, our results show that it is

electron-electron scattering which is the main source of high-temperature dephasing in graphene. Thus, it is the weakness of electron-phonon interaction that makes it possible to observe the quantum interference in graphene at very high temperatures.

Equation (4.2) that was used in the analysis of the temperature dependence of the dephasing rate represents the quantum time, τ_q, which is the time between any two scattering events. It is not the same as the momentum relaxation time τ_p, which is the time during which the momentum of a particle changes significantly (large-angle scattering contributes to τ_p). The quantum time represents any scattering regardless of angle. For short-range scatterers the two times are equal, because this type of scattering dominantly induces large-angle deflections. For long-range scattering $\tau_p > \tau_q$. In order to use equation (4.2) to fit the dephasing rate, it is necessary that $\tau_{e-ph} \equiv \tau_q \sim \tau_\varphi$. In graphene the use of this equation is justified. To prove it we first compare τ_q and τ_p.

The wavelengths of electrons and phonons are λ_e and λ_{ph}, respectively:

$$\lambda_e = \frac{2\pi}{k_F} \qquad \lambda_{ph} = \frac{2\pi}{q} \quad ,$$

where k_F and q are electron and phonon wave vectors, respectively. The ratio of the two wavelengths at $T > 10$ K in all studied regions is

$$\frac{\lambda_e}{\lambda_{ph}} = \frac{q}{k_F} = \frac{k_B T}{\varepsilon_F}\frac{\nu_F}{s} \gtrsim 1 \; ,$$

where s is the speed of sound. This equation means that electron scattering off phonons is large-angle scattering. Therefore, $\tau_q \sim \tau_p$.

Now we can estimate how much the electron phase changes during the time τ_{e-ph} [105]. During a collision the energy of the electron changes by $\Delta\varepsilon$ and its phase by $\Delta\varphi = \Delta\varepsilon\tau_{e-ph}/\hbar$. The energy and momentum conservation laws give the following change of the electron energy: $\Delta\varepsilon \sim \varepsilon_F s/\nu_F$. Thus, after a collision the phase of the electron changes by

$$\Delta\varphi = \frac{\Delta\varepsilon\tau_{e-ph}}{\hbar} \sim \frac{\tau_{e-ph}\varepsilon_F}{\hbar}\frac{s}{\nu_F} \sim 1 \quad .$$

In this estimation the values of τ_{e-ph} from Fig. 4.6 were taken. One can see that

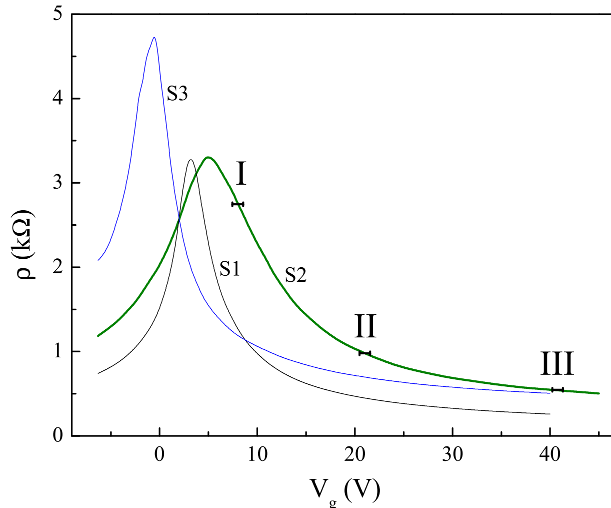

Figure 4.7: The gate voltage dependence of the resistivity measured at 5.4 K for three studied samples S1, S2 and S3. The EEI correction to the conductivity is studied in regions I, II and III.

the electron phase changes by an amount of the order of unity, which means that during the time τ_{e-ph} electrons lose their coherence, i.e. $\tau_{e-ph} = \tau_{\varphi}$.

In summary, we show that electron antilocalisation in graphene, a consequence of the Berry phase π, can be realised experimentally. This occurs when the dephasing time is small compared with the elastic inter- and intra-valley scattering times. We also demonstrate that quantum interference in graphene can exist at very high temperature due to suppressed electron-phonon scattering.

4.3 Electron-electron interaction

The weak localisation correction to the conductivity also contributes to the temperature dependence of the conductivity at zero magnetic field. In addition, there is another correction coming from electron-electron interaction in the presence of disorder. Since the two quantum corrections depend logarithmically on temperature, in order to study the electron-electron interaction correction to σ_0 it is necessary to separate the two.

We study several samples with different levels of disorder (Table 4.2), which is indicated by the electron mobilities, in a temperature range 0.25 – 40 K. We focus on the same carrier densities as in the studies of magnetoconductivity (see the previous section): regions I, II and III (Fig. 4.7).

First, the resistivity ρ is measured as a function of the gate voltage at all studied temperatures. Each studied region of the carrier density (gate voltage) is chosen with respect to the NP (Fig. 4.1). At low T in each region ρ is averaged over a small range of the gate voltages ΔV_g to reduce the effect of the UCF and noise. The range ΔV_g is different in regions I, II and III and is chosen in such a way that ρ is linear within ΔV_g. This range varies from sample to sample, because of the different level of disorder, which affects the shape of the $\rho(V_g)$ curves (e.g. the curves can be narrower or wider). Apart from that, the dependence of the resistivity on the gate voltage is different if long-range or short-range impurities are the dominant scatterers [9, 98]. In the current experiment in region I $\Delta V_g = 0.5$ V, in region II $\Delta V_g =$ 1-3 V and in region III $\Delta V_g =$ 3-6 V (at high carrier densities a range of gate voltages is given because the three samples have different levels of disorder, as can be seen in Fig. 4.7).

As an example, the resistivity measured in region II at different temperatures in a small range of gate voltages is shown in Fig. 4.8(a). One can see that at low temperatures, due to the presence of the UCF and noise, ρ should be averaged over the shown window of V_g. At high T this procedure is not necessary. The result of averaging in each region at different temperatures is shown in Fig. 4.8(b-d). Note that at high temperatures the position of the NP can fluctuate at different T by a small amount of 0-0.5 V (Fig. 4.9(b)). A simple check shows that the position of the NP should be determined accurately ($\delta V_g = 0.03 - 0.05$ V), because an error of 0.1 V leads to large errors in the temperature dependence of the resistivity. The best (reproducible) results are achieved when parts of the $\rho(V_g)$ curves near the NP are fitted with a Gaussian function (Fig. 4.9(a)). Usually the parts of the curves between ρ_{NP} and $0.5 - 0.8\rho_{NP}$ (where ρ_{NP} is the resistivity at the NP) are fitted,

Table 4.2: Electron mobility μ (in cm^{2}V^{-1}s^{-1}) at 5 K for three regions of the carrier density in samples S1, S2 and S3. Characteristic scattering times τ_i and τ_* (in ps) are also shown for sample S1.

	S1			S2	S3
Region	μ	τ_i	τ_*	μ	μ
I	17500	14	0.45	9300	12500
II	11500	3	0.3	5400	11000
III	9700	1	0.35	4500	9500

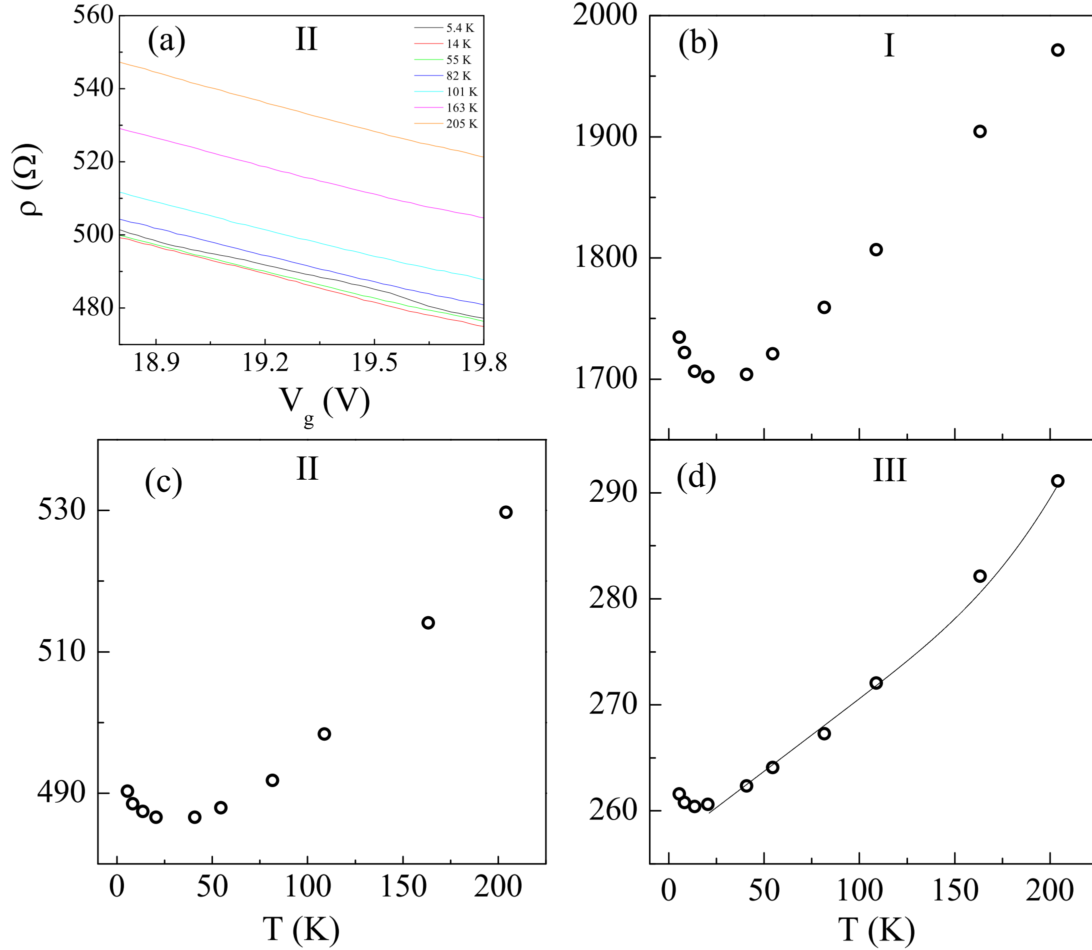

Figure 4.8: (a) The gate voltage dependence of the resistivity of sample S1 in region II at different temperatures. (b)-(d) The resistivity as a function of temperature for sample S1 for the three studied regions. The solid line in (d) is a fit to equation (2.51). The fit gives $D_a = 18$ eV.

and the position of the NP as well as the value of ρ_{NP} (if necessary) are determined. It is important that the same parts of the curves are fitted at all temperatures and magnetic fields. For example, if the lower fitting border is $0.5\rho_{NP}$, then only this border should be used while a sample is being measured. In the next chapter we will see that at temperatures between 20 mK and 4.2 K the NP is stable and there is no need to determine its position at each temperature using the Gaussian function.

One can see from Fig. 4.8(a) that at low T the resistivity decreases as the temperature increases. At high T the resistivity increases. There are several contributions to ρ that give such a dependence. At low temperatures the quantum corrections dominate: the WL and EEI corrections lead to a logarithmically decreasing resistivity. The WAL correction leads to the increase of ρ. At high temperatures

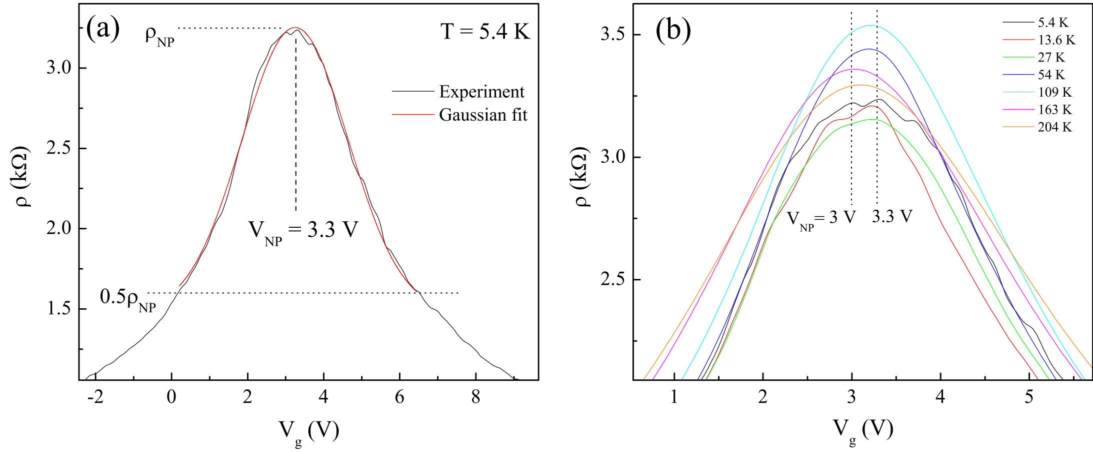

Figure 4.9: (a) Determination of the position, V_{NP}, of the neutrality point and its resistivity, ρ_{NP}. The upper half of the $\rho(V_g)$ curve is fitted with a Gaussian function. This function is then used to determine V_{NP} and ρ_{NP}. (b) Fluctuations of the NP at different temperatures: $V_{NP} = 3 - 3.3$ V.

electron-phonon interaction gives the main contribution to ρ. The figure shows that at these temperatures the experimental dependence is not linear, suggesting that apart from the linearly-dependent electron-acoustic phonon contribution, there is a contribution from other types of phonons, mainly coming from the substrate [57]. And finally, the temperature independent contribution, which arises from electron scattering off impurities, gives a T-independent offset of the experimental dependence of $\rho(T)$.

We will limit the studied temperature range to 50 K in order not to take into account optical phonons from the substrate. However, at 20-50 K acoustic phonons are significant and have to be dealt with. Therefore, before we start investigating the quantum corrections, we determine the electron-acoustic phonon contribution to ρ and subtract [49] it.

4.3.1 Effect of electron-phonon interaction

As we know from the previous section, at high carrier densities positive MC is observed (no antilocalisation) and the quantum interference survives at lower temperatures than at low carrier densities. Thus, at high carrier densities and high temperatures the dominant contribution to $\rho(T)$ is due to electron-phonon interaction, ρ_{e-ph}. Due to the linear dispersion relation, this contribution is independent of

n [52, 53]. Therefore, we determine ρ_{e-ph} in region III and subtract it in all studied regions of carrier density.

Since at $T > 100$ K optical phonons from the substrate also contribute to $\rho(T)$, we fit the experimental temperature dependence of the resistivity to the sum of two contributions [57]: acoustic phonons in graphene and optical phonons in silica, equation (2.51). This equation has only one fitting parameter, the deformation potential D_a. The fitting procedure (Fig. 4.8(d)) gives $D_a = 18 \pm 1$ eV. Using this value of D_a we can determine the acoustic phonon contribution to $\rho(T)$ using equation (2.48) and subtract it.

Figure 4.10(a) shows the $\rho(T)$ dependence and the electron-acoustic phonon contribution on the same graph for the three studied regions. The result of subtraction is shown in Fig. 4.10(b) as $\Delta\sigma(T) = \sigma(T) - \sigma(T_0)$, where T_0 is the lowest studied temperature, $\sigma(T) = [\rho(T)$ - $\rho_A(T)]^{-1}$.

4.3.2 Separation of the quantum corrections

In order to separate the quantum corrections, we combine the measurements of magnetoconductivity with those of the temperature dependence of the conductivity. The separation is performed using two methods. In the first method, used to analyse the results of samples S1 and S3, the low-field perpendicular magnetoconductivity has been measured in order to determine the characteristic times responsible for WL: the inelastic dephasing time $\tau_\varphi(T)$, the elastic time of inter-valley scattering τ_i, and the elastic time τ_* which describes intra-valley suppression of quantum interference. This analysis is done using the theoretical model (equation (2.27)) following the method described in the previous section and [34, 97]. These times are used to determine the WL correction, equation (2.41), which is then subtracted.

In the second method, used to analyse sample S2, the EEI correction has been isolated by suppressing WL by a perpendicular magnetic field of 1 T. As will be seen later this magnetic field is large enough to suppress interference without affecting the EEI correction [11]. Both methods lead to close results for the magnitude of the EEI correction in the studied samples, which proves the robustness of the first method based on equation (2.27).

In Fig. 4.10(b) the solid lines show the WL correction determined using the first

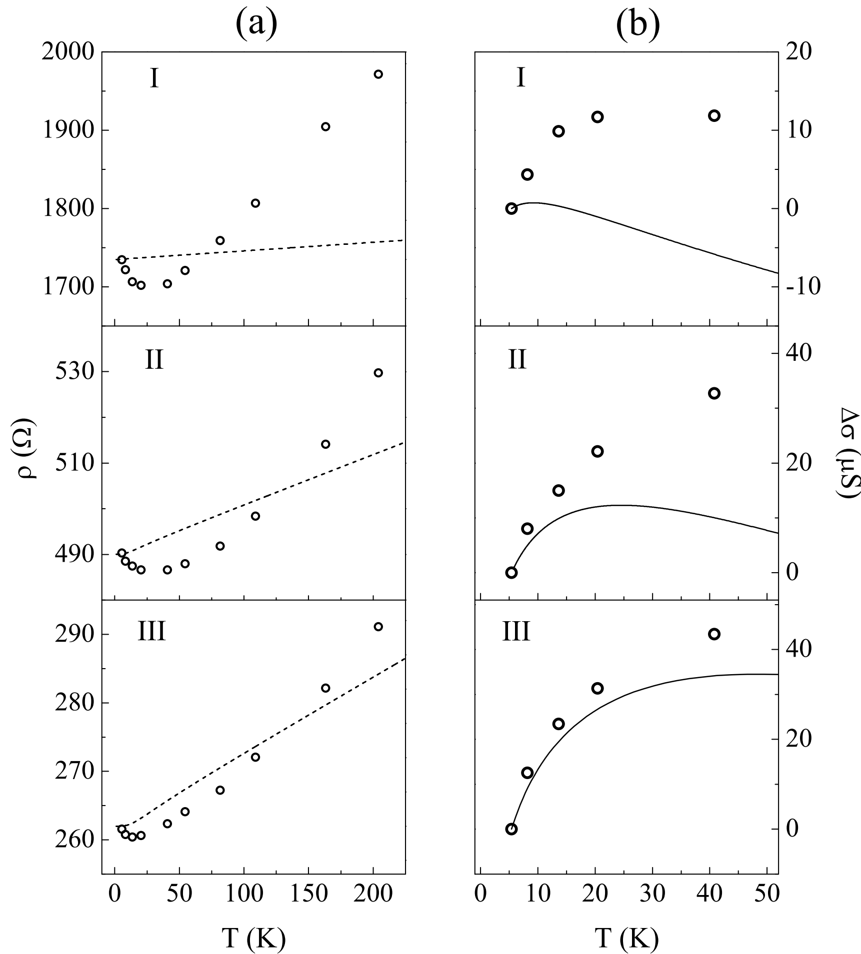

Figure 4.10: (a) Resistivity as a function of temperature for sample S1 in the three studied regions (see Fig. 4.8). The dashed line indicates the contribution from electron-acoustic phonon interaction calculated using equation (2.48) (shifted for convenience) with $D_a = 18$ eV. (b) The conductivity after the phonon contribution has been subtracted. The solid lines show the WL correction to the conductivity.

method. One can see that the two types of quantum correction, WL and EEI, are of similar magnitude. The solid lines clearly show that in regions I and II there is a transition from weak localisation, an increase of $\Delta\sigma(T)$, to antilocalisation, a decrease of $\Delta\sigma(T)$. (Earlier, such a transition was detected in the change of the sign of magnetoconductivity (see the previous section and [97]), with the transition temperatures of $\sim$ 10 K in region I and $\sim$ 25 K in region II, which is in agreement with this experiment.)

Figure 4.11(a) shows the temperature dependence of the resistivity in sample S2 in the temperature range 0.25 - 40 K. The dashed line shows the electron-phonon contribution with a deformation potential of 18 eV. This contribution, equation

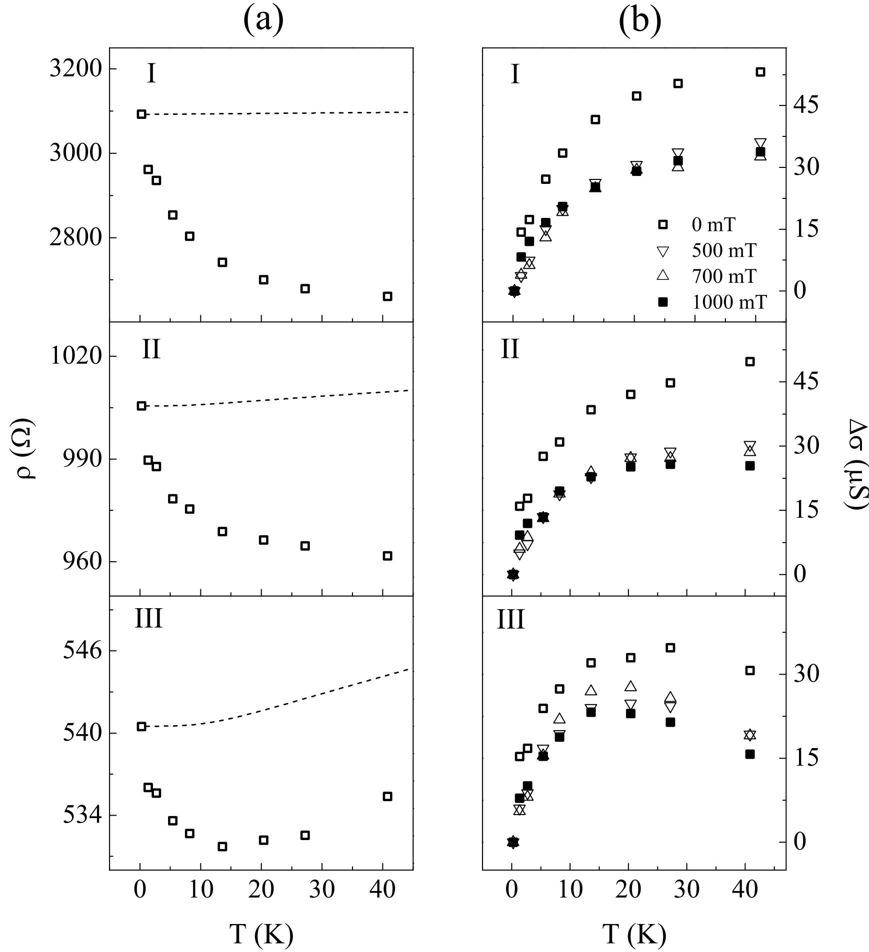

Figure 4.11: (a) Resistivity as a function of temperature for sample S2, shown for three regions. The dashed lines indicate the magnitude of the acoustic phonon contribution calculated using equation (2.48) (shifted for convenience) with $D_a = 18$ eV. (b) The conductivity $\Delta\sigma(T) = \sigma(T) - \sigma(T_0)$ at different magnetic fields (the contribution of acoustic phonons with $D_a = 18$ eV has been subtracted).

(2.48), is subtracted in regions II and III. The remaining quantum correction to the conductivity is presented in Fig. 4.11(b), for different magnetic fields. One can see that with increasing B there is a decrease in the slope of the temperature dependence until a saturation is reached. This is a signature that the WL correction has been suppressed.

As we discussed in Chapter 2, the suppression of the WL correction is expected at magnetic fields much larger than the transport magnetic field, B_{tr}. For sample S2, B_{tr} are 120, 70 and 45 mT for regions I, II and III, respectively. Therefore, it is not surprising that 1 T is enough to suppress WL. It is also important to make sure that this magnetic field does not affect the EEI correction due to the Zeeman splitting. The condition $g^*\mu_B B > k_B T$ is fulfilled at magnetic fields higher than

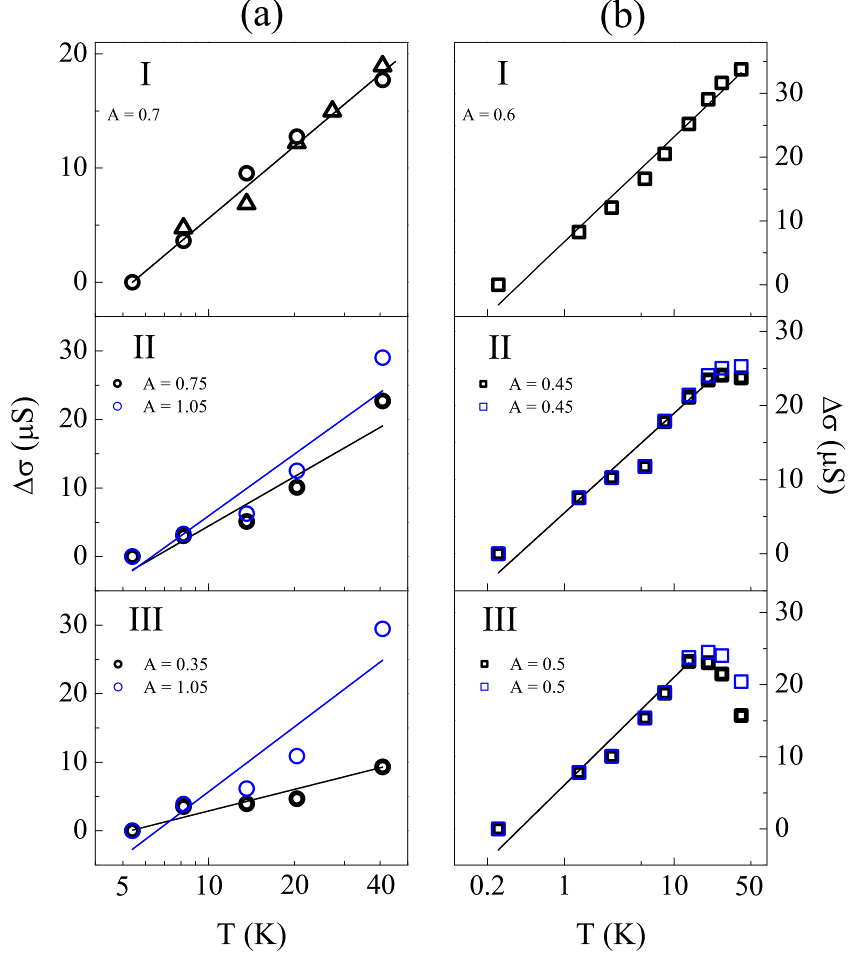

Figure 4.12: The electron-electron interaction correction to the conductivity. (a) The results for sample S1 (circles) are obtained by determining the WL correction using equation (2.27) (in region I the results for sample S3 are also displayed by triangles). (b) For sample S2 the WL contribution is suppressed by magnetic field. Solid lines are fits to equation (2.31). Black and blue colors correspond to the subtraction of equation (2.48) with $D_a = 18$ and 21 eV, respectively.

1 T, therefore the range of applied fields to suppress WL does not affect the EEI correction.

Figures 4.10(a) and 4.11(a) show that the relative magnitude of the phonon contribution depends both on the carrier density and sample quality (mobility). In region I, for all studied samples, this accounts for less than 5% of the change in $\rho(T)$ for temperatures below 50 K and the subtraction procedure is not necessary. In region III, where the carrier density is high and the resistivity is low, the phonon contribution is important and the value of the electron-electron interaction correction becomes sensitive to the choice of D_a. In region II it is significant in the

high-mobility sample S1 and less important in the low-mobility sample S2.

The result of the separation of the EEI correction using the two methods is shown in Fig. 4.12, where the interaction correction is also shown for sample S3 in region I. To check how the EEI correction is affected by the phonon contribution, we also subtract the phonon contribution with $D_a = 21$ eV. The two sets of points in each graph in Fig. 4.12 correspond to different values of the deformation potential, 18 and 21 eV. One can see that at low carrier density (region I) in sample S1 and all densities in sample S2 the uncertainty in the coefficient A is negligibly small. Since the mobility of electrons in sample S1 is larger than that in sample S2 (see Table 4.2) the effect of phonons is weaker in S2. That is why the results under mentioned conditions are stable for different values of D_a. Thus, in low-mobility samples, where the effects of phonons are very small, the error in determining the EEI correction is minimal. The figure also shows that the EEI correction is indeed logarithmic in temperature as expected. The coefficient A is 0.6 ± 0.15 for the majority of regions of the carrier densities in the studied samples.

To interpret the obtained value of A, we note that the theory [40] distinguishes between the contributions from different quantum states of two interacting electrons, commonly referred to as 'channels'. The coefficient A takes the form $A = 1 + c\,(1 - \ln(1 + F_0^\sigma)/F_0^\sigma)$, where F_0^σ is the Fermi-liquid constant. While the first term in this relation represents the universal contribution of the 'singlet' channel, the second (Hartree) term describes the contributions of c 'triplet' channels. For example, in a single-valley 2D system (such as in GaAs) the coefficient $c = 3$ due to identical contributions of three spin triplet states. (When this degeneracy is lifted by a magnetic field [40], the two components become suppressed, resulting in $c = 1$.)

In two-valley 2D systems (e.g., in Si-MOSFETs [106, 107]) the situation is more complicated. In the absence of inter-valley scattering, the valley index $v = \pm$ is a good quantum number. In this case the overall number of channels is 16, due to four-fold spin degeneracy of two interacting electrons and an additional four-fold degeneracy due to the two valleys. This gives the prefactor $c = 15$. This result also holds if the inter-valley scattering is weak, $k_B T \gg \hbar/\tau_i$, i.e. when the typical electron energy is larger than the characteristic rate of inter-valley scattering. However, at low temperatures, $k_B T \ll \hbar/\tau_i$, strong inter-valley scattering mixes the valleys and A takes the same form as in the single-valley case.

Unlike in Si-MOSFETs, in graphene the valley dynamics is governed by two characteristic times, the inter-valley scattering time τ_i and intra-valley dephasing time τ_* [13]. In our experiments, the inter-valley scattering rate $\hbar/\tau_i$ is of the order of 3 K, while the intra-valley dephasing rate is above 20 K (see Table 4.2). Thus the intermediate regime, $\hbar/\tau_i < k_B T < \hbar/\tau_*$, becomes possible. In this case, the channels with two electrons from different valleys give no contribution. (This situation is similar to the one that occurs for universal conductance fluctuations in graphene [108,109].) As there are two spin states per electron and two states for two electrons in the same valley, there are eight remaining channels, one of which is both spin and valley singlet, so that $c = 7$. Thus we arrive at the following expression for A in equation (2.31):

$$A(F_0^\sigma) = 1 + 7\left(1 - \ln(1 + F_0^\sigma)/F_0^\sigma\right) \ . \tag{4.4}$$

This analysis is confirmed by standard diagrammatic calculations [101], where a common assumption was used that all channels except for the singlet are described by the same Fermi-liquid parameter.

Using equation (4.4) and the experimental values of A, Fig. 4.12, we find the values of F_0^σ to be between -0.07 and -0.14. It is interesting to note that the value of F_0^σ found in GaAs and Si systems at $r_s \sim 1$ is between -0.15 and -0.2 [49, 106, 107]. In Chapter 2 it was shown that the Fermi-liquid constant is smaller in graphene compared to other 2D-systems due to the chirality of charge carriers. The theory predicts $F_0^\sigma = -0.10$, which is in agreement with our measurements. Our result is in agreement with the value of F_0^a in [46] for the studied range of charge densities. (To compare F_0^σ with F_0^a in [46], one has to take into account that these quantities are related as $F_0^a = 2F_0^\sigma$.)

In summary, we show that electron-electron interaction plays an important role in the low-temperature conductivity of carriers in graphene. Unexpectedly for the EEI correction, its magnitude is affected by the intra-valley decoherence rate due to elastic scattering. We find the value of the interaction parameter F_0^σ in graphene, which is lower than in other 2D systems studied previously.

Chapter 5

Quantum corrections to the conductivity at low temperatures

In the previous chapter we studied the quantum corrections to the conductivity at temperatures between 5 and 200 K. We observed a transition from weak localisation to antilocalisation as a function of temperature and carrier density. The quantum interference in graphene was found to survive at temperatures up to 200 K due to weak electron-phonon interaction. The electron-electron interaction correction was shown to depend logarithmically on temperature (as predicted by theory) and to be affected by elastic scattering. Due to the chirality of charge carriers the Fermi-liquid parameter F_0^σ was found to be smaller in graphene compared to conventional 2D-systems.

In this chapter we study the quantum corrections between 20 mK and 5 K. In the magnetoconductivity measurements we observe a saturation of the dephasing length below 100 mK. We discuss the possible mechanisms responsible for such a saturation and focus on the spin-orbit interaction and spin-flip processes by resonant scatterers. We determine the spin coherence length and find its values to be much smaller than theory predicts. We also demonstrate how this length can be tuned by controlling the level of disorder.

5.1 Weak localisation

In Chapter 4 we described one method of measurements of WL: the magnetic field was fixed and the conductivity was measured in a narrow window of gate voltages,

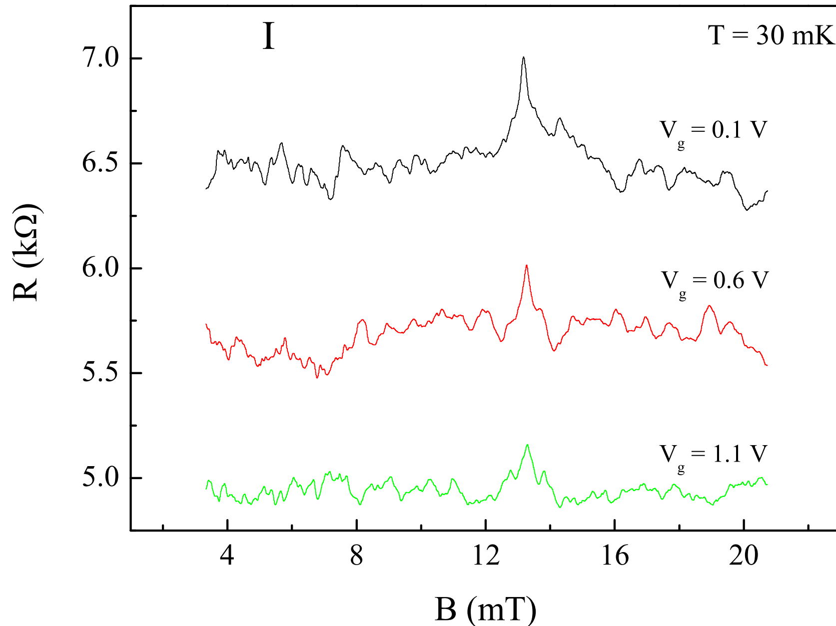

Figure 5.1: The resistance measured in sample SS1 as a function of magnetic field shown for region I at 30 mK. Three curves correspond to three close values of the gate voltage.

over which σ was averaged. The magnetic field was then changed by a few milli Tesla and the measurements were repeated.

Here we show a slightly different approach. The resistance, $R(B)$, is measured as the magnetic field is varied over a range of 20 mT at a fixed gate voltage. This measurement is then repeated at three close values of V_g (Fig. 5.1) and $R(B)$ is averaged. At very low temperatures, $\sim$20 mK, the dephasing length is expected to be very large. Therefore, the WL peak in the MC is very narrow. In order to resolve the peak one has to sweep the magnetic field very slowly. Therefore we limit the values of V_g, over which the averaging is performed, to three. This is enough to reduce the effect of the UCF by $1/\sqrt{3}$. The slight asymmetry in the $R(B)$ curves is eliminated as described in the previous chapter and the result is converted to the magnetoconductivity (MC), $\Delta\sigma(B)$.

We study three different samples of different size and disorder (see Table 5.1). Since samples SS1 and SS2 are large, the UCF at 20 mK are not expected to be very large. Sample SS3 was measured at a higher temperature at which the UCF were also small.

The MC measurements are performed at carrier densities marked by red circles in Fig. 5.2(a). The temperature dependence of the conductivity is measured in regions

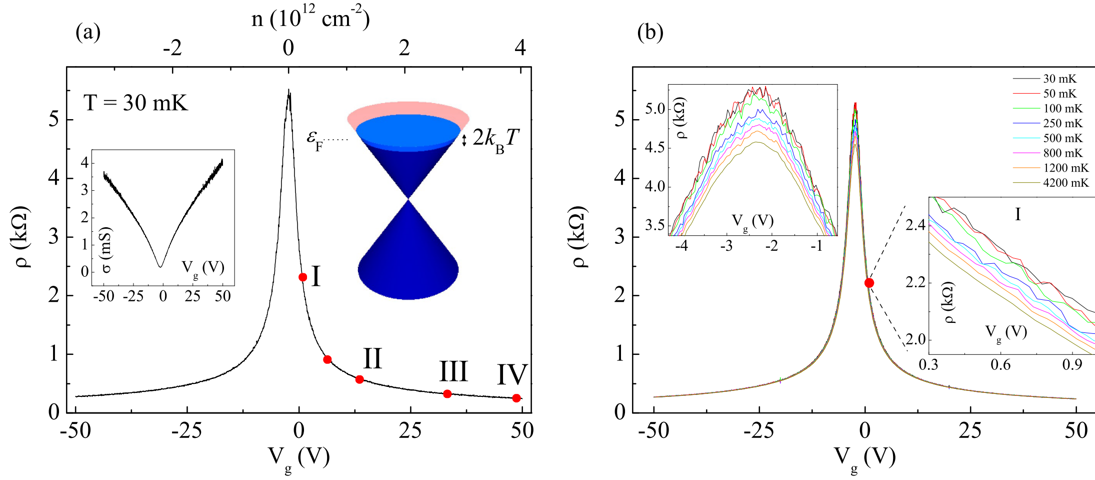

Figure 5.2: (a) The resistivity dependence on the gate voltage, RV_g, measured at 30 mK in sample SS1. Red circles represent regions where magnetoconductivity is measured. The temperature dependence of the conductivity is measured in regions I, II and III. The left inset shows the gate voltage dependence of the conductivity for the same sample at 30 mK. The right inset shows the valence and conduction bands filled with electrons up to the Fermi energy, ε_F, which is much larger than k_BT in all studied regions. (b) The RV_g curves measured in a temperature range 20 mK - 4.2 K. The left inset shows a zoomed-in region near the neutrality point. The right inset shows the resistivity in a narrow range of the gate voltages in region I.

I, II and III. At all carrier densities the studied system of electrons is degenerate, as could be deduced from the fact that the Fermi energy is much larger than k_BT.

Figure 5.3 shows the MC curves measured at different temperatures. One can see positive MC at all T, which is indicative of the weak localisation correction to the conductivity. Analysis of WL is performed using the standard theoretical model [13]:

$$\frac{\pi h}{e^2} \cdot \Delta\sigma(B) = F\left(\frac{\tau_B^{-1}}{\tau_{\varphi s}^{-1}}\right) - F\left(\frac{\tau_B^{-1}}{\tau_{\varphi s}^{-1} + 2\tau_i^{-1}}\right) - 2F\left(\frac{\tau_B^{-1}}{\tau_{\varphi s}^{-1} + \tau_i^{-1} + \tau_*^{-1}}\right) . \quad (5.1)$$

Table 5.1: Sample parameters: dimensions (in μm) of the samples and mobilities μ (in cm^{2}V^{-1}s^{-1}) in regions I, II and III.

Sample	L×W	μ_I	μ_{II}	μ_{III}
SS1	40.6×17.5	13400	9800	7700
SS2	15×7	5300	4700	4200
SS3	4×1	4100	2000	1300

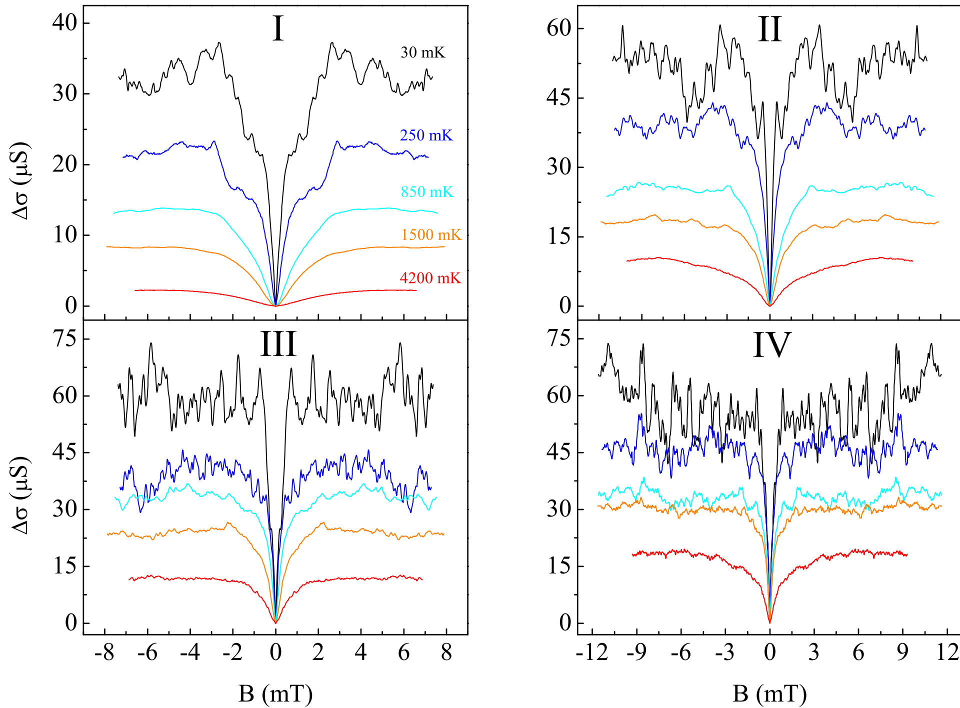

Figure 5.3: Magnetoconductivity measured in regions I, II, III and IV at different temperatures.

Here $\tau_{\varphi s}^{-1} = \tau_{\varphi}^{-1} + \tau_{s}^{-1}$, τ_{φ} and τ_s are the electron dephasing and spin coherence times.

Analysis of the MC curves is performed similarly to that at high temperatures: equation (5.1) is used to fit the experimental dependences and extract the three characteristic lengths: $L_{\varphi s}, L_i$ and L_*. As in the previous studies of WL, in this experiment we obtained $L_i \sim 1\ \mu$m and $L_* \ll 1\ \mu$m.

5.1.1 Temperature dependence of the dephasing length

The temperature dependence of the dephasing length is shown in Fig. 5.4 for three regions. One can see that above $\sim$ 1K the dephasing length, $L_{\varphi s} = \sqrt{D\tau_{\varphi s}}$, decreases as the temperature increases and agrees with the theory of dephasing due to electron-electron interaction in the diffusive regime [21]:

$$\tau_{\varphi}^{-1} = \alpha \frac{k_B T}{2\varepsilon_F \tau_p} \ln\left(\frac{2\varepsilon_F \tau_p}{\hbar}\right) . \tag{5.2}$$

This regime corresponds to the condition $k_B T \tau_p/\hbar < 1$, which is always fulfilled under the studied experimental conditions. We use equation (5.2) to fit the exper-

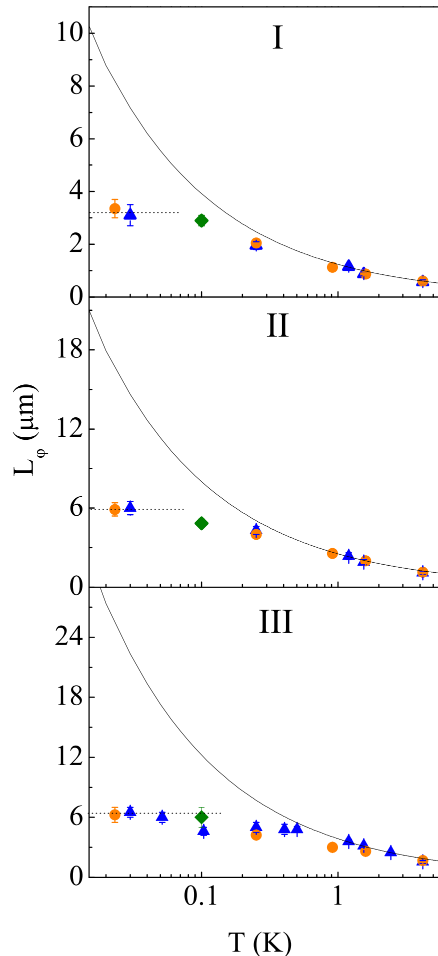

Figure 5.4: The temperature dependence of the dephasing length in sample SS1 extracted from MC in regions I, II and III. Different symbols represent different experimental runs. The dotted line shows the saturated value of $L_{\varphi s}$. Solid curve is the expected behavior of the dephasing length due to electron-electron interaction. Error bars at each temperature indicate values of $L_{\varphi s}$, which can be used to fit the MC curves.

imental temperature dependence of $L_{\varphi s}(T)$ at $T > 1$ K to find α, which is of the order of unity (in agreement with the theory) at all carrier densities.

At temperatures below 1 K the experimental values of the dephasing length deviate from theory and eventually saturate. The value of the saturated $L_{\varphi s}$ increases with carrier density (Fig. 5.4).

5.1.2 Mechanisms of the saturation of the dephasing length

This saturation results from the temperature-independent contribution to $L_{\varphi \mathrm{s}}(T)$ related to the electron spin. However, before we can draw this conclusion there are three other mechanisms that could be responsible for such a saturation [60] that we

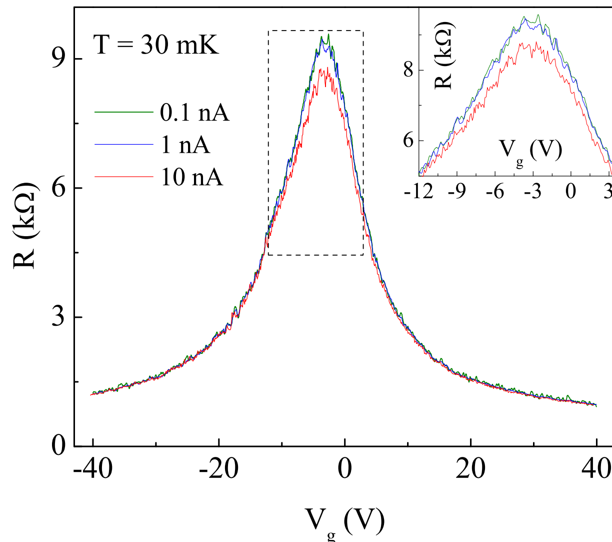

Figure 5.5: The resistance dependences on the gate voltage measured at 30 mK in sample SS2 for different source–drain currents show the absence of electron overheating for 1 and 0.1 nA (this is true also for sample SS1). The inset is a zoomed-in region shown in the main graph by a rectangle.

need to take into account: (i) sample size [34], (ii) electron overheating [99], and (iii) magnetic impurities [110].

(i) Dephasing of electrons can occur in the source and drain contacts of the sample, and therefore the maximum possible dephasing length is the sample length, L. Since the saturated value of the dephasing length $L_{\varphi s}^{sat} \ll L$ this mechanism can be dismissed.

(ii) Measurements performed at different source–drain currents show that 1 nA does not cause overheating. For example, in Fig. 5.5 the resistance measured as a function of the gate voltage increases as the current is decreased from 10 nA to 1 nA and then saturates for smaller currents [99]: there is no difference in passing 1 or 0.1 nA through the samples. Therefore, 1 nA is low enough not to cause overheating. Moreover, as we will see in the next section the conductivity decreases logarithmically as a function of temperature down to 20 mK (see Fig. 5.6). Both facts prove that there is no electron overheating and the applied current can be ruled out as a source of dephasing.

(iii) As far as magnetic impurities are concerned, the three studied samples were fabricated from different sources of natural graphite. All of them have different level of disorder, which can be seen from the electron mobilities (see the table in Fig. 1).

As we will see later, the values of the saturated dephasing length, $L_{\varphi s}^{sat}$, extracted in these samples are systematic and all lie along the same line in Fig. 5.10. If magnetic impurities were responsible for the saturation, then their concentration would vary randomly from sample to sample and one would expect random values of $L_{\varphi s}^{sat}$. Therefore, the observed saturation of the dephasing length can not be caused by magnetic impurities [60].

Between the experimental runs, sample SS1 was thermally cycled to room temperature and back to the base temperature a few times. The cycles caused only a very small shift ($\sim 5\%$) of the Dirac point. If there were impurities that could cause electron dephasing, then their amount and distribution along the sample would change over the thermal cycles. This, in turn, would lead to a noticeable shift of the Dirac point, because graphene was shown to be sensitive even to single molecules [111]. In this case, values of $L_{\varphi s}$ measured in different experimental runs would not be in agreement with each other. High stability of the Dirac point and good agreement between the runs means that there are no such impurities.

Thus, the only origin of the saturation is related to the electron spin and the values of $L_{\varphi s}^{sat}$ are the values of L_s. We consider two spin-related phenomena: spin-orbit interaction and spin-flip scattering by resonant localised states in the vicinity of the Dirac point.

5.2 Temperature dependence of the conductivity

The weak localisation correction also manifests itself in the temperature dependence of the conductivity, $\sigma(T)$, at zero magnetic field, which is measured similarly to the high-T conductivity (Chapter 4). The resistivity is measured as a function of the gate voltage at different temperatures, 20 mK - 4.2 K, Fig. 5.2(b), which is then averaged over a small range of V_g in each of the three regions (I, II and III). The averaging is more important at low temperatures due to the presence of the UCF and noise (right inset in Fig. 5.2(b)). The resultant resistivity is converted to the conductivity and plotted as $\Delta\sigma = \sigma(T) - \sigma(T_0)$, where $\sigma(T) = 1/\rho(T)$ and T_0 is the lowest studied temperature. At low temperatures the position of the NP in the $\rho(V_g)$ curves is stable as can be seen from Fig. 5.2(b) (left inset), therefore there is no need to determine it at each temperature. The result of averaging is plotted in

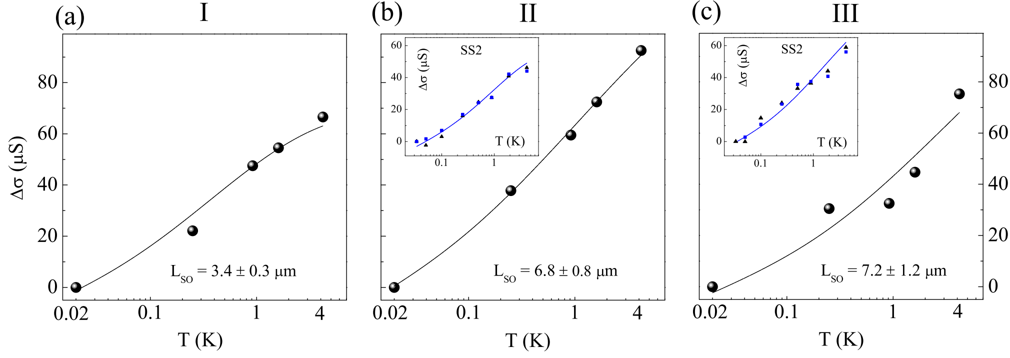

Figure 5.6: The temperature dependences of the conductivity, $\Delta\sigma(T) = \sigma(T) - \sigma(T_0)$, where T_0 is the lowest studied temperature. The dependences in the main graphs are shown for sample SS1 for (a) region I, (b) region II and (c) region III. Insets show $\Delta\sigma(T)$ in sample SS2. The solid curves are fits to equation (5.3). The values of the spin coherence lengths in each region are shown for sample SS1. Different symbols in the insets correspond to different experimental runs.

Fig. 5.6.

In addition to the WL correction, there is also the EEI correction:

$$\Delta\sigma = \delta\sigma^{\mathrm{WL}} + \delta\sigma^{\mathrm{EEI}} \; . \tag{5.3}$$

Only $\delta\sigma^{\mathrm{WL}}$ contains information about SOI and spin-flip scattering by vacancies, so we measure the EEI correction explicitly by two independent methods: by studying the temperature dependence of the Hall coefficient, and suppressing WL by a perpendicular magnetic field. These measurements were used to determine the value of A which we found to be $A = 0.5 - 0.6$ (see subsection 5.2.1) in agreement with earlier studies [101].

The WL correction to the conductivity is given by the following relation:

$$\delta\sigma^{\mathrm{WL}} = -\frac{e^2}{2\pi^2\hbar}\left[\ln\left(1 + \frac{2\tau_\varphi}{\tau_i} + \frac{\tau_\varphi}{\tau_s}\right) - \ln\left(1 + \frac{\tau_\varphi}{\tau_s}\right) - 2\ln\left(\frac{\tau_\varphi/\tau_p}{1 + \tau_\varphi/\tau_i + \tau_\varphi/\tau_* + \tau_\varphi/\tau_s}\right)\right] \; . \tag{5.4}$$

Figure 5.6 shows the temperature dependence of the conductivity of two samples. The conductivity, $\Delta\sigma(T) = \sigma(T) - \sigma(T_0) = 1/\rho(T) - 1/\rho(T_0)$, where T_0 is the lowest studied temperature, decreases logarithmically down to 20 mK. The dependences are fitted by equation (5.3). From the MC analysis we determine the inter-valley

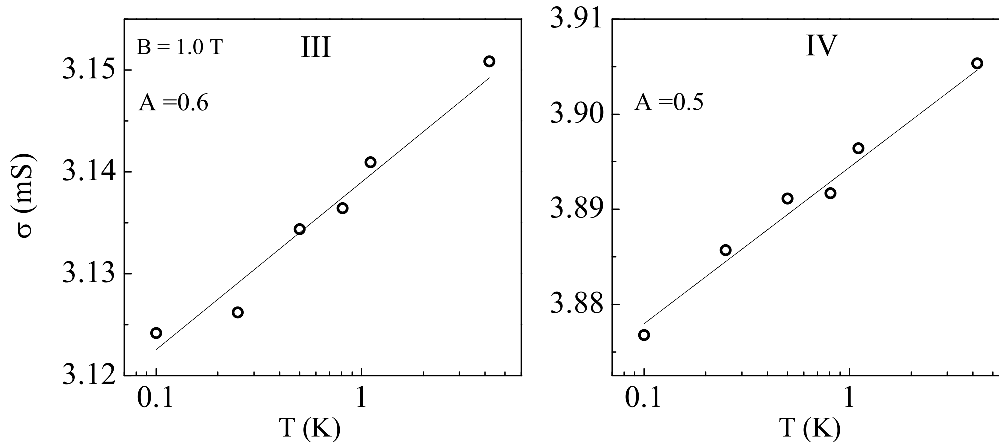

Figure 5.7: The EEI correction to the conductivity isolated by applying a perpendicular magnetic field of 1 T. The left- and right-hand side graphs correspond to regions III and IV.

and intra-valley scattering lengths. Since $L_i \sim 1\ \mu$m and $L_* \ll 1\ \mu$m, and both are much smaller than L_φ, they have a negligible effect on the form of $\sigma(T)$. The values of L_φ at temperatures below 1 K are calculated using equation (5.2), where the prefactor α is determined from the higher temperature ($T > 1$ K) dependence of $L_{\varphi s}^{\text{sat}}$, Fig. 5.4. Since the EEI correction is determined separately, the spin coherence length, L_{s}, is the only fitting parameter in equation (5.3). The result of fitting is shown for samples SS1 and SS2 in Fig. 5.6.

5.2.1 Electron-electron interaction correction

We isolate the EEI correction to the conductivity by suppressing WL in a perpendicular magnetic field and by studying the temperature dependence of the Hall coefficient. The suppression of WL by a magnetic field is done in the same way as in Chapter 4. A magnetic field of 1 T was enough to isolate the EEI correction (Fig. 5.7).

Figure 5.8 shows the studies of the Hall coefficient, R_H, in graphene. In order to determine the EEI correction from R_H, one has to know the Drude conductivity σ_0 and the classical Hall coefficient R_H^0 (see equation (2.46)). We determine σ_0 by measuring the longitudinal resistivity as a function of the magnetic field at temperatures 0.11, 1.8 and 4.2 K (Fig. 5.8(a)). The figure shows three curves crossing each other at $B = 0.75$ T. The correspondent resistivity is $\rho_{xx} = 2.27$ kΩ. The expected

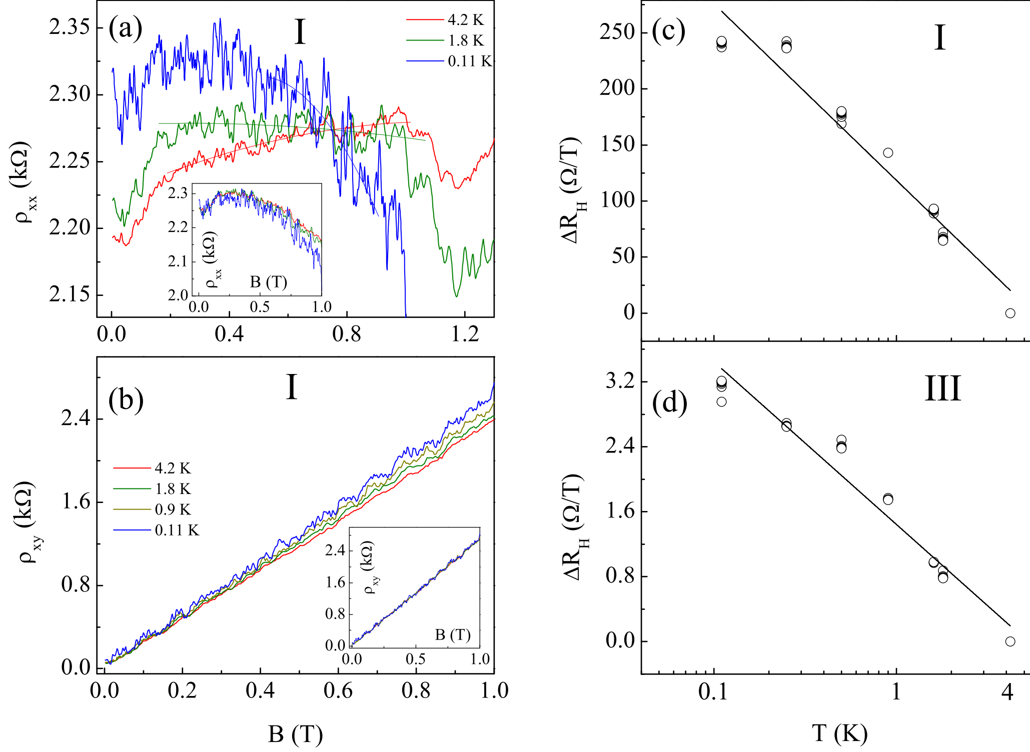

Figure 5.8: (a) The longitudinal magnetoresistivity measured in region I at different temperatures. Fitting solid curves are used to determine the resistivity at the crossing point. The inset shows the same curves after the EEI correction has been subtracted. (b) The transverse magnetoresistivity at different temperatures. The group of lines in the main graph corresponds to raw data and that in the inset shows ρ_{xy} without the EEI correction. (c-d) The temperature dependences of the Hall coefficient shown for regions I and III. The solid lines are linear fits. Different points at each temperature correspond to different magnetic fields.

value of the magnetic field at the crossing point is $B_0 = 1/1.34 \approx 0.75$ T. The found value of ρ_{xx} is used to calculated the Drude conductivity $\sigma_0 = 1/\rho_{xx}$.

The classical value of the Hall coefficient is given by the relation $R_H^0 = 1/ne$. The carrier density, n, is determined from the Shubnikov-de Haas oscillations (Chapter 3). The proportionality coefficient between the carrier density and the gate voltage is found to be $\gamma = 7.7 \times 10^{10}$ V^{-1} ($n = \gamma V_g$ cm^{-2}).

The Hall coefficient is determined from the slope of the transverse magnetoresistivity: $R_H = \rho_{xy}/B$. The group of curves in the main graph in Fig. 5.8(b) shows $\rho_{xy}(B)$ at different temperatures. The curves are fitted with a straight line and the ratio ρ_{xy}/B is calculated at different B. The temperature dependence of the Hall coefficient is shown in Fig. 5.8(c-d) for regions I and III. The slope of this dependence gives the EEI correction (equation (2.46)), Fig. 5.9. The values of A

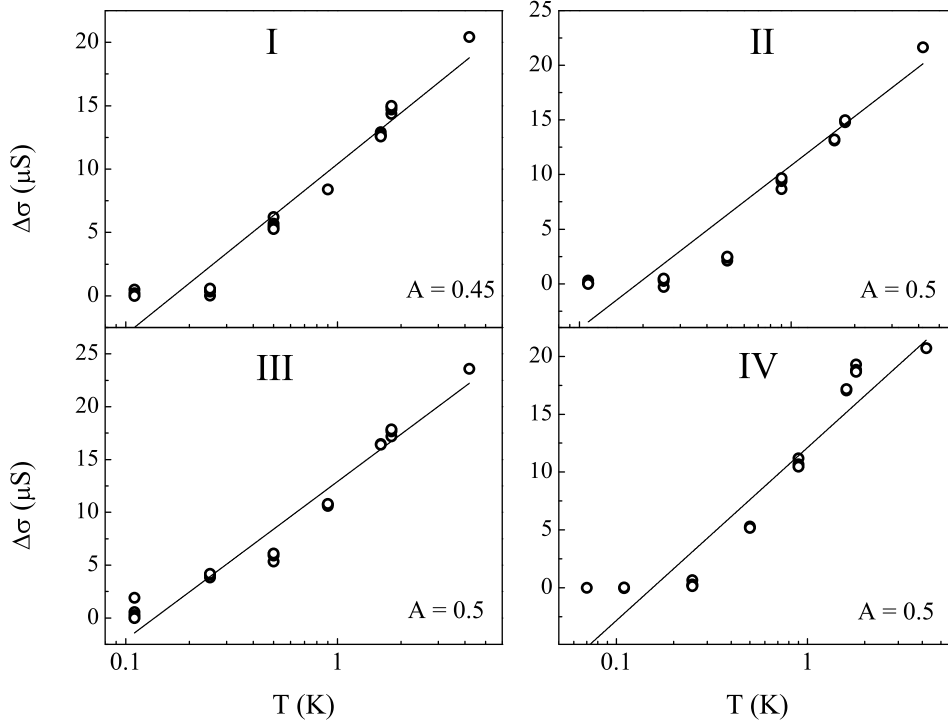

Figure 5.9: The EEI correction to the conductivity determined from the temperature dependence of the Hall coefficient for regions I-IV.

determined from the two methods are in agreement with each other.

The EEI correction determined from the Hall coefficient studies is then subtracted from σ_{xx} and the longitudinal and transverse resistivities are recalculated from the inverted conductivity tensor, equation (2.45). The insets in Fig. 5.8(a) and Fig. 5.8(b) show ρ_{xx} and ρ_{xy} without the EEI correction, respectively. In both cases all curves collapse into one, which proves that the EEI correction is determined correctly.

5.3 A comparison of L_s determined from MC and $\sigma(T)$

In Chapter 2 we discussed that the two relevant mechanisms of spin dephasing in graphene depend differently on the mean free path. Therefore, we plot L_s, determined from from the MC and $\sigma(T)$, as a function of l_p for the studied samples (Fig. 5.10). In samples SS1 and SS2 we covered a range of mean free paths from 60 to 180 nm. In order to extend this range to lower l_p, we irradiate (see Chapter 6 for details)

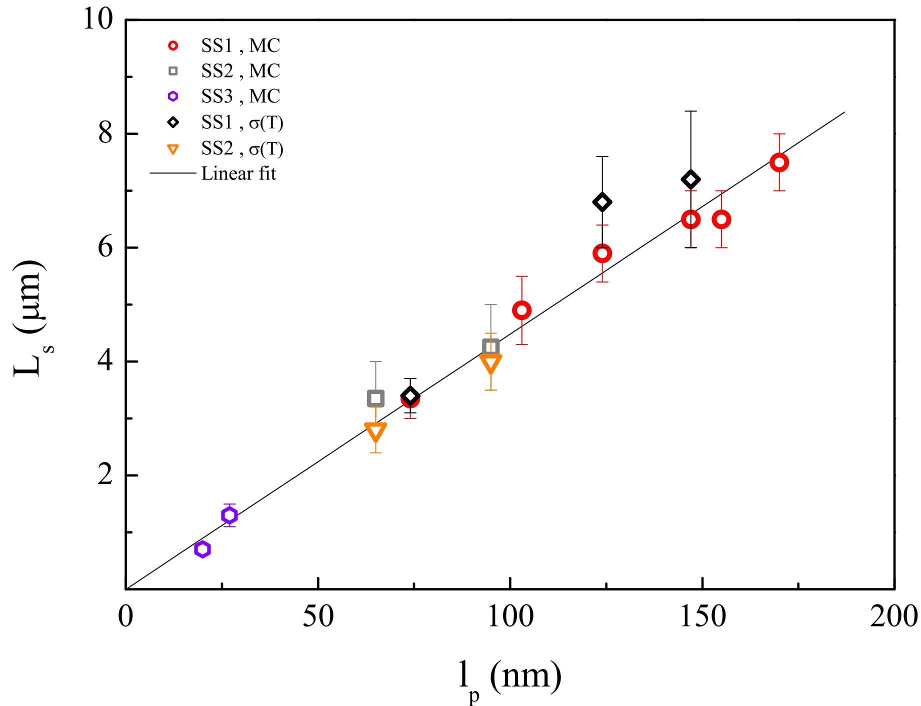

Figure 5.10: The spin coherence length as a function of the mean free path determined from the MC analysis (circles, squares and hexagons) and the temperature dependence of the conductivity, equation (5.3) (diamonds and triangles). Circles and diamonds correspond to sample SS1, squares and triangles - to sample SS2, hexagons - to sample SS3. The solid line is a linear fit to experimental data shown by red circles. Error bars show possible values of L_s that can be used to fit the experimental dependences.

sample SS3 with gallium ions. This increases disorder in graphene and reduces the mean free path to 20 nm. The spin coherence length determined from the MC in sample SS3 is also shown in Fig. 5.10. The spin coherence length increases linearly as the mean free path increases suggesting the Elliot-Yafet type of spin decoherence. The values of L_s determined from the MC and $\sigma(T)$ studies and in different samples are consistent and all lie on the same line. The significance of the Elliot-Yafet type of spin decoherence could be inferred from Fig. 5.3, where only WL is observed at all studied temperatures and carrier densities. For the Dyakonov-Perel mechanism one would observe weak antilocalisation of electrons.

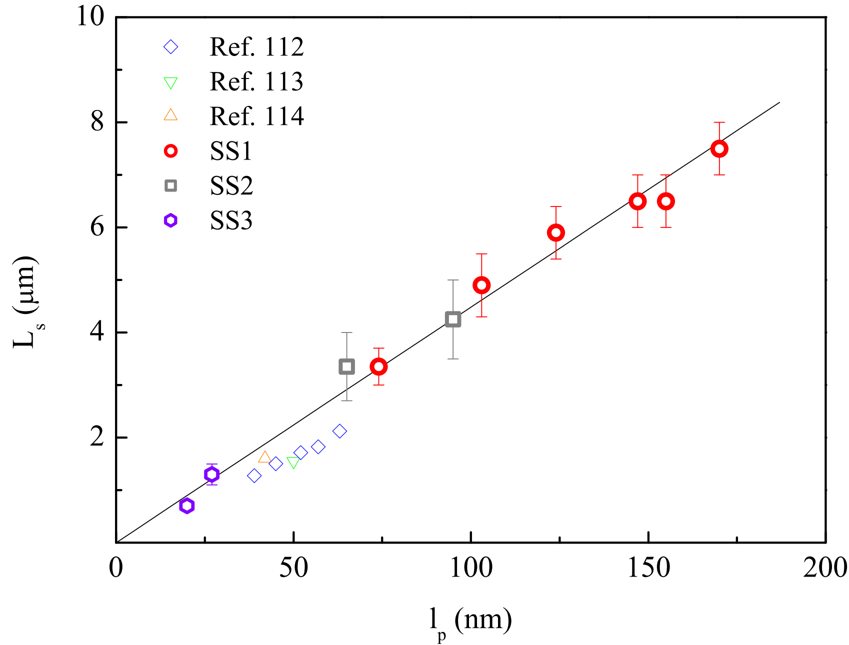

Figure 5.11: The dependence of the spin coherence length on the mean free path determined by different experimental groups [112–114].

5.3.1 Spin-related phenomena in previous papers on weak localisation

In the previous papers [34, 97, 101] where WL in graphene was studied SOI or spin-flip scattering were not taken into account. This is justified for the reason that at temperatures above 1 K the dephasing length is much smaller than the spin coherence length. Therefore the effect of the spin-related phenomena on WL is negligible. In the first paper to study WL in detail [34], the saturation of $L_{\varphi s}$ at temperatures below 1 K was shown to be due to the length of the sample, i.e. the condition $L_{\varphi} = L$ was met.

5.3.2 Comparison of L_s determined by different experimental groups

Figure 5.11 compares the values of the spin coherence length found in the three studied samples (circles, squares and hexagons) with those found by other experimental groups [112–114]. These groups studied spin transport using non-local spin valve measurements, so the methods to determine L_s are completely different to ours. As can be seen from the figure, however, all methods lead to a more or less consistent

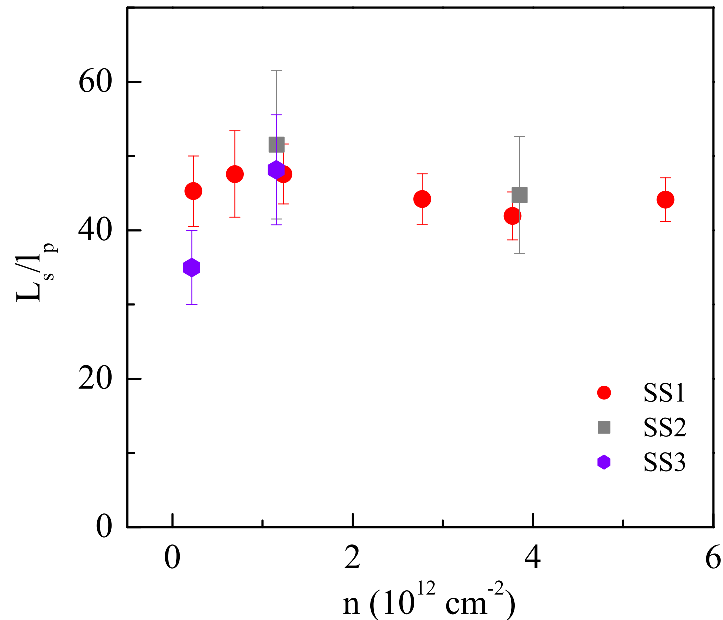

Figure 5.12: The dependence of the ratio L_s/l_p on the carrier density for the three studied samples.

picture. (The slightly smaller spin coherence lengths determined from the spin-valve experiments possibly result from the presence of the layer of Al_2O_3, which acts as a source of additional spin dephasing.) Interestingly, the found spin coherence lengths are very small compared to theoretically predicted values [115–119].

5.3.3 Speculations about the short spin coherence length

The momentum relaxation time in graphene is mainly controlled by remote Coulomb scatterers, which can be deduced from the almost linear dependence of the conductivity on carrier density (see the inset in Fig. 5.2(a)). Nevertheless, the correlation between L_s and l_p does not inherently imply that spin decoherence is caused by the same scatterers. We compare [125], in Table 5.2, the density dependence of

Table 5.2: Approximate dependence on electronic density n of the ratio of the spin coherence length to the mean free path L_s/l_p using estimates from recent literature [120–124].

	weak short-range	strong short-range	long-range Coulomb
intrinsic SOI	$\sqrt{n}$	$\sqrt{n}$	$\sqrt{n}$
short-range SOI	1	$1/\sqrt{n}$	$1/\sqrt{n}$

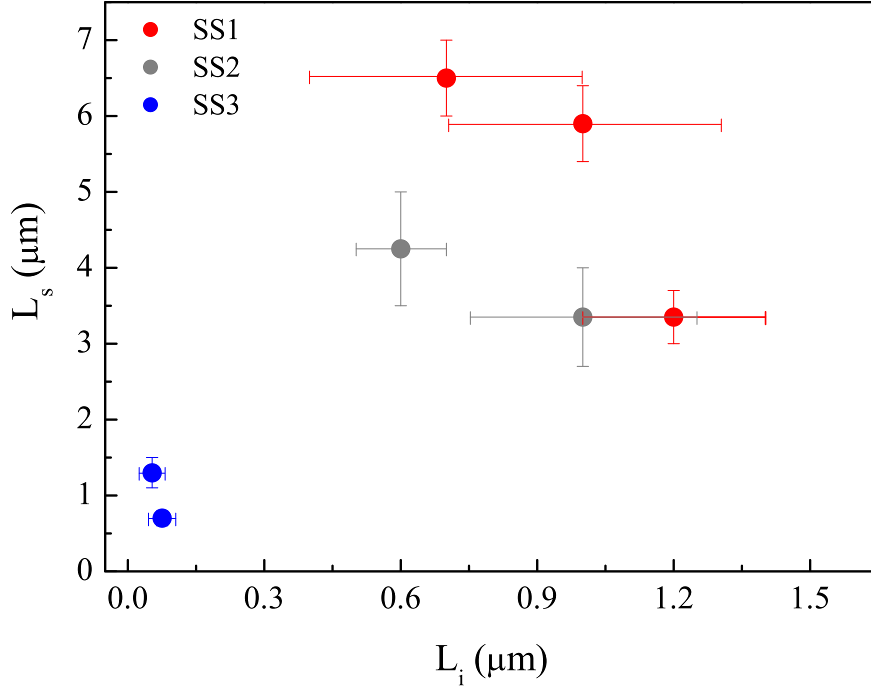

Figure 5.13: The dependence of the ratio L_{s}/l_p on the inter-valley scattering length for the three studied samples.

the mean free path $l_p = \nu_F \tau_p$ with that of the spin coherence length L_{s} for various assumptions about the nature of disorder and type of SOI, taking into account that $L_{\mathrm{s}}/l_p \propto \sqrt{\tau_{\mathrm{s}}/\tau_p}$. The data shown in Fig. 5.10 are taken at different carrier densities ranging from 0.2 to $5.5{\times}10^{12}$ cm^{-2} and, therefore, it is clear from the proportionality seen in the figure that there is no dependence of L_{s}/l_p on the carrier density. (One can also plot the dependence of L_{s}/l_p on n, see Fig. 5.12) This indicates that both SOI and momentum relaxation are controlled by a weak, short-range correlated disorder (see Table 5.2), which contradicts the observed dependence of the conductivity on carrier density. Therefore, we attribute [125] the observed saturation of $L_{\varphi\mathrm{s}}$ to spin-flip scattering from resonant localised states in the vicinity of the Dirac point, which can be produced by e.g. vacancies, boundaries or hydrocarbons [120]. Such states would lead to the spin coherence time $\tau_s \propto \varepsilon_F$, which would result in $L_s/l \propto \sqrt{\tau_s/\tau}$ independent of carrier density in the sample.

We can go further by looking at the correlation of L_{s} with the inter-valley scattering length L_i. Inter-valley scattering occurs on atomically sharp defects but is not affected by long-range impurities. Figure 5.13 shows that in each sample with increasing carrier density L_i decreases due to an increase in the density of states.

At the same time L_s also increases (in agreement with the fact that $\tau_s \propto \varepsilon_F$). This result confirms that it is strong short-range disorder arising from resonant scatterers that leads to the short spin coherence length such that L_s/l_p is independent of n. The same correlation between L_s and L_i is observed also in sample S2 and ion-irradiated sample SS3.

Chapter 6

Electron transport in ion irradiated graphene

In the previous chapter we studied the quantum corrections to the conductivity at temperatures down to 20 mK. We determined the spin coherence length and plotted it as a function of the mean free path l_p. To extend the range of l_p, we irradiated sample SS3 with ions. Irradiation introduced more disorder in the sample and significantly decreased the mean free path.

In this chapter we study electron transport through sample SS3. We compare the results of measurements before and after irradiation and find a number of interesting features. We also show experimental results of measurements of the temperature dependence of the resistivity performed in other ion bombarded samples, each having different dosages of irradiation.

6.1 Light irradiation. Weak localisation regime

Quantum transport through non-irradiated graphene samples was discussed in detail in Chapters 4 and 5. Sample SS3 (see Table 5.1) was studied at temperatures 0.25 - 40 K in the same way as in these two chapters starting from the fabrication and finishing with the investigation of the two quantum corrections.

Before bombarding a sample with ions, all contacts to it are grounded to prevent charge accumulation in graphene during irradiation. The sample is then placed in a vacuum chamber at 10^{-5} mbar and exposed to a 5 keV focused gallium ion beam at room temperature for a given time. The ion current is 15 pA. Depending on the

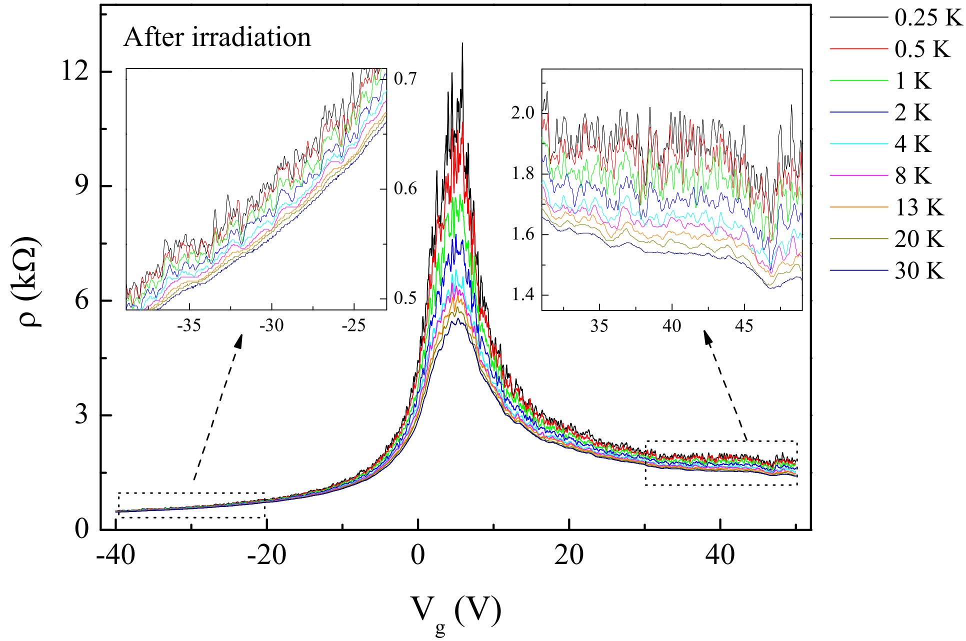

Figure 6.1: The gate voltage dependence of the resistivity measured at different temperatures in sample SS3 after irradiation. The two insets are zoomed-in regions shown in the main graph by rectangles.

time of exposure τ_{exp} we can tune the level of disorder. After irradiation the sample is annealed at 140°C for a few hours in a helium atmosphere before being transferred to a cryostat for measurements.

For 'light' irradiation, $\tau_{\text{exp}} < 4\,\text{s}$, a slight increase of the resistivity (compared to non-irradiated samples) at the Dirac point is observed, Fig. 6.1. The figure also shows that ρ decreases as T increases at any carrier density in the entire range of studied temperatures. Transport at low temperatures is found to still be governed by the quantum corrections to the conductivity that logarithmically depend on temperature, Fig. 6.2.

6.1.1 Weak localisation and electron-electron interaction corrections

We combine measurements of the magnetoconductivity (MC) and the temperature dependence of the conductivity at zero magnetic field in order to study the weak localisation (WL) and electron-electron interaction corrections (EEI) to the conductivity. The MC is measured in regions I and II (Fig. 6.3(a, b)) and analysed using equation (2.27). The three characteristic lengths, L_φ, L_i, L_*, extracted from

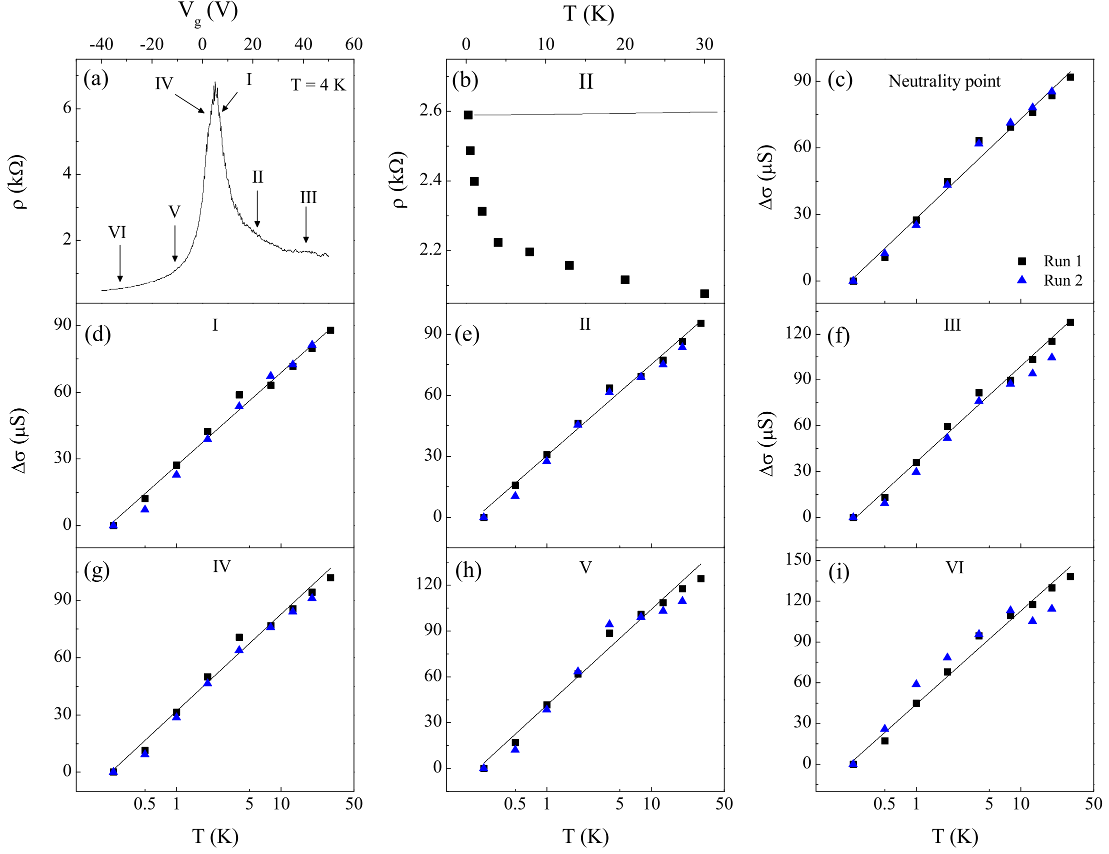

Figure 6.2: (a) The $R(V_g)$ curve at 4 K. Arrows indicate the studied regions of the gate voltage (carrier density). (b) The temperature dependence of the resistivity shown for region II. The solid line is the electron–acoustic phonon contribution to ρ with the deformation potential of 30 eV. (c - i) The temperature dependence of the conductivity in seven regions of the gate voltage plotted in the semilogarithmic scale. Regions I, II and III correspond to 3, 16 and 36 V with respect to the neutrality point, respectively, and regions IV, V and VI to -3, -16 and -36 V with respect to the NP. The measurements are shown for two experimental runs. Solid lines in the $\Delta\sigma(T)$ dependences are linear fits.

the analysis are used to determine the WL correction to the conductivity at zero magnetic field, equation (2.41) (most of the experimental points were obtained at high temperatures where $L_\varphi < L_{SO}$; therefore, the effect of spin can be neglected). The temperature dependence of the conductivity in regions II and III is then fitted with equation (5.3), in which A is the only fitting parameter. The EEI correction (Fig. 6.3(c, d)) is found to be the same as in non-irradiated samples (see [101] and Chapters 4 and 5): the coefficient A from equation (2.31) is 0.6 ± 0.1. (The electron–acoustic phonon contribution [52, 53] is negligibly small compared to the experimental temperature dependence of the resistivity, Fig. 6.2(b). To compare the two we used the largest value of the deformation potential $D_a = 30\,\text{eV}$ reported

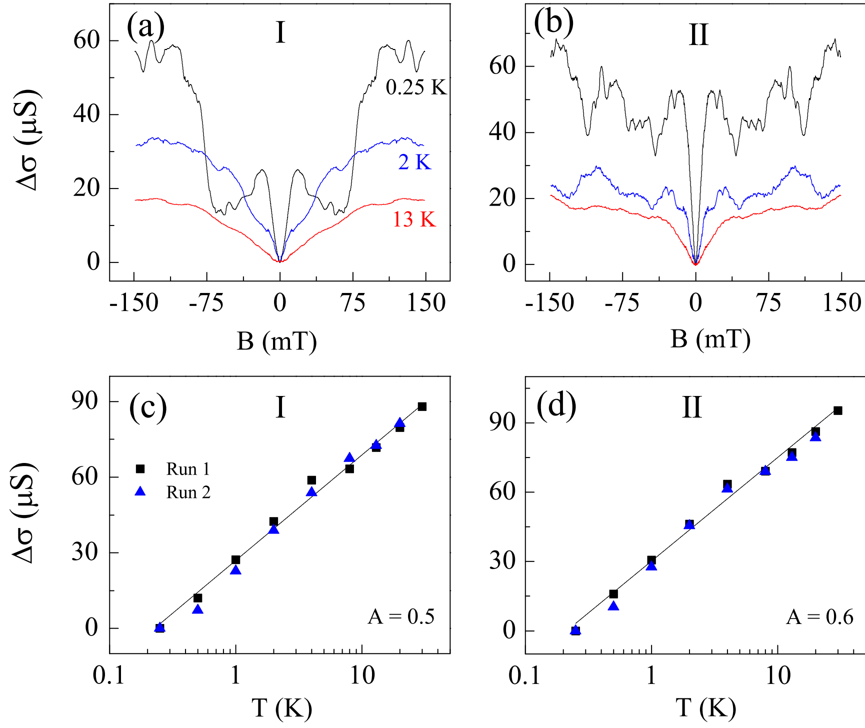

Figure 6.3: (a, b) Magnetoconductivity measured in regions I and II at different temperatures. (c, d) The temperature dependence of the conductivity in the same regions. The coefficient A from equation (2.31) is shown. Different symbols correspond to different experimental runs.

so far [59]. Therefore, the phonon contribution was not taken into account.)

6.1.2 Inter-valley scattering length

From the analysis of MC we found that the inter-valley scattering length was significantly reduced after irradiation and became comparable to the mean free path, which varied between 20 and 80 nm depending on the region. In non-irradiated samples $L_i \sim 1\mu$m. Small values of L_i show that atomic scale defects were being introduced into the graphene by the ion bombardment. Additional remote impurities were also introduced in the irradiation procedure as gallium became embedded in the silicon dioxide substrate.

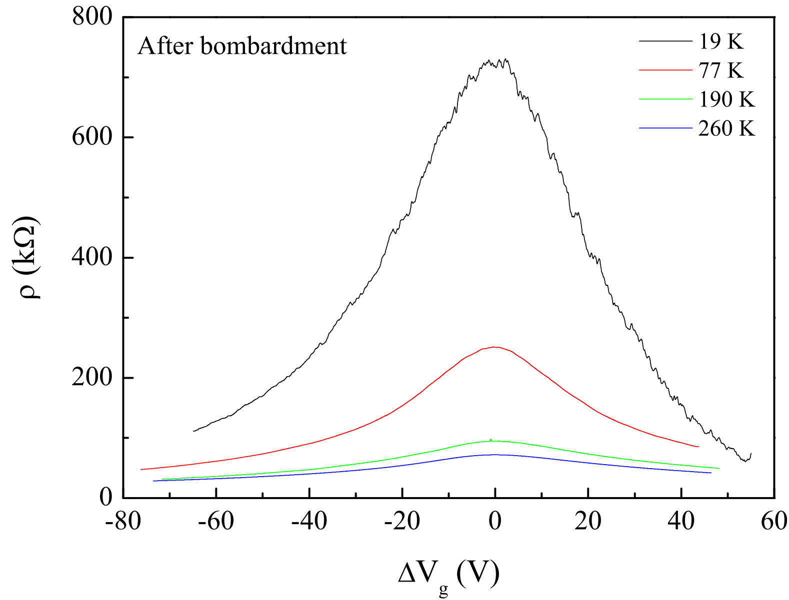

Figure 6.4: The resistivity as a function of the gate voltage measured after ion bombardment at different temperatures. The curves are shifted to zero gate voltage.

6.2 Heavy irradiation. Strong localisation regime. Variable-range hopping

Investigation of electron transport through graphene samples irradiated with larger dosages of ions is presented for another sample. For 'heavy' irradiation, $\tau_{\rm exp} \geq 4\,{\rm s}$, the resistivity at the Dirac point becomes of the order of $10^6\,\Omega$ at low temperatures, Fig. 6.4. A comparison between $\rho(T)$ before and after bombardment is given in Fig. 6.5. One can see that before irradiation at low temperatures ρ decreases due to the quantum corrections. The following increase of the resistivity up to 100 K at the NP and in region I is due to weak antilocalisation of charge carriers (as we discussed in Chapter 4 the electron–acoustic phonon contribution is negligibly small at low carrier densities). In regions II and III the increase of $\rho(T)$ is due to electron-acoustic phonon scattering. Above 100 K the contribution from optical phonons in SiO_2 becomes significant. A decrease of $\rho(T)$ above 200 K at the NP is due to thermal activation of charge carriers.

After irradiation the resistivity decreases as a function of temperature at all carrier densities in the entire range of studied temperatures. In this case $\rho(T)$ is best described by the variable-range hopping mechanism of the resistivity (Fig. 6.6). Similar effects at large dosages of irradiation were observed by other experimental

groups [57, 126].

We varied the time of exposure, τ_{exp}, between 2 and 4 s, and compared the results of measurements before and after irradiation (Table 6.1).

The energy of the ion beam and the current are minimal for our focused ion beam system. Smaller values of these parameters would lead to a more precise control of the irradiation dosage (the time τ_{exp} would be larger). Therefore, it would be possible to decrease the mean free path below 20 nm and, at the same time, stay in the weak localisation regime. Such control would make it possible to achieve values of L_{s} smaller than $0.8\,\mu$m (Chapter 4).

In summary, we show that irradiation of graphene by ions changes the behavior of electrons. At low dosages we found a significant decrease of the inter-valley scattering length. The low temperature transport is still governed by the quantum corrections to the conductivity. At high dosages electrons become strongly localised leading to the variable-range hopping mechanism of the conductivity.

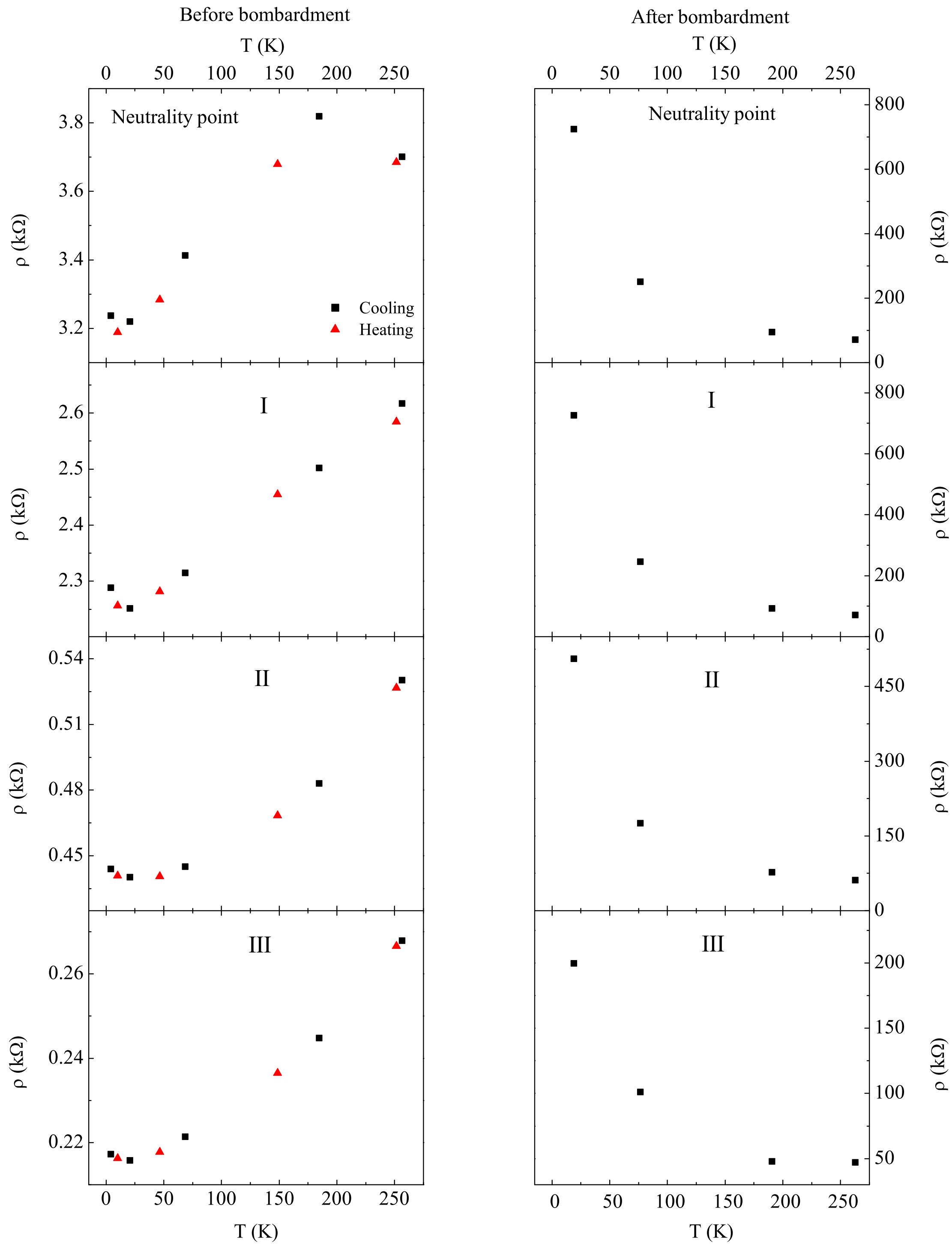

Figure 6.5: The temperature dependence of the resistivity before (left column) and after (right column) ion irradiation measured at the neutrality point (NP) and in regions I, II and III. These regions are the same as in all previous experiments. Before ion bombardment the resistivity was measured first at increasing temperatures (triangles), then at decreasing temperatures (squares), and after bombardment only at decreasing T.

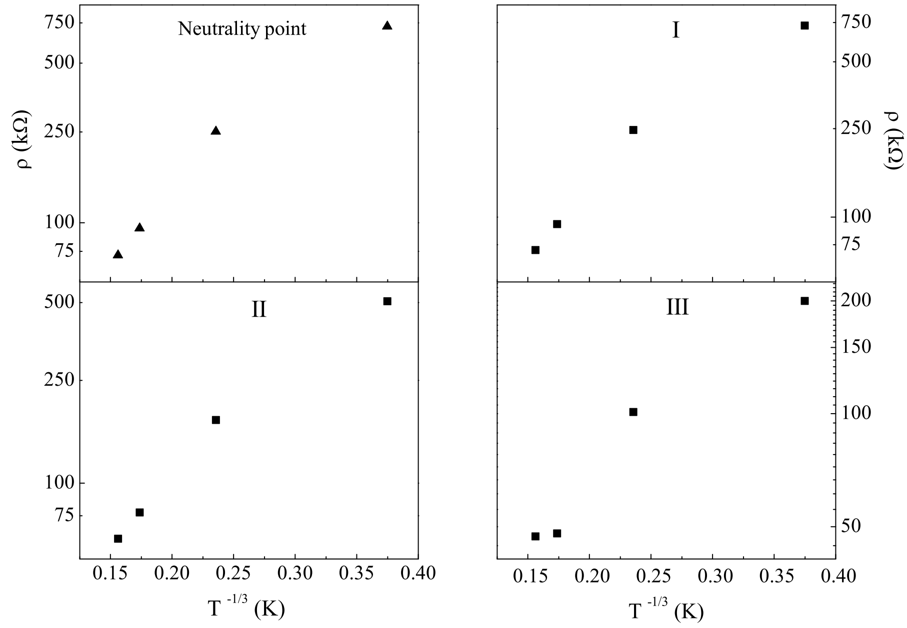

Figure 6.6: The resistivity as a function of temperature for a heavily irradiated sample. Experimental points follow the $\exp(T^{-1/3})$ dependence, which indicates that electron transport occurs via variable-range hopping.

Table 6.1: Sample parameters before and after ion bombardment. The resistivity is given at the neutrality point at different temperatures and the mobility (in $cm^2V^{-1}s^{-1}$) at 20 V with respect to the NP. The exposure time for irradiation is also shown.

Sample No	Before bombardment	After bombardment
1	$\rho(295\,K) = 2.35$ kΩ $\rho(4.2\,K) = 3.2$ kΩ $\mu(295\,K) = 20000$	Exposure time: 16 s Sample does not conduct
2	$\rho(260\,K) = 3.7$ kΩ $\rho(4.2\,K) = 3.2$ kΩ $\mu(260\,K) = 10000$	Exposure time: 4 s $\rho(260\,K) = 72$ kΩ $\rho(20\,K) = 720$ kΩ $\mu(260\,K) = 70$
3	$\rho(260\,K) = 1.7$ kΩ $\rho(4.2\,K) = 1.9$ kΩ $\mu(260\,K) = 7900$	Exposure time: 2 s $\rho(260\,K) = 1.9$ kΩ $\rho(4.2\,K) = 2.8$ kΩ $\mu(260\,K) = 6400$
4	$\rho(260\,K) = 4.8$ kΩ $\rho(4.2\,K) = 5.4$ kΩ $\mu(260\,K) = 2600$	Exposure time: 3 s $\rho(260\,K) = 16.9$ kΩ $\rho(4.2\,K) = 127.4$ kΩ $\mu(260\,K) = 490$

Chapter 7

Conclusions

In this thesis we investigate the conductivity of graphene at different temperatures, carrier densities and magnetic fields. There are different contributions to the conductivity at different temperatures: the weak localisation and electron-electron interaction corrections, electron-phonon interaction and temperature-independent (Drude) conductivity caused by electron scattering off impurities. In this thesis we measure and analyse each of them separately.

Our main focus is the quantum corrections to the Drude conductivity. We report the first experimental observation of these corrections in graphene in a wide range of temperatures (20 mK - 200 K). Due to the presence of the two valleys and the Berry phase of π, weak localisation in graphene is sensitive to both inelastic and elastic scattering mechanisms leading to a theoretically predicted transition from WL to WAL. In experiments we find that with increasing temperature from 5 to 200 K or decreasing carrier density from $2.6 \cdot 10^{12}$ to $0.2 \cdot 10^{12}$ cm^{-2} this transition indeed takes place. Moreover, surprisingly, quantum interference can survive at unusually high temperatures, up to 200 K, due to weak electron-phonon scattering.

The transition can be observed not only in the magnetoconductivity studies, but also in the temperature dependence, $\sigma(T)$, of the conductivity. In both cases the transition temperatures for different carrier densities are in good agreement with each other. In the $\sigma(T)$ dependence there is the electron-electron interaction correction, which depends on T similarly to the WL correction. Therefore, investigation of the quantum corrections requires their separation, which we perform using several methods. All of them yield the same magnitude of the EEI correction.

The analysis of the interaction correction can give information about the Fermi-liquid constant, F_0^σ. In two-valley systems with parabolic dispersion relation the dependence of the EEI correction on F_0^σ is sensitive to the strength of inter-valley scattering. Interestingly, in graphene the strength of intra-valley scattering is also important leading to a new expression for the EEI correction. We use this expression to determine the value of the Fermi-liquid constant, which turns out to be smaller than in other two-dimensional systems due to the chirality of charge carriers.

The magnitude of the WL correction goes up as the temperature is decreased due to increasing the dephasing length. At $T < 100$ mK the dephasing length, $L_{\varphi \mathrm{s}}$, saturates. We study several mechanisms that could be responsible for such saturation and focus on the effect of the spin-orbit interaction and spin-flip by resonant scatterers, attributing the saturated value of $L_{\varphi \mathrm{s}}$ to the spin coherence length, L_s. We demonstrate that the strength of this effect can be tuned experimentally by showing a direct proportionality between the spin coherence length and the mean free path. We further show that spin decoherence is dominated by resonant scatterers in a graphene sheet and that they are responsible for the short values of the coherence length compared to those expected theoretically.

Bibliography

[1] K. S. Novoselov, *et al.*, *Science* **306**, 666 (2004).

[2] P. R. Wallace, *Phys. Rev.* **71**, 622 (1947).

[3] R. Saito, G. Dresselhaus, M. S. Dresselhaus, *Physical Properties of Carbon Nanotubes* (Imperial College Press, 1998).

[4] N. M. R. Peres, F. Guinea, A. H. Castro Neto, *Phys. Rev. B* **73**, 125411 (2006).

[5] V. P. Gusynin, S. G. Sharapov, J. P. Carbotte, *Int. J. Mod. Phys. B* **21**, 4611 (2007).

[6] A. H. Castro Neto, F. Guinea, N. M. R. Peres, K. S. Novoselov, A. K. Geim, *Rev. Mod. Phys.* **81**, 109 (2009).

[7] A. K. Geim, K. S. Novoselov, *Nature Materials* **6**, 183 (2007).

[8] K. V. Klitzing, G. Dorda, M. Pepper, *Phys. Rev. Lett.* **45**, 494 (1980).

[9] K. S. Novoselov, *et al.*, *Nature* **438**, 197 (2005).

[10] Y. Zhang, Y.-W. Tan, H. L. Stormer, P. Kim, *Nature* **438**, 201 (2005).

[11] G. Begrman, *Phys. Rep.* **107**, 1 (1984).

[12] C. W. J. Beenakker, H. van Houten, *Solid State Physics* (Academic Press Inc., San Diego, 1991).

[13] E. McCann, *et al.*, *Phys. Rev. Lett.* **97**, 146805 (2006).

[14] S. Hikami, A. I. Larkin, Y. Nagaoka, *Prog. Theor. Phys.* **63**, 707 (1980).

[15] A. K. Savchenko, A. S. Rylik, V. N. Lutskii, *JETP* **58**, 1279 (1983).

[16] C. Schierholz, R. Kursten, G. Meier, T. Matsuyama, U. Merkt, *phys. stat. sol. (b)* **233**, 436 (2002).

[17] C. Schierholz, T. Matsuyama, U. Merkt, G. Meier, *Phys. Rev. B* **70**, 233311 (2004).

[18] H. Suzuura, T. Ando, *Phys. Rev. Lett* **89**, 266603 (2002).

[19] A. F. Morpurgo, F. Guinea, *Phys. Rev. Lett* **97**, 196804 (2006).

[20] S. V. Morozov, *et al.*, *Phys. Rev. Lett* **97**, 016801 (2006).

[21] B. L. Altshuler, A. G. Aronov, D. E. Khmelnitsky, *J. Phys. C: Solid State Phys.* **15**, 7367 (1982).

[22] B. N. Narozhny, G. Zala, I. L. Aleiner, *Phys. Rev. B* **65**, 180202 (2002).

[23] T. A. Polyanskaya, I. I. Saidashev, *JETP Lett* **34**, 361 (1981).

[24] L. V. den dries, C. V. Haesendonck, Y. Bruynseraede, G. Deutscher, *Phys. Rev. Lett.* **46**, 565 (1981).

[25] M. E. Gershenson, V. N. Gubankov, Y. E. Zhuravlev, *JETP Lett.* **35**, 467 (1982).

[26] P. H. Woerlee, G. C. Verkade, A. G. M. Jansen, *J. Phys. C: Solid State Phys.* **16**, 3011 (1983).

[27] R. Taboryski, P. E. Lindelof, *Semicond. Sci. Technol* **5**, 933 (1990).

[28] Y. F. Komnik, V. Y. Kashirin, B. I. Belevtsev, E. Y. Beliaev, *Phys. Rev. B* **50**, 15298 (1994).

[29] S. Pedersen, *et al.*, *Phys. Rev. B* **60**, 4880 (1999).

[30] P. T. Coleridge, A. S. Sachrajda, P. Zawadzki, *Phys. Rev. B* **65**, 125328 (2002).

[31] G. M. Minkov, A. V. Germanenko, I. V. Gornyi, *Phys. Rev. B* **70**, 245423 (2004).

[32] A. Y. Kuntsevich, *et al.*, *Phys. Rev. B* **75**, 195330 (2007).

[33] K. Y. Chen, C.-T. Liang, N. C. Chen, P. H. Chang, C.-A. Chang, *Chinese Journal of Physics* **45**, 616 (2007).

[34] F. V. Tikhonenko, D. W. Horsell, R. V. Gorbachev, A. K. Savchenko, *Phys. Rev. Lett.* **100**, 056802 (2008).

[35] D. W. Horsell, F. V. Tikhonenko, R. V. Gorbachev, A. K. Savchenko, *Phil. Trans. R. Soc. A* **366**, 245 (2008).

[36] B. L. Altshuler, V. E. Kravtsov, I. V. Lerner, *JETP Lett.* **43**, 441 (1986).

[37] B. L. Altshuler, V. E. Kravtsov, I. V. Lerner, *Sov. Phys. JETP* **64**, 1352 (1986).

[38] B. L. Altshuler, D. E. Khmelnitski, *JETP Lett.* **42**, 360 (1985).

[39] P. A. Lee, A. D. Stone, H. Fukuyama, *Phys. Rev. B* **35**, 1039 (1987).

[40] B. L. Altshuler, A. G. Aronov, *Electron-Electron Interactions in Disordered Systems* (North-Holland, Amsterdam, 1985).

[41] J. Friedel, *Philos. Mag.* **43**, 153 (1952).

[42] C. Kittel, *Quantum Theory of Solids* (Wiley, New York, 1963).

[43] G. Zala, B. N. Narozhny, I. L. Aleiner, *Phys. Rev. B* **64**, 214204 (2001).

[44] V. V. Cheianov, V. I. Falko, *Phys. Rev. Lett.* **97**, 226801 (2006).

[45] A. V. Shytov, *Private communication* .

[46] M. Polini, R. Asgari, Y. Barlas, T. Pereg-Barnea, A. H. MacDonald, *Solid State Commun.* **143**, 58 (2007).

[47] N. N. Klimov, *et al.*, *Phys. Rev. B* **78**, 195308 (2008).

[48] H. P. Wittmann, A. Schmid, *J. Low Temp. Phys* **69**, 131 (1987).

[49] Y. Y. Proskuryakov, *et al.*, *Phys. Rev. Lett.* **86**, 4895 (2001).

[50] K. E. J. Goh, M. Y. Simmons, A. R. Hamilton, *Phys. Rev. B* **77**, 235410 (2008).

[51] Y. Zhang, *et al.*, *Phys. Rev. Lett.* **96**, 136806 (2006).

[52] T. Stauber, N. M. R. Peres, F. Guinea, *Phys. Rev. B* **76**, 205423 (2007).

[53] E. H. Hwang, S. D. Sarma, *Phys. Rev. B* **77**, 115449 (2008).

[54] S. Fratini, F. Guinea, *Phys. Rev. B* **77**, 195415 (2008).

[55] E. Mariani, F. von Oppen, *Phys. Rev. Lett.* **100**, 076801 (2008).

[56] E. Mariani, F. von Oppen, *Phys. Rev. B* **82**, 195403 (2010).

[57] J.-H. Chen, C. Jang, S. Xiao, M. Ishigami, M. S. Fuhrer, *Nature Nanotechnology* **3**, 206 (2008).

[58] C. Dean, *et al.*, *Nature Nanotechnology* **5**, 722 (2010).

[59] D. K. Efetov, P. Kim, *Phys. Rev. Lett.* **105**, 256805 (2010).

[60] J. J. Lin, J. P. Bird, *Phys.: Condens. Matter* **14** (2002).

[61] P. G. Elliot, *Phys. Rev.* **96**, 266 (1954).

[62] Y. Yafet, *Solid State Physics* (Academic, New York, 1963).

[63] M. I. Dyakonov, V. I. Perel, *Sov. Phys. Solid State* **13**, 3023 (1972).

[64] M. I. Dyakonov, V. Y. Kachorovskii, *Sov. Phys. Semicond.* **20**, 110 (1986).

[65] N. F. Mott, *Phil. Mag.* **19**, 835 (1969).

[66] M. Pollak, B. Shklovskii, *Hopping transport in solids* (North-Holland, 1991).

[67] B. I. Shklovskii, A. L. Efros, *Electronic Properties of Doped Semiconductors* (Springer, Berlin, 1984).

[68] V. L. Mironov, *Fundamentals of the scanning probe microscopy* (The Russian Academy of Sciences Institute of Physics of Microstructures, 2004).

[69] G. Binnig, H. Rohrer, *IBM Journal of Research and Development* **30**, 4 (1986).

[70] G. Binnig, C. F. Quate, C. Gerber, *Phys. Rev. Lett.* **56**, 930 (1986).

[71] K. S. Novoselov, *et al.*, *Proc. Natl Acad. Sci.* **102**, 10451 (2005).

[72] R. Singh, *Physics in Perspective* **4**, 399 (2002).

[73] S. Picozzi, *et al.*, *J. Vac. Sci. Technol. A* **22**, 1466 (2004).

[74] D. M. Basko, *Phys. Rev. B* **78**, 125418 (2008).

[75] Z. H. Ni, *et al.*, *Phys. Rev. B* **77**, 115416 (2008).

[76] T. M. G. Mohiuddin, *et al.*, *Phys. Rev. B* **79**, 205433 (2009).

[77] C. Casiraghi, *et al.*, *Nano Lett.* **9**, 1433 (2009).

[78] Z. H. Ni, *et al.*, *ACS Nano* **3**, 569 (2009).

[79] R. Ma, D. Yoon, K.-Y. Chun, S. Baik, *Chem. Phys. Lett* **474**, 158 (2009).

[80] F. Alzina, *et al.*, *Phys. Rev. B* **82**, 075422 (2010).

[81] A. C. Ferrari, *et al.*, *Phys. Rev. Lett.* **97**, 187401 (2006).

[82] A. Gupta, G. Chen, P. Joshi, S. Tadigadapa, P. C. Eklund, *Nano Lett.* **6**, 2667 (2007).

[83] D. M. Basko, S. Piscanec, A. C. Ferrari, *Phys. Rev. B* **80**, 165413 (2009).

[84] I. Calizo, *et al.*, *Nano Lett.* **7**, 2645 (2007).

[85] I. Calizo, F. Miao, W. Bao, C. N. Lau, A. A. Balandin, *Appl. Phys. Lett.* **91**, 071913 (2007).

[86] E. A. Obraztsova, A. V. Osadchy, E. D. Obraztsova, S. Lefrant, I. V. Yaminsky, *phys. stat. sol. (b)* **245**, 2055 (2008).

[87] I. Calizo, I. Bejenari, M. Rahman, G. Liu, A. A. Balandin, *106* .

[88] P. Delhaes, *Graphite and Precursors* (Gordon and Breach Science Publishers, 2001).

[89] R. E. Peierls, *Helv. Phys. Acta* **7**, 81 (1934).

[90] R. E. Peierls, *Ann. Inst. H. Poincare* **5**, 177 (1935).

[91] L. D. Landau, *Phys. Z. Sowjet Union* .

[92] L. D. Landau, E. M. Lifshitz, *Statistical Physics, Part I* (Pergamon, Oxford, UK, 1980).

[93] McCord, M. A. M. J. Rooks, *Handbook of Microlithography, Micromachining and Microfabrication. Volume 1.* (SPIE Optical Engineering Press, 1997).

[94] P. Blake, *et al.*, *Appl. Phys. Lett.* **91**, 2007 (063124).

[95] O. V. Lounasmaa, *Experimental Principles and Methods Below 1 K.* (Academic Press London and New York, 1974).

[96] L. J. van der Pauw, *Philips Research Reports* **13**, 1 (1958).

[97] F. V. Tikhonenko, A. A. Kozikov, A. K. Savchenko, R. V. Gorbachev, *Phys. Rev. Lett.* **103**, 226801 (2009).

[98] K. Nomura, A. H. MacDonald, *Phys. Rev. Lett.* **98**, 076602 (2007).

[99] K. Kechedzhi, *et al.*, *Phys. Rev. Lett.* **102**, 066801 (2009).

[100] S. Morozov, *et al.*, *Phys. Rev. Lett.* **100**, 016602 (2008).

[101] A. A. Kozikov, A. K. Savchenko, B. N. Narozhny, A. V. Shytov, *Phys. Rev. B* **82**, 075424 (2010).

[102] S. Datta, *Electronic Transport in Mesoscopic Systems* (Cambridge University Press, 1995).

[103] J. B. Miller, *et al.*, *Phys. Rev. Lett.* **90**, 076807 (2003).

[104] T. Nihei, Y. Suzuki, M. Kohda, J. Nitta, *phys. stat. sol. (c)* **3**, 4239 (2006).

[105] B. L. Altshuler, A. G. Aronov, A. I. Larkin, D. E. Khmelnitski, *Zh. Eksp. Teor. Fiz.* **81**, 411 (1981).

[106] S. A. Vitkalov, K. James, B. N. Narozhny, M. P. Sarachik, T. M. Klapwijk, *Phys. Rev. B* **67**, 113310 (2003).

[107] N. N. Klimov, *et al.*, *Phys. Rev. B* **78**, 195308 (2008).

[108] M. Y. Kharitonov, K. B. Efetov, *Phys. Rev. B* **78**, 033404 (2008).

[109] K. Kechedzhi, O. Kashuba, V. I. Falko, *Phys. Rev. B* **77**, 193403 (2008).

[110] P. Esquinazi, *et al.*, *Phys. Rev. B* **66**, 024429 (2002).

[111] F. Schedin, *et al.*, *Nature Materials* **6**, 652 (2007).

[112] C. Jozsa, *et al.*, *Phys. Rev. B* **80**, 241403(R) (2009).

[113] W. Han, *et al.*, *Appl. Phys. Lett.* **94**, 222109(R) (2009).

[114] M. Shiraishi, *et al.*, *Adv. Funct. Mater.* **19**, 3711 (2009).

[115] C. Kane, E. Mele, *Phys. Rev. Lett.* **95**, 226801 (2005).

[116] D. Huertas-Hernando, F. Guinea, A. Brataas, *Phys. Rev. B* **74**, 155426 (2006).

[117] H. Min, *et al.*, *Phys. Rev. B* **74**, 165310 (2006).

[118] Y. Yao, F. Ye, X.-L. Qi, S.-C. Zhang, Z. Fang, *Phys. Rev. B* **75**, 041401 (2007).

[119] J. C. Boettger, S. B. Trickey, *Phys. Rev. B* **75**, 121402 (2007).

[120] N. M. R. Peres, F. Guinea, A. H. Castro Neto, *Phys. Rev. B* **73**, 125411 (2006).

[121] T. Ando, *J. Phys. Soc. Jpn.* **75**, 074716 (2006).

[122] K. Nomura, A. H. MacDonald, *Phys. Rev. Lett.* **98**, 076602 (2007).

[123] M. I. Dyakonov, V. Y. Kachorovskii, *Phys. Rev. Lett.* **98**, 186806 (2007).

[124] A. Ferreira, *et al.*, *Phys. Rev. B* **83**, 165402 (2011).

[125] E. McCann, V. Fal'ko, *Private communication* .

[126] J. Moser, *et al.*, *Phys. Rev. B* **81**, 205445 (2010).